THE UNIVERSITY OF CHICAGO

STUDIES OF THE RELATIONSHIP BETWEEN GALAXIES AND THE INTER/CIRCUM-GALACTIC MEDIUM

A DISSERTATION SUBMITTED TO
THE FACULTY OF THE DIVISION OF THE PHYSICAL SCIENCES
IN CANDIDACY FOR THE DEGREE OF
DOCTOR OF PHILOSOPHY

DEPARTMENT OF ASTRONOMY AND ASTROPHYSICS

BY
SEAN D. JOHNSON

CHICAGO, ILLINOIS
AUGUST 2016

TABLE OF CONTENTS

LIST OF FIGURES

LIST OF TABLES

ACKNOWLEDGMENTS

First, I would like to thank my thesis advisor, Hsiao-Wen Chen for her tireless commitment to daring and excellent observational astrophysics as well as graduate education. The knowledge, experience, and wisdom that she shared with me throughout the scientific process – from proposal preparation to observing, analysis, interpretation, and publication – has been and will continue to be invaluable. Plus, it has been a lot of fun!

Next, I would like to thank my undergraduate and M.A. advisor, Don York for fostering my interest in observational astronomy and guiding me to graduate school. Through many nights on the Apache Point 3.5-m, Don taught me not only the technical ropes of observing, but also the value and pleasure of humbly observing the Universe.

I am deeply indebted to John Mulchaey for his enthusiastic support and undying optimism during my time at the Carnegie Observatories and throughout graduate school. I would like to thank the staff at Carnegie, and Gwen Rudie and Drew Newman in particular for their advice and guidance, both scientific and otherwise.

In addition, I want to thank Randy Landsberg and the Space Explorers. My experiences as the Space Explorers Instructor and at Yerkes have been among the most rewarding times of my graduate career.

Thank you to my family for their support over the years and for their tolerance of long hours and regular observing runs that kept me away from home. Jessie, Mom, Dad, Kelli – I could not have done it without you!

Finally, thank you to my office mates for the enlightening conversations, support, and for putting up with my loud typing: Louis Abramson, Eric Baxter, Hsin-Yu Chen, Roozbeh Davari, Ke Fang, Cameron Liang, Dan Masters, Vinicius Miranda, Monica Mocanu, Rebecca Pierce, Fakhri Zahedy. And thank you Vin for all the breaks from research!

My thesis involved extensive observing at the Magellan and DuPont telescopes at the Las Campanas Observatory in Chile, and the ARC 3.5-m telescope at the Apache Point

Observatory in New Mexico as well as data from the Hubble Space Telescope. The staff at Las Campanas, Apache Point, and the Space Telescope Science Institute make these world class facilities possible and a pleasure to use – thank you. Myself and the rest of the astronomical community are indebted to the astronauts who have made Hubble possible and extended its lifetime through daring space walks.

My research has been supported by funding from the National Science Foundation, the National Aeronautics and Space Administration, the Brinson Foundation, The University of Chicago, the Kavli Institute for Cosmological Physics, and the Carnegie Institution for Science.

ABSTRACT

Galaxies are thought to grow through star formation that is fueled by the accretion of gas in dark matter halos and from intergalactic space. In turn, star formation and active galactic nuclei drive outflows that regulate gas cooling and accretion while enriching the surrounding gas with heavy elements. The resulting enriched gaseous halos that surround galaxies are thought to dominate the baryon reservoirs capable of fueling future growth. Developing an empirical understanding of the relationship between galaxies and this surrounding gas consequently represents a key step toward a more complete understanding of galaxy evolution. The diffuse nature of galaxy halo gas renders direct emission too faint to be detected with current facilities except in extreme cases, but the gas can be readily observed as absorption features in the spectra of UV-bright background sources such as quasars. This thesis presents a series of observational studies that provide new insights into the relationship between galaxies and surrounding diffuse baryon reservoirs through combined galaxy redshift and quasar absorption line surveys. The majority of the thesis focuses on results from deep and highly complete galaxy redshift surveys with the Magellan Telescopes in fields with high quality quasar absorption spectra from the *Hubble Space Telescope* that probe highly ionized diffuse gas through absorption from the H I Lyman series and metal ion transitions such as the O VI doublet. The thesis begins in Chapter 1 with historical background and motivation. Chapter 2 then presents a detailed analysis of the absorbing gas and corresponding galactic environments in the field of PKS 0405−123 which has the highest signal-to-noise ratio absorption spectrum available among intermediate redshift quasars. Though based on a single sightline, these survey data provide evidence that highly ionized gas observed as O VI absorption systems primarily trace the extended gaseous halos of gas-rich galaxies and low-mass galaxy "groups" signified by the presence of nearby star-forming galaxies. Chapter 3 presents the discovery of an unusually transparent sightline at small projected distance from a pair of interacting galaxies. The H I absorption associated with this galaxy pair falls

more than two orders-of-magnitude below expected levels suggesting that interactions can significantly deplete cool halo gas reservoirs through stripping or heating. Chapter 4 presents a study of the spatial extent of H I and O VI absorbing gas as a function of both star-formation activity and galaxy environment out to 10× the galaxy host halo virial radius. Galaxies with nearby neighbors exhibit more extended O VI absorbing gas than isolated galaxies while no excess H I is observed suggesting that environment plays a role in distributing heavy element enriched gas beyond the gaseous halos of individual galaxies. In addition, Chapter 5 presents a survey of cool Mg II absorbing gas around quasar host galaxies to shed light on the relationship between cool halo gas and quasar activity while drawing insights into the environments of quasar hosts from the Magellan galaxy survey data. Together, these survey results highlight the role of environment in galaxy evolution and its possible relation with extended halo gas reservoirs. Finally, Chapter 6 summarizes the galaxy redshift and quasar absorption survey status, overviews data analysis techniques, highlights recent work confirming the results from Chapter 2 with a larger sample, and motivates future studies.

CHAPTER 1

INTRODUCTION

1.1 Early studies of galaxy halo gas

The notion that galaxies reside in extended and tenuous gaseous halos has its roots in the hot ($\approx 10^6$ K) interstellar galactic corona proposed by Spitzer (1956) to provide pressure confinement for observed cool interstellar clouds. Due to its low inferred density Spitzer (1956) noted, however, that the proposed hot "corona is apparently not observable optically except by absorption measures shortward of 2000 Å" through the C IV ($\lambda\lambda 1548, 1550$ Å), N V ($\lambda\lambda 1238, 1242$ Å), O VI ($\lambda\lambda 1031, 1036$ Å), or Mg X ($\lambda\lambda 609, 624$ Å) doublets which enable detection of gas at densities more than one million times lower than can be observed in emission. However, observations at such short wavelengths can only be carried out with a space-based ultraviolet telescope due to attenuation by the Earth's atmosphere. Nevertheless, even before direct evidence for the hot corona was available, the discovery of high velocity clouds (HVCs) in the Milky Way halo observed in 21-cm emission by Muller et al. (1963) led to speculation that the Galaxy may host a multiphase gaseous halo with both a hot corona and denser cool gas. Seventeen years after Spitzer's prediction, observations with the *Copernicus* satellite confirmed the existence of a hot corona through O VI doublet absorption in spectra of background Milky Way stars (Rogerson et al., 1973; Jenkins & Meloy, 1974; York, 1974). Constraints on the multi-phase halo gas of galaxies beyond the Milky Way, however, would require bright background objects with UV luminosities far in excess of that of bright, normal stars in typical distant galaxies.

Soon after Schmidt (1963) published the spectrum of 3C 273 demonstrating that quasars are likely extragalactic and at substantial cosmological distances, it was realized that absorption spectroscopy of these UV-bright point sources could serve as an ideal probe of galaxy halo gas outside of the local Universe. Bahcall & Salpeter (1966) suggested that discrete gas

clouds along the quasar sightline could be detected through individual absorption features in quasar spectra. Such intervening absorption systems were observed within a year (Burbidge et al., 1966; Greenstein & Schmidt, 1967), and as observations accumulated, Bahcall & Spitzer (1969) proposed that "most of the absorption lines are caused by tenuous gas in extended halos of normal galaxies". This hypothesis was confirmed, at least for metal-line absorbers, through the detection of galaxies at low projected distances from quasar sightlines and coincident in redshift with metal absorption systems such as Ca II H & K and Mg II (e.g. Boksenberg et al., 1980; Bergeron & Stasińska, 1986). Though debate continued on the origin of quasar redshifts for some time, the detection of galaxies with redshifts coincident with metal absorption systems left little doubt that quasar redshifts are cosmological in origin, and ever since quasar absorption spectroscopy has been and remains by far the most sensitive available tool for observing the diffuse gas around and between galaxies.

1.2 Galaxy formation in dark matter halos: the over-cooling and missing baryon problems

Observations of flat rotation curves (Rubin & Ford, 1970; Rubin et al., 1978) in nearby spiral galaxies and the discovery of the Cosmic Microwave Background (CMB; Dicke et al., 1965; Penzias & Wilson, 1965) led to a picture in which galaxies form as the result of baryon gas cooling (Rees & Ostriker, 1977) in self-gravitating dark matter halos (Ostriker et al., 1974; White & Rees, 1978) that grew from primordial overdensities (Silk, 1968) in the early Universe. The connection between the the statistical properties of the large-scale distribution of galaxies in the local Universe (e.g. Geller & Huchra, 1989) with that of primordial overdensities inferred from the CMB anisotropy power spectrum (Smoot et al., 1992) represents one of the greatest triumphs of modern physics. However, in simulations that include well-understood gravitational and gas physics, simulated galaxies exhibit efficient gas cooling and star formation leading to significant over-predictions of galaxy stellar masses

and an over-abundance of both low- and high-mass galaxies (e.g. Cole, 1991; Katz & Gunn, 1991; Navarro & White, 1994). This "over-cooling problem" demonstrates that radiative cooling limited models of galaxy growth are incomplete and that non-gravitational feedback mechanisms associated with galaxy and star formation are needed to provide the energy and momentum necessary to prevent efficient cooling. Developing an understanding of these feedback mechanisms is a driving goal in modern extragalactic astrophysics.

Possible feedback mechanisms that can solve the over-cooling problem include galactic-scale winds driven by supernovae and massive stars (e.g. Dekel & Silk, 1986), mass loss from evolved stars and Type 1a supernovae in dispersion supported galaxies (e.g. Mathews & Baker, 1971; Conroy et al., 2015), and energy released during accretion of material onto central supermassive black holes during a quasar phase (e.g. Silk & Rees, 1998). Outflows are routinely observed as blue-shifted absorption in "down-the-barrel" observations of starbursting local galaxies (e.g. Heckman et al., 2000) and star-forming galaxies at high redshift (e.g. Shapley et al., 2003). Though the down-the-barrel observations do not directly provide evidence that the outflows escape the ISM, this led to a framework in which galaxies form through gas accretion from the intergalactic medium (IGM) and cooling regulated by heating and outflows that, in turn, pollute the IGM and galaxy halos with heavy-element enriched gas. Consequently, observations of this diffuse gas can lead to significant insights into the baryon cycles thought to regulate galaxy evolution.

Given a cosmological model and set of feedback prescriptions, large hydrodynamic simulations can predict the expected distribution and physical state of baryons in simulated universes. Because the total cosmological baryon content in the Universe can be inferred from both Big Bang Nucleosynthesis (e.g. Burles et al., 2001) and precise measurements of the CMB (e.g. Spergel et al., 2003; Planck Collaboration et al., 2015) the disposition of baryons as a function of time relative to the expected total forms a sensitive possible test of our understanding of structure formation. A census of stars and emitting gas in the local Universe

accounts for only $\approx 12\%$ of the expected baryon budget (Fukugita et al., 1998; Fukugita, 2004; Fukugita & Peebles, 2004), confirming that gas cooling and star formation in galaxies are globally inefficient processes. The majority of the remaining "missing baryons" are predicted to reside in the IGM and in diffuse galaxy halo gas (also known as the circum-galactic medium or CGM) with cool ($T \lesssim 10^5$ K) IGM dominating the baryon budget at $z > 2$. As time goes on, however, gas near collapsing dark matter halos is predicted to undergo shock heating to $T = 10^5 - 10^7$ K resulting in a warm-hot phase of the IGM (WHIM) that dominates the baryon budget at $z < 1$ (e.g. Cen & Ostriker, 1999; Davé et al., 2001). Much like the hot galactic corona, however, the temperatures and densities of the WHIM mean that this predicted baryon phase can only be observed through UV or X-ray absorption studies.

1.3 The UV extragalactic renaissance

Motivated in no small part by the possibility of observing the IGM and galaxy halo gas in absorption, Spitzer (1968) proposed a 120-in diameter space telescope which eventually came to fruition in the form of the *Hubble Space Telescope* (HST). When launched in 1990, HST carried the Goddard High Resolution Spectrograph (GHRS; Soderblom et al., 1995) and Faint Object Spectrograph (FOS; Keyes et al., 1995) which enabled observations of the IGM and CGM at $z \lesssim 1$ though quasar absorption spectroscopy. The HST Quasar Absorption Line Key project in particular obtained UV spectra of 37 quasars enabling the first large, systematic studies of the IGM at $z < 1$ (Bahcall et al., 1993). At nearly the same time, the construction of new ground-based facilities such as the twin Keck 10-m telescopes on Mauna Kea in Hawaii combined with efficient, high resolution spectrographs such as HIRES (Vogt et al., 1994) enabled observations of the IGM through the forest of Lyα absorption lines at $z \gtrsim 2$. With these pioneering facilities, astronomers found that the cool IGM observed in the Lyα forest at $z = 2 - 3$ can account for $\gtrsim 95\%$ of the expected baryons (e.g. Rauch et al., 1997), but only $\approx 25\%$ of baryons at low-redshift (e.g. Penton et al., 2000, 2004). These

observations combined with the prediction that the WHIM should dominate the baryon budget at low redshift motivated searches for this highly ionized gas through UV and x-ray absorption.

The installation of the Space Telescope Imaging Spectrograph (STIS; Woodgate et al., 1998) on HST in 1997 during the second servicing mission enabled high resolution observations of the IGM at observed wavelengths of $\approx 1150-1650$ Å with an efficiency more than ten times that of the FOS and GHRS. Two years later, the launch of the Far Ultraviolet Spectroscopic Explorer (FUSE; Moos et al., 2000) extended the observable wavelength range to cover $900-1150$ Å, enabling observations of the highly ionized IGM/CGM through O VI and Ne VIII absorption at low redshift. Absorption surveys searching for highly ionized gas found that O VI absorbers can account for a significant fraction of the "missing" baryons (e.g. Tripp et al., 2000, 2008; Thom & Chen, 2008a,b) though the physical state and origins of the these highly ionized absorbers remained uncertain.

In the mean time, ground-based galaxy redshift surveys in the fields of quasars with absorption spectra at both low ($z \lesssim 1$: Lanzetta et al., 1995; Stocke et al., 1995; Chen et al., 1998, 2001) and high ($z = 2-3$: Adelberger et al., 2003; Steidel et al., 2010; Rudie et al., 2012) redshifts enabled statistical studies of galaxy halo gas and its relationship with galaxy properties. These observations directly confirm the near ubiquitous presence of multiphase, metal-enriched halo gas surrounding galaxies with high observed covering fractions of low and intermediate ionization state gas out to $d \lesssim 100$ kpc and more highly ionized O VI absorbing gas out to $d \lesssim 300$ kpc around star-forming galaxies (Chen & Mulchaey, 2009).

Despite the substantial gain in throughput achieved by STIS over the previous generation of UV spectrographs, the total HST+STIS system efficiency peaks at $\approx 1\%$ (see Woodgate et al., 1998, for details) limiting the IGM studies with STIS to the brightest ≈ 16 quasars on the sky (e.g. Tripp et al., 2008; Thom & Chen, 2008a). To enable UV spectroscopy of fainter UV sources, the Cosmic Origins Spectrograph (COS) was installed on HST in 2009

during the fourth and last servicing mission. Because the efficiency of optical elements in the UV is low, COS was designed to minimize the number of optical elements with gratings that diffract and focus the incident light onto the detector while simultaneously correcting for the spherical aberration of the HST primary mirror and astigmatism in the instrument (Green et al., 2012). This unique spectrograph design enabled an order-of-magnitude increase in efficiency and a corresponding increase in the survey path length of IGM observations at $z \lesssim 0.7$ (e.g. Danforth et al., 2016).

While COS was being designed, observational astronomy was revolutionized by the Sloan Digital Sky Survey (SDSS; York et al., 2000) which used the purpose-built Apache Point 2.5-m telescope to survey $15,000\,\mathrm{deg}^2$ of the sky with both imaging and spectroscopy resulting in over 200 million galaxies with five-band photometry as well as 2.4 million galaxies and 477,000 quasars with spectra (see the SDSS Data Release 12 summary in Alam et al., 2015). The combination of COS and SDSS imaging/spectroscopy led to an extragalactic UV renaissance through observations of the CGM of hundreds of galaxies probed at small projected distance by background quasars bright enough to be observed at moderate resolution with COS (e.g. Tumlinson et al., 2011; Stocke et al., 2013; Tumlinson et al., 2013; Werk et al., 2013; Borthakur et al., 2013; Bordoloi et al., 2014; Liang & Chen, 2014).

At the same time, computational advances have enabled high resolution cosmological and zoom-in hydrodynamic simulations incorporating sub-grid feedback recipes that can reproduce many of the bulk properties of galaxies observed in emission and as well as IGM absorption statistics in some cases (e.g. Davé et al., 2010, 2011; Agertz et al., 2011; Oppenheimer et al., 2012; Hopkins et al., 2014; Vogelsberger et al., 2014; Agertz & Kravtsov, 2015; Schaye et al., 2015; Rahmati et al., 2015, 2016). However, the simulations that best reproduce the emission properties of galaxies systematically under-predict the column densities of H I and heavy element ions observed in the CGM compared to observations indicating (1) that our understanding of galaxy evolution remains incomplete and (2) that observations of the

relationship between galaxies and the IGM/CGM can serve as a key test of sub-grid feedback prescriptions (Hummels et al., 2013; Liang et al., 2016; Ford et al., 2016; Oppenheimer et al., 2016).

1.4 Combined galaxy redshift and quasar absorption surveys

Despite the significant progress enabled by the combination of SDSS and COS, our understanding of the relationship between galaxies and the IGM/CGM remains incomplete. In particular, the majority of the observations carried out over the last decade have focused on characterizing galaxy halo gas at projected distances of less than a virial radius from targeted galaxies. Each foreground galaxy in the field of a UV bright quasars represents an opportunity to study surrounding gas at a given distance from the galaxy center by looking for absorbing gas in the quasar spectrum at the foreground galaxy redshift. Conversely, each galaxy in the field represents a potential host of absorbing gas. Higher S/N quasar spectra and higher completeness galaxy survey data can provide a more complete understanding of the relationship between galaxies and absorbing gas. In particular, the transition from halo gas to the IGM and the impact of short-lived but important stages of galaxy evolution such as galaxy interactions and AGN activity remain poorly constrained. Developing a more complete empirical understanding of the relationship between galaxies and the dominant, diffuse baryon reservoirs at $z \lesssim 1$ requires a combination of deep galaxy redshift surveys reaching faint galaxies over wide areas in fields with high quality quasar absorption spectra. Such wide-field, deep galaxy surveys are possible with the unique combination of wide-field multi-object spectroscopy and large telescope aperture offered by the Inamori-Magellan Areal Camera and Spectrograph (IMACS; Dressler et al., 2011) on the Magellan I 6.5-m telescope (Shectman & Johns, 2003). In this thesis, I present a series of observational studies of the relationship between galaxies and absorbing gas that focus primarily on a series of deep and highly complete galaxy redshift surveys carried out with the Magellan Telescopes in fields

with high S/N, moderate resolution COS quasar spectra. In particular, Chapter 2 presents a detailed comparative study of the galactic environments of quasar absorption systems in the field of PKS 0405−123 which has the highest available S/N absorption spectrum of all intermediate redshift quasars. Chapter 3 presents the discovery of an unusually transparent sightline at small projected distance from a pair of interacting galaxies. Chapter 4 presents a study of the spatial extent of H I and O VI absorbing gas as a function of both star-formation and galaxy environment out to 10× the galaxy host halo virial radius. In addition, Chapter 5 presents a large and statistical survey of the cool CGM of quasar host galaxies to shed light on the relationship between the CGM and quasar activity while drawing insights into quasar host environments from the Magellan galaxy surveys. Finally, Chapter 6 summarizes the current state of the survey and highlights ongoing as well as future work.

CHAPTER 2

NEW INSIGHTS INTO THE GALAXY ENVIRONMENTS OF O VI ABSORBERS IN PKS 0405−123

The contents of this chapter have been published in the Monthly Notices of the Royal Astronomical Society and are reproduced here in accordance with the copyright agreement and with permission from the Oxford University Press.

Johnson, S. D., Chen, H.-W., & Mulchaey, J. S. 2013, MNRAS, 434, 1765

2.1 Introduction

Ultraviolet absorption lines in the spectra of background sources represent the most sensitive available means of observing the diffuse gas that permeates the Universe. The O VI $\lambda\lambda$1031, 1037 doublet in particular has received attention as a tracer of: the warm-hot phase of the intergalactic medium (IGM; e.g. Cen & Ostriker, 1999), the galaxy outflows thought to be responsible for the chemical enrichment of the IGM (e.g. Oppenheimer & Davé, 2006), and the intra-group medium (Mulchaey et al., 1996). While independent surveys of O VI absorbers in the spectra of distant quasars have uncovered a large number of these systems supporting the notion of O VI doublets being a sensitive tracer of warm-hot gas, the reported number density of O VI absorbers from different surveys shows a scatter much beyond the individual measurement errors (e.g. Burles & Tytler, 1996; Tripp et al., 2000; Tripp & Savage, 2000; Prochaska et al., 2004; Richter et al., 2004; Tripp et al., 2008; Thom & Chen, 2008b; Danforth & Shull, 2008; Tilton et al., 2012). At the same time, cosmological simulations incorporating momentum-driven winds have been able to reproduce the observed O VI absorption column density distribution function, but ambiguity remains in attributing the majority of low-redshift O VI absorbers to either cool, photoionized gas (e.g. Kang et al., 2005; Oppenheimer & Davé, 2009; Oppenheimer et al., 2012) or the warm-hot phase of the

IGM (cf. Smith et al., 2011; Tepper-García et al., 2011; Cen, 2012; Stinson et al., 2012).

Key insights into the physical origin of O VI absorbers can be gained from a detailed examination of their galactic environments. Observations designed to constrain the properties of gaseous halos of known galaxies have shown that emission-line galaxies exhibit near unity O VI covering fractions ($\kappa_{\rm O\,VI}$) at projected distances $\rho \lesssim 150$ kpc and $\kappa_{\rm O\,VI} \approx 64\%$ at $\rho < 350$ kpc, while absorption-line galaxies exhibit $\kappa_{\rm O\,VI} \lesssim 30\%$ on similar scales (Chen & Mulchaey, 2009; Tumlinson et al., 2011). The large incidence of O VI absorbers around star-forming galaxies may be explained by a causal connection between star formation and the production of O VI absorbing gas, but the non-negligible covering fraction of such gas around an evolved galaxy population becomes difficult to explain under the same scenario.

While surveys of galaxies associated with known O VI absorbers have revealed a correlation between the presence of star-forming galaxies and O VI absorbers at modest projected separations of $\rho \lesssim 350$ kpc (Stocke et al., 2006; Prochaska et al., 2006; Chen & Mulchaey, 2009; Mulchaey & Chen, 2009; Wakker & Savage, 2009; Stocke et al., 2013), the galaxy survey data are not sufficiently deep and complete for a detailed examination of the galactic environment immediate to the absorbers. Dedicated surveys around UV bright quasar sightlines are typically limited to bright galaxies with R-band magnitudes brighter than $AB(R) \approx 19.5$ limiting sensitivity to $L \approx 0.1\,L_*$ galaxies at $z \lesssim 0.1$ (e.g. Prochaska et al., 2011a). Although the study of Wakker & Savage (2009) includes galaxies fainter than $L = 0.1\,L_*$ at $z < 0.02$, the incompleteness of their galaxy catalog is unknown. Survey incompleteness complicates the interpretation of the galaxy–absorber studies (Stocke et al., 2006, 2013). To date, a high completeness level ($> 95\%$) for galaxies of $R \lesssim 23$ and $\Delta\theta \lesssim 2'$ from the quasar sightline has been reached in only one quasar field (HE 0226−4110 in Chen & Mulchaey 2009). To improve the statistics, our group is continuing the effort to collect high-completeness galaxy survey data in multiple quasar fields.

In this chapter, we present new galaxy survey data obtained for the field around

PKS 0405−123 at $z_{\rm QSO} = 0.57$. Our galaxy survey in this field has reached 100% completeness within $\rho = 200$ kpc of the quasar sightline for galaxies as faint as $0.1\,L_*$ ($0.2\,L_*$) out to redshifts of $z \approx 0.35$ ($z \approx 0.5$). PKS 0405−123 is among the brightest quasars on the sky, for which high-quality UV echelle data have been obtained using STIS and extremely high-quality UV spectra have been obtained using COS. The intermediate redshift of the quasar provides a long redshift path length for probing intervening absorption systems. Previous systematic searches in the STIS and FUSE spectra of PKS 0405−123 have uncovered six O VI absorption systems at $z_{\rm O\,VI} = 0.09 - 0.5$ (Prochaska et al., 2004; Howk et al., 2009) and 11 additional strong Lyα absorbers of neutral hydrogen column density $\log N({\rm H\,I}) \geq 13.6$ at $z_{\rm H\,I} = 0.03 - 0.5$ (e.g. Williger et al., 2006; Lehner et al., 2007). Recent targeted searches in the new COS spectra have further uncovered a Ne VIII absorber associated with the strong O VI absorber at $z = 0.495$ (Narayanan et al., 2011) and a new component associated with the previously known O VI absorber at $z = 0.167$ (Savage et al., 2010).

To complement the available highly complete galaxy survey data, we have carried out a new systematic search of absorption features in the new COS spectra. Here we discuss new insights into the origin of O VI absorbing gas that we have learned from combining the improved absorption-line measurements and highly complete galaxy survey data. The chapter proceeds as follows: In Section 2.2 we present the full archival COS spectrum of PKS 0405−123 and new galaxy redshifts in our survey. In Section 2.3 we review measurements of the absorbers enabled by the COS spectrum including (1) a tentative detection of an O VI absorber at $z = 0.2977$, (2) a new O VI absorber at $z = 0.3615$, and (3) N V associated with a known O VI absorber at $z = 0.3633$. In Section 2.4 we discuss the galaxy environments of all seven O VI absorbers along this sightline and compare them to the galaxy environments of strong Lyα absorbers with no detected O VI. Finally, in Section 2.5, we briefly discuss the implications of our findings.

Throughout the chapter, we adopt a Λ cosmology with $\Omega_{\rm m} = 0.3$, $\Omega_\Lambda = 0.7$, and $H_0 = 70$

Table 2.1: Journal of spectroscopic observations

Telescope	Instrument/setup	FWHM (Å)	No. of targets	Exposure time (ks)	Date
Magellan Baade	IMACS/f2/200l, 1″ slitlets	9	17	3.6	Nov. 2012
			12	3.0	Feb. 2011
			150	5.4	Nov. 2012
			140	5.4	Feb. 2011
Magellan Clay	LDSS3/VPH-all 1″ slitlets	10	24	7.2	Feb. 2011
APO 3.5-m	DIS/B400 & R300, 1.5″ long slit	5	23	varies	Oct.−Dec. 2012

$\mathrm{km\,s^{-1}\,Mpc^{-1}}$. We also adopt a non-evolving, rest-frame absolute R-band magnitude (AB) of $M_{R*} = -21.17$ for L_* galaxies based on Blanton et al. (2003). Unless otherwise stated, we perform k-corrections using the Scd galaxy template from Coleman et al. (1980).

2.2 Data

PKS 0405−123 is a well-studied sightline with available imaging and UV spectroscopic data in the FUSE and HST archives (Chen & Prochaska, 2000; Prochaska et al., 2004; Williger et al., 2006; Lehner et al., 2007). Different galaxy surveys have been carried out in this field identifying galaxies associated with absorption-line systems uncovered in the UV spectra (Spinrad et al., 1993; Ellingson & Yee, 1994; Chen et al., 2005; Prochaska et al., 2006; Chen & Mulchaey, 2009). Recently, PKS 0405−123 was targeted for HST/COS UV spectroscopy at significantly higher S/N than the archival STIS spectra. This new data set led to the discovery of an interesting O VI absorber with no detectable H I at $\Delta v \approx -300$ $\mathrm{km\,s^{-1}}$ from a previously detected O VI absorber in a partial Lyman-limit system at $z = 0.1671$ (Savage et al., 2010). We have analyzed the full COS spectrum of PKS 0405−123 (Figure 2.1) together with new and existing galaxy survey data for a comprehensive study of the galactic environments of absorbing clouds uncovered along this quasar sightline.

Figure 2.1: COS spectrum of PKS 0405−123.

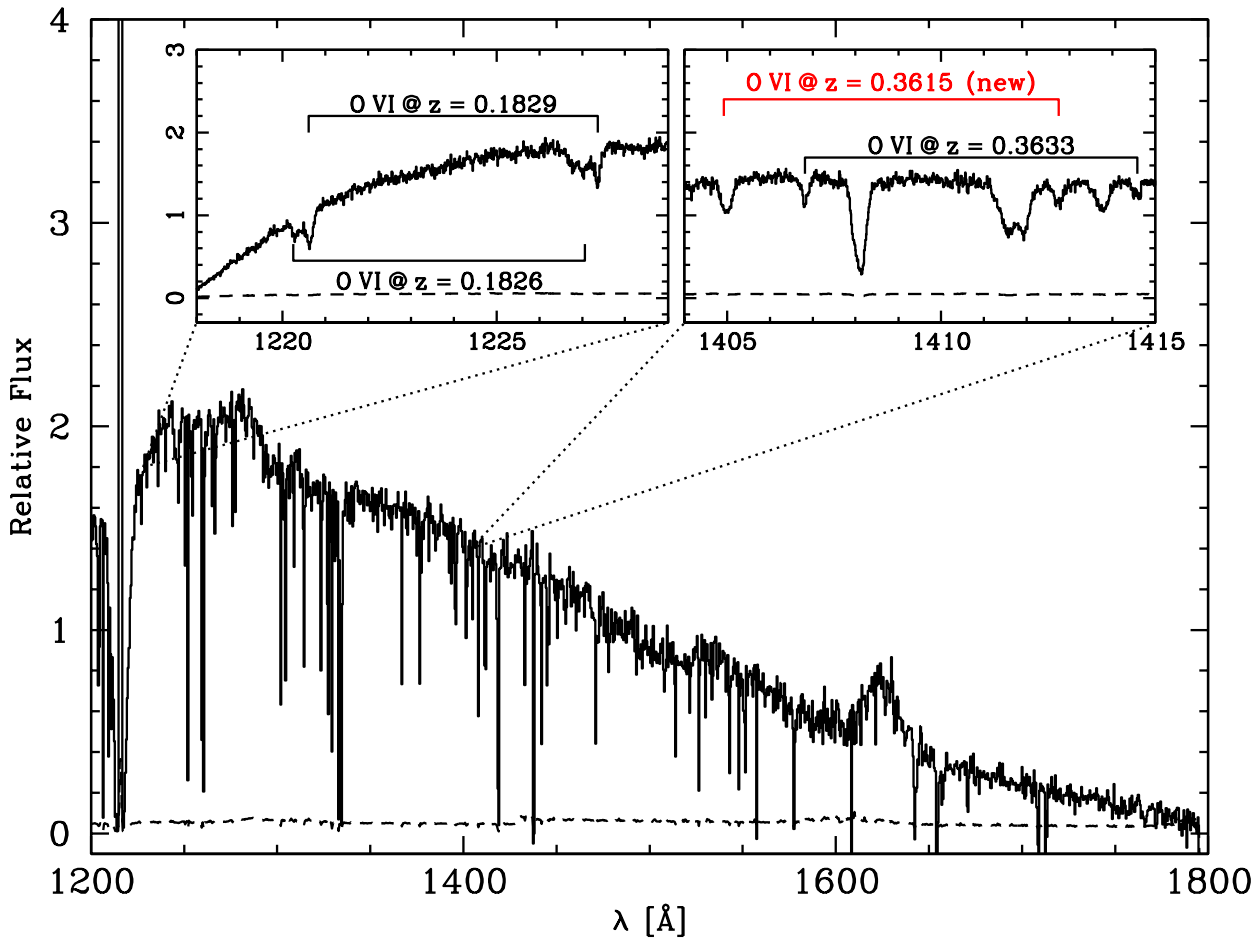

Reduced and combined COS spectrum (solid line) of PKS 0405−123 with corresponding 1-σ errors (dashed line). The inset plots highlight detections enabled by the improved S/N of the quasar spectrum. *Left*: O VI absorption at $z = 0.1829$ and 0.1826. *Right*: O VI absorption at $z = 0.3633$ and 0.3615 (new).

2.2.1 COS spectroscopy

PKS 0405−123 was targeted for COS observations by two separate *HST* programs (PI: Keith Noll, PID=11508 and PI: James Green, PID=11541). The two programs together acquired 17 exposures, totaling 22.2 ks with the G130M grating (covering the spectral range $1150 - 1450$ Å and with full width at half-maximum spectral resolution of FWHM = 16 $\mathrm{km\,s^{-1}}$), and 4 exposures, totaling 11.1 ks with the G160M grating ($1400 - 1800$ Å, FWHM = 16 $\mathrm{km\,s^{-1}}$). The exposures were acquired at different central wavelengths in order to provide contiguous wavelength coverage despite the gap between COS detectors. We retrieved the 1-D individual calibrated spectra from the Mikulski Archive for *HST* and combined them using a custom suite of software (see Yoon et al. 2012 for details). Specifically, individual spectra from the two detector segments were aligned and co-added using a common Milky Way absorption line as a reference (e.g., Si III 1206) and then combined into a single one-dimensional spectrum. These co-addition routines work with photon counts rather than flux calibrated data to allow for an accurate error estimate in the low-count regime (e.g. Gehrels, 1986). A well-known issue with far-ultraviolet (FUV) spectra obtained using COS is the presence of fixed-pattern noise due to the grid-wire in the COS FUV detectors. Such pattern noise can be reduced by the use of multiple FP-POS settings (see the COS Instrument Handbook). As described above, PKS 0405−123 was observed by two different programs and in many exposures of different FP-POS settings. The effect of such fixed-pattern noise is therefore minimal in the final stack. To ensure consistency with previous results, we set a common zero-point by aligning the co-added COS spectrum with the archival FUSE and STIS spectra prior to combination of the G130M and G160M data. This alignment led to minor ($\ll$FWHM) higher-order corrections to the COS wavelength calibration. By comparing the COS spectrum with the archival STIS spectrum, we estimate that errors in the wavelength calibration limit the accuracy of line-centroids to ≈ 4 $\mathrm{km\,s^{-1}}$.

The resulting high resolution spectrum (see Figure 2.1) enabled the new detections of

O VI systems in addition to a number of other lines and significantly stronger upper limits on key ions. The new detections are discussed in detail in Section 2.3.

2.2.2 Galaxy Survey

Previous spectroscopic surveys of galaxies in the PKS 0405−123 field reached ≈ 80% completeness within a 3′ radius of the quasar sightline for galaxies brighter than $R = 21$ and ≈ 50% for galaxies between $R = 21$ and 22 (e.g. Chen & Mulchaey 2009). These surveys identified galaxies associated with half of the known O VI absorbers along this quasar sightline; however, a detailed study of the galaxy environments that includes sub-L_* galaxies requires a higher survey completeness at fainter magnitudes. To improve the survey depth, we acquired new galaxy spectra with the Magellan telescopes using IMACS (Dressler et al., 2011) and the Low Dispersion Survey Spectrograph 3 (LDSS3) on the Magellan Telescopes. (see Table 2.1 for a summary of the observations). In addition, we confirmed a number of photometric stars using the Dual Imaging spectrograph (DIS) on the Apache Point 3.5-m. The IMACS and LDSS3 data were reduced using the Carnegie Observatories System for MultiObject Spectroscopy (COSMOS[1]) as described in Chen & Mulchaey (2009). The APO DIS spectra were reduced using a slightly modified version of the Low-REDUX pipeline written by J. Hennawi, S. Burles, and J. X. Prochaska[2]. Galaxy redshifts were determined both by cross-correlation with SDSS galaxy templates and by fitting of galaxy eigenspectra as in Chen & Mulchaey (2009). In nearly all cases, the two independently determined redshifts were in good agreement ($|\Delta z| \leq 0.0003$), but in the small number of cases for which they were not, we determined the best redshift by refitting and visual inspection. All assigned redshifts were visually inspected to determine their reliability and galaxy spectra were further classified as either absorption-line dominated or emission-line dominated. The final object

1. http://code.obs.carnegiescience.edu/cosmos

2. http://www.ucolick.org/∼xavier/LowRedux/

Table 2.2: The photometric and spectroscopic catalog of galaxies around PKS 0405−123[a]. The full table is available on the journal webpage.

ID	RA (J2000)	Dec (J2000)	$\triangle\theta$ ($''$)	ρ[b] (kpc)	R (mag)	$z_{\rm spec}$	Quality[c]	Object type[d]	Galaxy class[e]	L/L_*[b,f]
80001[n]	04:07:48.9	-12:11:33	7.8	51	21.65 ± 0.00	0.5715	A	G	E	0.95
90001	04:07:49.1	-12:11:38	9.9	64	22.10 ± 9.99	0.5697	A	G	E	0.62
80003[n]	04:07:49.1	-12:11:43	11.7	76	21.10 ± 0.00	0.5709	A	G	A	1.57
80004[n]	04:07:48.2	-12:11:49	12.8	83	19.97 ± 0.00	0.5678	A	G	A	4.36
80005[n]	04:07:48.6	-12:11:52	15.5	100	21.54 ± 0.00	0.5656	A	G	A	1.01
1883	04:07:48.3	-12:11:21	15.8	111	21.69 ± 0.12	0.6883	A	G	E	1.69
90002	04:07:49.5	-12:11:41	16.3	106	22.10 ± 9.99	0.5715	A	G	A	0.63
1920[n]	04:07:47.4	-12:11:26	18.5	137	22.77 ± 0.19	0.7797	A	G	A	0.97
1862	04:07:49.1	-12:11:21	18.5	112	22.63 ± 0.17	0.4942	A	G	E	0.25
1866	04:07:48.8	-12:11:58	22.0	142	21.40 ± 0.10	0.5713	A	G	E	1.19
80010[n]	04:07:49.8	-12:11:48	23.1	−1	21.70 ± 0.00	1.4657	B	G	E	−1.00
1820[n]	04:07:49.9	-12:11:49	24.8	161	21.75 ± 0.13	0.5686	A	G	A	0.85
1854	04:07:49.2	-12:12:04	29.6	194	21.23 ± 0.09	0.5779	A	G	E	1.44

Notes

[a] ID, coordinates, and R-band photometry from Prochaska et al. (2006) except for objects with IDs 800## or 900## which were added from Ellingson & Yee (1994) or based on visual inspection of the DuPont/WFCCD or *HST* images.

[b] Given a value of −1 when not available due to lack of a secure redshift or when not applicable.

[c] Redshift and classification quality: A→ secure (≥ 2 features), B→ 1 feature, C→ observed but no features, $N \rightarrow$ not observed.

[d] Object classification: Q→ quasar, G→ galaxy, S→ star, U→ unknown.

[e] Galaxy classification: E→ emission-line dominated, A→ absorption-line dominated, $N \rightarrow$ n/a.

[f] Measured from R-band photometry as discussed in text.

[n] Redshift and classification from new data presented in this chapter.

catalog is presented in Table 2.2.

The new IMACS/LDSS3 observations include 225 new galaxies without previously known redshifts, providing an unprecedented level of completeness in the field when combined with previous surveys. Specifically, the survey is 100% ($\approx 90\%$) complete for galaxies brighter than $R = 22$ ($R = 23$) within $1'$ of the quasar sightline. The relevant figure-of-merit, however, is the completeness as a function of galaxy luminosity, physical impact parameter, and redshift which is shown in Figure 2.2 along with a galaxy-redshift histogram[3]. The survey is 100% complete for $L > 0.1\,L_*$ galaxies at impact parameters less than $\rho = 100$ kpc and $> 90\%$ complete at $\rho < 200$ kpc at all redshifts $z < z_{\rm QSO}$. The completeness level decreases somewhat at larger impact parameters due to our targeting priority, but even at $\rho < 500$ kpc, the survey is $\gtrsim 75\%$ complete for $L > 0.1\,L_*$ galaxies at $z < z_{\rm QSO}$. The high level

3. We estimated the completeness function using the observed completeness as a function of magnitude and angular separation from the quasar sightline and smoothed with a $\Delta\, z = 0.1$ boxcar function to remove fluctuations due to small number statistics.

Figure 2.2: Summary of our galaxy survey results in the field of PKS 0405-123.

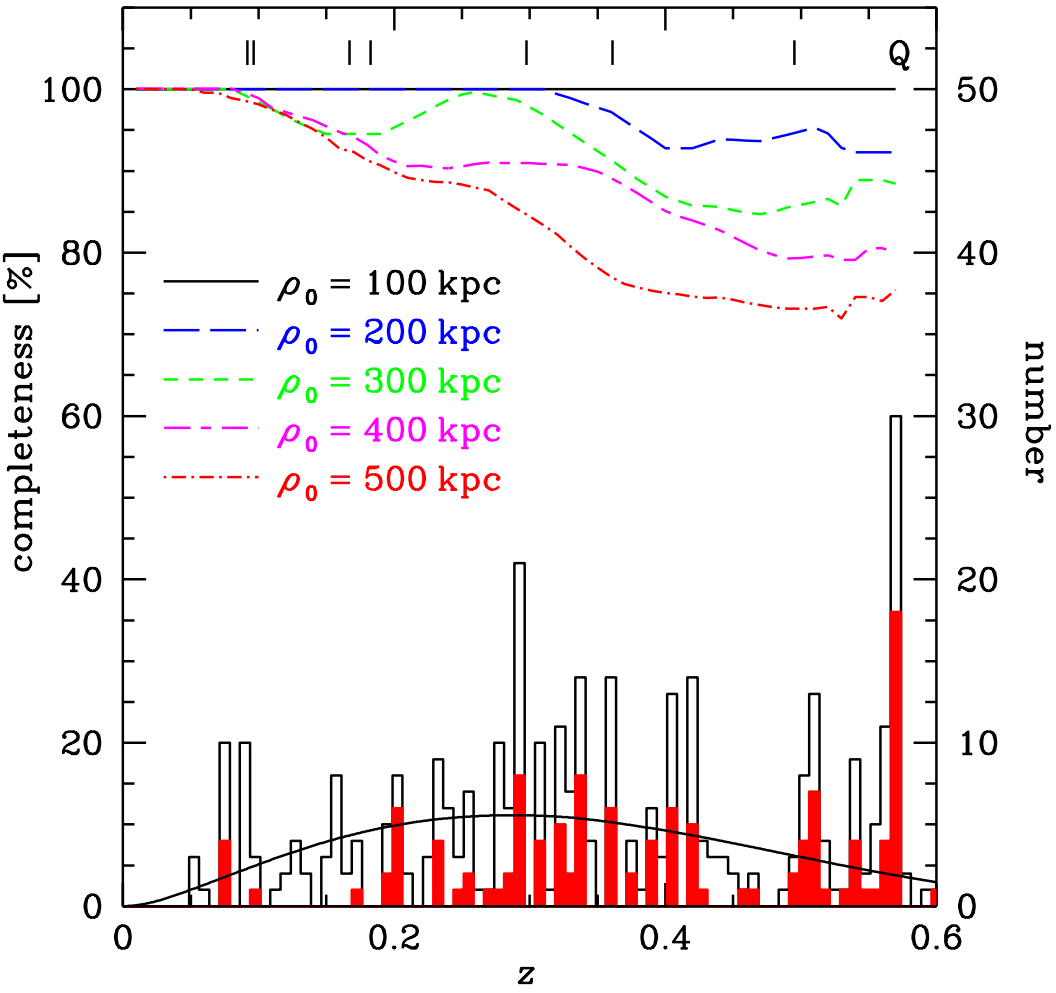

The curves at the top show the estimated survey completeness for $L > 0.1\,L_*$ galaxies as a function of redshift at projected distances of $\rho < 100$, 200, 300, 400, and 500 kpc of the quasar sightline. The bottom histograms show the redshift distributions of all galaxies (black) and absorption-line dominated galaxies (red, solid) in the final combined spectroscopic catalog. For comparison, we show the expected redshift distribution based on a non-evolving R-band luminosity function adapted from Blanton et al. (2003), taking into account our survey incompleteness as a function of galaxy luminosity and redshift (solid black line). Spikes in the histogram that deviate significantly from expectations are due to large-scale galaxy overdensities in the quasar field. The redshifts of O VI absorbers (vertical ticks) and the quasar (Q) are shown along the top of the figure.

of completeness is visually captured by the HST image of the field labelled with galaxy redshifts (Figure 2.3).

We note that in addition to the many foreground galaxies spectroscopically identified near the quasar line-of-sight, there exists a clear overdensity of galaxies at the redshift of the quasar. The galaxy catalog is therefore also valuable for studying AGN environments and fueling (e.g. Ellingson & Yee 1994) and discussed in Chapter 5.

2.3 New measurements of absorption-line systems

The higher S/N of the new COS data ensured both improved measurements of previously known transitions and new detections along the sightline. We conducted a systematic search of new absorption features in the COS spectra of PKS 0405−123 and identified three features that were previously unknown. These include: (1) a tentative detection of a new O VI absorber at $z = 0.2977$, (2) a new O VI component at $\Delta v = +170$ km s^{-1} from a previously known metal-line absorber at $z = 0.3608$, and (3) N V absorption associated with a known O VI system at $z = 0.3633$. Combining previous results with the new findings yielded a sample of seven O VI absorbers and 12 individual components found at $z = 0.0918 - 0.495$ along the sightline toward PKS 0405−123.

We measured the line profiles of both new and known O VI absorbers, as well as their associated H I and other metal transitions based on a Voigt profile analysis using the VPFIT package[4] (Carswell et al., 1987) and the empirical COS line spread function (LSF)[5]. The COS LSF exhibits broad wings which contain up to 40% of the flux (Ghavamian et al., 2009). The use of the empirical LSF in the Voigt profile fitting is therefore necessary in order to properly account for the absorption that falls in the wings of the LSF. In cases of line blending, we employed a simultaneous fit of a minimum number of separate components that

4. http://www.ast.cam.ac.uk/∼rfc/vpfit.html

5. http://www.stsci.edu/hst/cos/performance/spectral_resolution/

Figure 2.3: HST/Wide Field Planetary Camera 2 image of PKS 0405−123 at $z_{\rm em} = 0.573$.

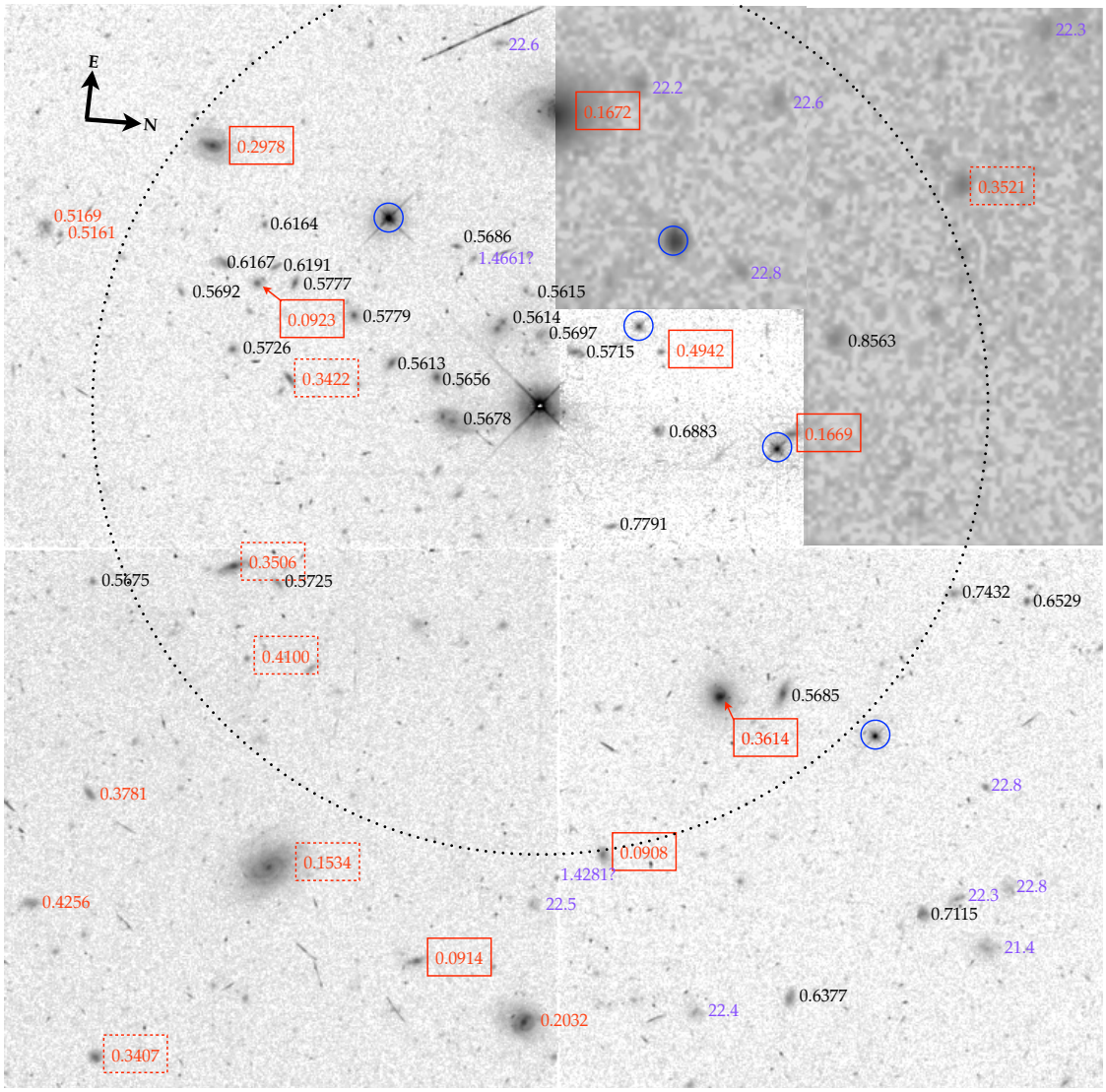

The HST image is augmented with an image from the DuPont telescope (Prochaska et al., 2006) where *HST* imagery is unavailable. The orientation of the field is indicated by the N–E arrows that appear in the upper-left corner. Redshifts are shown to the right of the corresponding galaxy except in crowded areas where an arrow is used to indicate association. Galaxies foreground to the quasar are shown in red, while background galaxies ($z \gtrsim z_{\rm QSO}$) are shown in black. Galaxies associated with O VI absorbers (with velocity offsets $|\Delta v| < 300$ km s^{-1}) are marked by solid red boxes, while galaxies associated with Lyα absorbers and no detectable O VI are marked by dotted red boxes. Stars are labelled with blue circles and galaxies without secure redshifts are marked in purple either by redshift (based on a single emission line) or R-band magnitude if no redshift is available. A dotted circle centered on the quasar with $1'$ radius is shown to provide scale. In addition to the many foreground galaxies spectroscopically identified near the quasar line-of-sight, there exists a clear overdensity of galaxies at the redshift of the quasar.

Table 2.3: Summary of line properties of known O VI absorbers in the sightline of PKS 0405−123

Element	Δv (km s^{-1})	b (km s^{-1})	$\log N$ / cm^{-2}	References[a]
		$z_{\rm sys} = 0.09180$		
H I	0	38 ± 2	14.52 ± 0.05	1
C IV	0		< 12.90	2
N V	0		< 12.67	2
O VI	+20		13.83 ± 0.04	1
Si IV	0		< 12.66	2
		$z_{\rm sys} = 0.09658$		
H I	0	40 ± 2	14.65 ± 0.05	1
C IV	0		< 12.90	2
N V	0		< 12.97	2
O VI	0		13.70 ± 0.20	1
Si IV	0		< 12.64	2
		$z_{\rm sys} = 0.16711$		
H I	-11 ± 3		15.50	1, 3
H I	0 ± 5		16.35	1, 3
O VI	-266 ± 5	52 ± 2	13.90 ± 0.03	3
O VI	-35 ± 2		14.71 ± 0.01	3
		$z_{\rm sys} = 0.18259$		
H I	0 ± 4	33 ± 1	14.69 ± 0.01	2
H I	$+68 \pm 4$	36 ± 2	14.09 ± 0.03	2
N V	0		< 12.83	2
O VI	$+9 \pm 4$	32 ± 3	13.75 ± 0.02	2
O VI	$+82 \pm 4$	21 ± 1	13.88 ± 0.02	2
Si IV	0		< 12.77	2
		$z_{\rm sys} = 0.29762$		
H I	0 ± 5	38 ± 3	13.89 ± 0.05	2
H I	$+65 \pm 15$	42 ± 12	13.34 ± 0.19	2
C III	0		< 12.05	2
N V	0		< 13.13	2
O VI[b]	$+8 \pm 4$	63 ± 4	13.61 ± 0.02	2
		$z_{\rm sys} = 0.36078$		
H I	-24 ± 14	26 ± 8	14.3 ± 0.3	2
H I	0 ± 3	16 ± 1	15.06 ± 0.05	2
H I	$+27 \pm 8$	54 ± 6	14.29 ± 0.08	2
H I	$+151 \pm 4$	45 ± 4	13.56 ± 0.04	2
H I[c]	$+557 \pm 3$	41 ± 10	12.75 ± 0.41	2
H I	$+575 \pm 3$	22 ± 5	13.11 ± 0.14	2
C III	+168		< 12.5	2
C III[c]	$+557 \pm 3$	12	12.48 ± 0.07	2
N V	+168		< 13.1	2
N V[c]	$+557 \pm 3$	11	13.01 ± 0.08	2
O VI[b]	-44 ± 7	64 ± 9	13.38 ± 0.05	2
O VI	$+168 \pm 3$	30 ± 1	13.80 ± 0.01	2
O VI[c]	$+557 \pm 3$	10	13.36 ± 0.05	2
		$z_{\rm sys} = 0.49510$		
H I	0	53 ± 1	14.09 ± 0.03	4
H I	+93	21 ± 2	13.44 ± 0.09	4
O VI	−3	35 ± 1	14.29 ± 0.02	4
O VI	+48	19 ± 2	13.80 ± 0.07	4

[a] 1: Prochaska et al. 2004; 2: this work;
3: Savage et al. 2010; 4: Narayanan et al. 2011.
[b] Tentative detection due to contamination of the λ1037 member.
[c] Measurements obtained with a simultaneous fit to the transitions assuming that these absorbers originate in the same gas.

are necessary to produce a reasonable χ^2 value. For non-detections, we calculated the 3-σ rest-frame equivalent width limit over a 300 km s^{-1} spectral window (significantly broader than the wings of the COS LSF) and converted this to the corresponding 3-σ limit in column density assuming that the gas is optically thin. The results are summarized in Table 2.3, where we list for each species the velocity offset Δv relative to the systemic redshift of each absorber $z_{\rm sys}$ as defined by the dominant H I component, the Doppler parameter b, and the best-fit column density. We also include in Table 2.3 measurements from the literature for completeness. Here we briefly describe the properties of newly detected absorption features.

At $z = 0.1826$ and 0.1829, two O VI components were found in previous searches (Prochaska et al., 2004; Thom & Chen, 2008b). We confirm both detections and remeasure the absorber properties with a simultaneous fit of both components in the COS data. The lower-redshift O VI component is characterized by an O VI column density log N(O VI) = 13.75 ± 0.02 and Doppler width $b = 32 \pm 3$ km s^{-1}, and is merely ≈ 9 km s^{-1} offset from a previously identified H I absorption component with log N(H I) = 14.69 ± 0.01 and $b = 33 \pm 1$ km s^{-1}. The higher-redshift O VI component is characterized by log N(O VI) = 13.88 ± 0.02 and $b = 21 \pm 1$ km s^{-1}. No other ions have been detected with a 3-σ upper limit of log $N < 12.8$ for both N V and Si IV absorption. Prochaska et al. (2004) reported an upper limit of log $N < 12.4$ for C III absorption. The best-fit Voigt profiles of the O VI doublet along with those of Lyα and Lyβ absorption are presented in the left column of Figure 2.4).

At $z = 0.2977$, we report a tentative detection of an O VI absorber at $\Delta v \approx 8$ km s^{-1} from a previously identified Lyα absorber. The O VI absorption profile is relatively broad with log N(O VI) = 13.61 ± 0.02 and $b \approx 60$ km s^{-1}. The λ1037 member is detected at a ≈ 7-σ level of significance, but the model slightly over-predicts the absorption strength of this weaker member which appears to be contaminated by other absorption features. No other metal absorption is detected in the COS spectrum. Our Voigt profile analysis shows that the Lyα transition is best described by two components separated by $\Delta v = 65$ km s^{-1}, with

Figure 2.4: Absorption profiles and Voigt profile fits in the field of PKS 0405−123

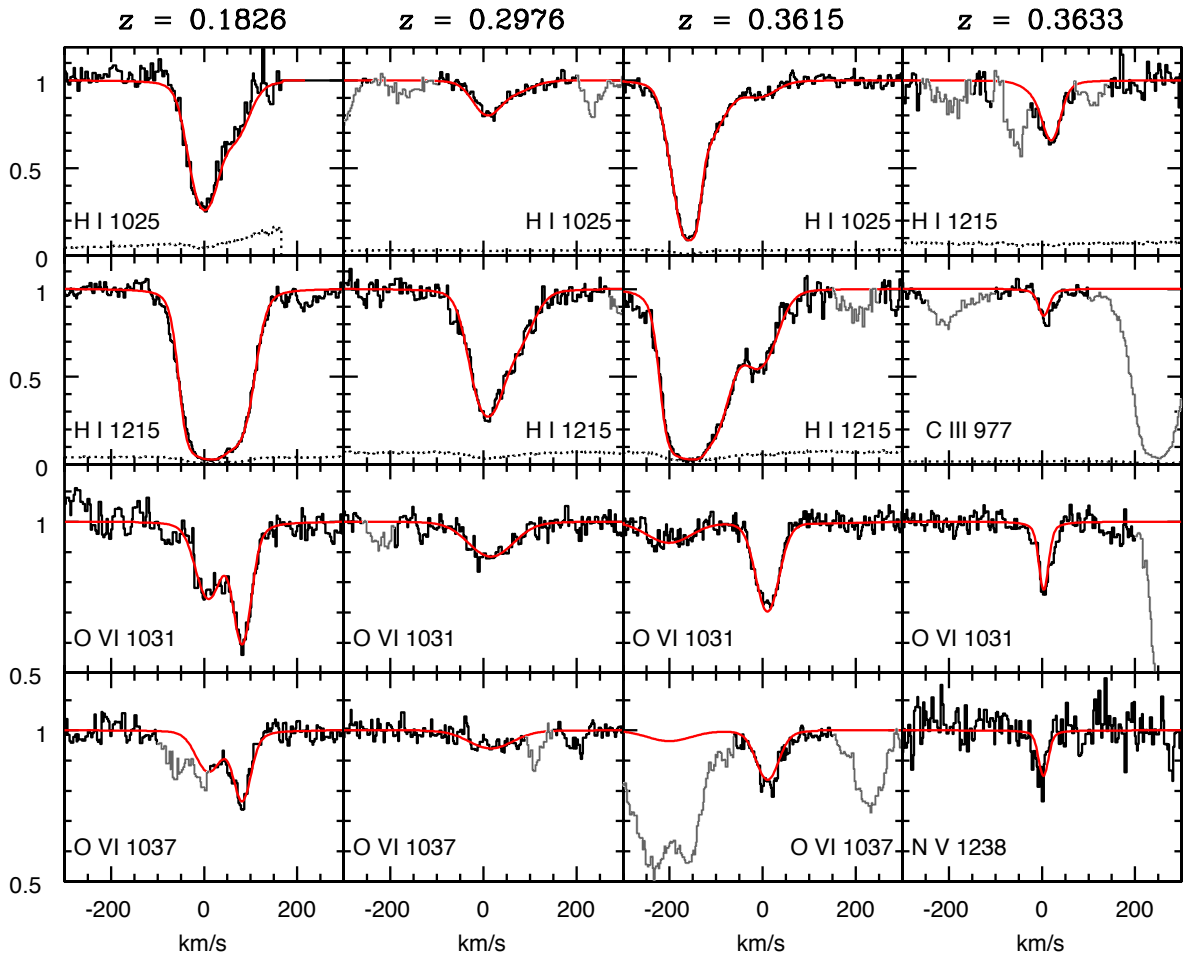

Absorption profiles of two O VI absorbers and a tentative detection (left three columns) and the N V doublet detected in a known metal-line absorber (right column) in the high-quality COS spectrum, along with the associated H I Lyα and/or Lyβ transition. The continuum normalized spectrum is shown in black solid line and the associated 1-σ errors are plotted in black dotted line. The best-fit model profiles from a Voigt profile analysis (§ 2.3) are shown in red. Spectral regions contaminated by other absorption systems are plotted in gray. We do not plot data at velocities greater than $\Delta v > +120$ km s^{-1} for the Lyβ line of the $z = 0.1826$ absorber because in this range, the quasar flux is nearly completely attenuated by Milky Way Lyα absorption. We consider the O VI absorber at $z = 0.2977$ a tentative detection, because the observed depth of the λ1037 member appears shallower than the expectation of the doublet based on the fit of the λ1031 member. Note that the bottom two rows are shown with a partial y-range from 0.5 to 1.2 to improve the visibility of weak features. This partial y-range prevents the errors from being displayed in the bottom two rows.

Table 2.4: Summary of line properties of strong Lyα absorbers with no detectable O VI absorption in the spectrum of PKS 0405−123

Element	Δv (km s^{-1})	b (km s^{-1})	log N / cm^{-2}	References[a]
		$z_{\rm sys} = 0.08139$		
H I	0	54 ± 4	13.79 ± 0.02	1
O VI	0		< 13.62	2
		$z_{\rm sys} = 0.13233$		
H I	0	22 ± 2	13.64 ± 0.03	1
H I	+193	32 ± 6	13.29 ± 0.06	1
C IV	0		< 12.94	3
N V	0		< 12.97	3
O VI	0		< 12.95	3
Si IV	0		< 12.83	3
		$z_{\rm sys} = 0.15304$		
H I	−208	22 ± 2	13.54 ± 0.04	1
H I	0	46 ± 3	13.80 ± 0.03	1
C IV	0		< 13.30	3
N V	0		< 12.71	3
O VI	0		< 13.14	3
Si IV	0		< 12.56	3
		$z_{\rm sys} = 0.16121$		
H I	0	54 ± 8	13.71 ± 0.04	1
H I	+75	18 ± 4	13.27 ± 0.09	1
N V	0		< 13.11	3
O VI	0		< 12.85	3
Si IV	0		< 12.42	3
		$z_{\rm sys} = 0.17876$		
H I	0	55 ± 7	13.61 ± 0.04	1
C III	0		< 12.37	3
N V	0		< 13.13	3
O VI	0		< 13.16	3
		$z_{\rm sys} = 0.24554$		
H I	−99	54 ± 24	13.23 ± 0.11	1
H I	0	23 ± 2	13.69 ± 0.03	1
O VI	0		< 12.89	3
Si IV	0		< 12.53	3
		$z_{\rm sys} = 0.33402$		
H I	0	30 ± 2	13.82 ± 0.03	1
N V	0		< 13.04	3
O VI	0		< 13.12	3
		$z_{\rm sys} = 0.35099$		
H I	0	38 ± 2	14.25 ± 0.03	1
H I	+115	25 ± 5	13.53 ± 0.05	1
H I	+251	31 ± 5	13.57 ± 0.05	1
C III	0		< 12.14	3
N V	0		< 13.05	3
O VI	0		< 13.00	3
		$z_{\rm sys} = 0.40571$		
H I	0	33 ± 2	14.98 ± 0.02	1
C III	0		< 12.00	3
N V	0		< 13.10	3
O VI	0		< 13.28	3

[a] 1: Lehner et al. 2007; 2: from FUSE data published in Prochaska et al. 2004; 3: this work; 4: Williger et al. 2006

Table 2.4 Continued.

Element	Δv (km s^{-1})	b (km s^{-1})	log N / cm^{-2}	References[a]
		$z_{\rm sys} = 0.40886$		
H I	0	40 ± 2	14.38 ± 0.03	1
H I	+149	26 ± 6	13.58 ± 0.07	1
N V	0		< 13.12	3
O VI	0		< 13.28	3
		$z_{\rm sys} = 0.53830$		
H I	0	23 ± 4	14.22 ± 0.06	4
C III	0		< 12.35	3
O VI	0		< 13.26	3

[a] 1: Lehner et al. 2007; 2: from FUSE data published in Prochaska et al. 2004; 3: this work; 4: Williger et al. 2006

one component containing log N(H I) $= 13.89 \pm 0.05$ at $z = 0.2976$ and the other containing log N(H I) $= 13.34 \pm 0.2$ at $z = 0.2979$. The best-fit Voigt profiles of the O VI doublet along with those of Lyα and Lyβ absorption are presented in the middle-left column of Figure 2.4).

At $z = 0.3615$, we also report the detection of a new O VI component with log N(O VI) $= 13.80 \pm 0.01$ and $b = 30 \pm 1$ km s^{-1} at $\Delta v = +170$ km s^{-1} from a previously known absorption complex at $z = 0.3608$ (e.g. Prochaska et al. 2004). Similarly to the O VI absorber at $z = 0.1829$, we do not detect additional metal-line systems associated with this new O VI component. There is possible O VI absorption at $z \approx 0.3608$ with log N(O VI) $= 13.38 \pm 0.05$ detected in the COS spectrum, but it cannot be confirmed due to contaminating features at the location of the second doublet member. The best-fit Voigt profiles of the O VI doublet along with those of Lyα and Lyβ absorption are presented in the middle-right column of Figure 2.4).

Finally, the O VI absorption system previously identified at $z = 0.3633$ with log N(O VI) $= 13.36 \pm 0.05$ and $b = 10 \pm 1$ km s^{-1} displays possible presence of associated N V doublet in the new COS spectrum. Prochaska et al. (2004) identified H I, O IV, N IV, and C III absorption associated with this O VI absorber, although the H I absorbing component is $\Delta v = +20$ km s^{-1} away from the O VI absorber. We confirm the presence of C III absorption with log N(C III) $= 12.48 \pm 0.07$ and detect N V with N(N V) $= 13.01 \pm 0.08$ at the redshift of

the O VI absorber. The measurements were obtained based on a simultaneous fit of Voigt profiles to all three transitions, assuming that these ions originate in the same gas. Allowing independent fits to the line centroids of N V and C III does not improve the model-fit. The best-fit Voigt profiles of Lyα , C III λ 977, O VI λ 1031 and N V λ 1238 are presented in the right column of Figure 2.4). Both O^{5+} and N^{4+} are highly ionized species, whereas C^{2+} is at a much lower ionization state. The presence of these ions together strongly support a scenario of photo-ionization by the extragalactic UV background for the absorbing gas (see Prochaska et al. 2004). Based on the observed relative abundance of C^{2+} and O^{5+}, Prochaska et al. 2004 derived an ionization parameter of $\log U = -1.4 \pm 0.2$ and a minimum metallicity of solar for the absorbing gas assuming that all of the observed N(H I) is associated with the O VI absorbing gas.

Including the tentative detection of an O VI absorber at $z = 0.2977$, we have a total of seven O VI absorbers along the sightline toward PKS 0405−123. In addition, this sightline contains additional 11 strong Lyα absorption systems of $\log N(\mathrm{H\,I}) > 13.6$ (Williger et al., 2006; Lehner et al., 2007)[6] with no detectable absorption from heavy ions. The high S/N of the COS spectrum enables stronger limits (cf. Prochaska et al., 2004) on the associated O VI column densities. In some cases, these limits are comparable to O VI absorption levels seen in the Milky Way ISM (e.g. Rogerson et al., 1973; Jenkins & Meloy, 1974; York, 1974), and are sufficient to rule out the presence of conductively evaporating clouds which are expected to produce absorption with $N(\mathrm{O\,VI}) \sim 10^{13}\,\mathrm{cm}^{-2}$ (e.g. Gnat et al., 2010). We define a subsample of "Lyα-only" absorbers of these strong Lyα absorbers with no associated O VI absorption to a sensitive upper limit. The properties of these Lyα-only systems are summarized in Table 2.4.

6. We associate the H I components identified by Lehner et al. (2007) with one another provided $|\Delta v| < 300$ km s^{-1}. Lehner et al. (2007) restricted their study to absorbers with $z < 0.5$ so we include systems identified by Williger et al. (2006) at $z > 0.5$ as well. For each system, we adopt the total H I column density and the redshift of the strongest H I component.

2.4 The galaxy environments of O VI and Lyα-only Absorber

The highly complete survey data of faint galaxies in the field around PKS 0405−123 offer a new opportunity to re-examine the galaxy environments of O VI absorbers. In particular, we compare our findings with previous results from a shallower survey which concluded that O VI absorbers trace a diverse set of environments including: the halos of individual galaxies, galaxy groups, filamentary-like structures, and galaxy voids (e.g. Prochaska et al., 2006). In addition, we compare the galaxy environments of the O VI absorbers with those of Lyα-only absorbers which constitutes a control sample in seeking the discriminating galactic features that result in the observed O VI absorbing gas at large galactic radii. Throughout, we associate galaxies with absorbers provided the projected line-of-sight velocity between the absorber and the galaxy is $|\Delta v| < 300$ km s^{-1}. All galaxies spectroscopically identified at impact parameter $\rho < 1$ Mpc and velocity offset $|\Delta v| < 300$ km s^{-1} of the O VI and Lyα-only systems are presented in Tables 2.5 and 2.6, respectively.

The galactic environments of O VI absorbers uncovered in our survey are presented in Figure 2.5. We find that O VI primarily traces over-dense galaxy environments with at least one emission-line galaxy found within $\rho \approx 300$ kpc. Specifically, the O VI absorber at $z = 0.0918$ was originally attributed to filamentary structure connecting three galaxy groups at $\rho = 1 - 3$ Mpc (Prochaska et al. 2006). However, we have uncovered four dwarf, emission-line galaxies at $\rho \leq 300$ kpc, the closest of which is at $\rho = 70$ kpc and $\Delta v = +140$ km s^{-1}. Similarly, the absorbers at $z \approx 0.3608$ had been attributed to the intragroup medium of a group of passive galaxies found at $\rho = 1 - 3$ Mpc. Our survey has revealed a dwarf emission-line galaxy ($L = 0.08\,L_*$ at $\rho = 320$ kpc and $\Delta v \approx 0$ km s^{-1}) in addition to the known massive absorption-line galaxy previously found at $\rho = 230$ kpc. The only intriguing exception is the O VI absorption system at $z \approx 0.183$, which exhibits two strong components separated by 70 km s^{-1}. This O VI absorber does not have an associated galaxy at $\rho < 300$ kpc. Our galaxy survey rules out the presence of any galaxies of $L > 0.04\,L_*$ at $\rho < 250$ kpc

Figure 2.5: The galaxy environments of O VI absorbers and strong Lyα absorbers of log N(H I) > 13.6 with no detectable O VI (designated as "Lyα-only" systems) in the field of PKS 0405−123.

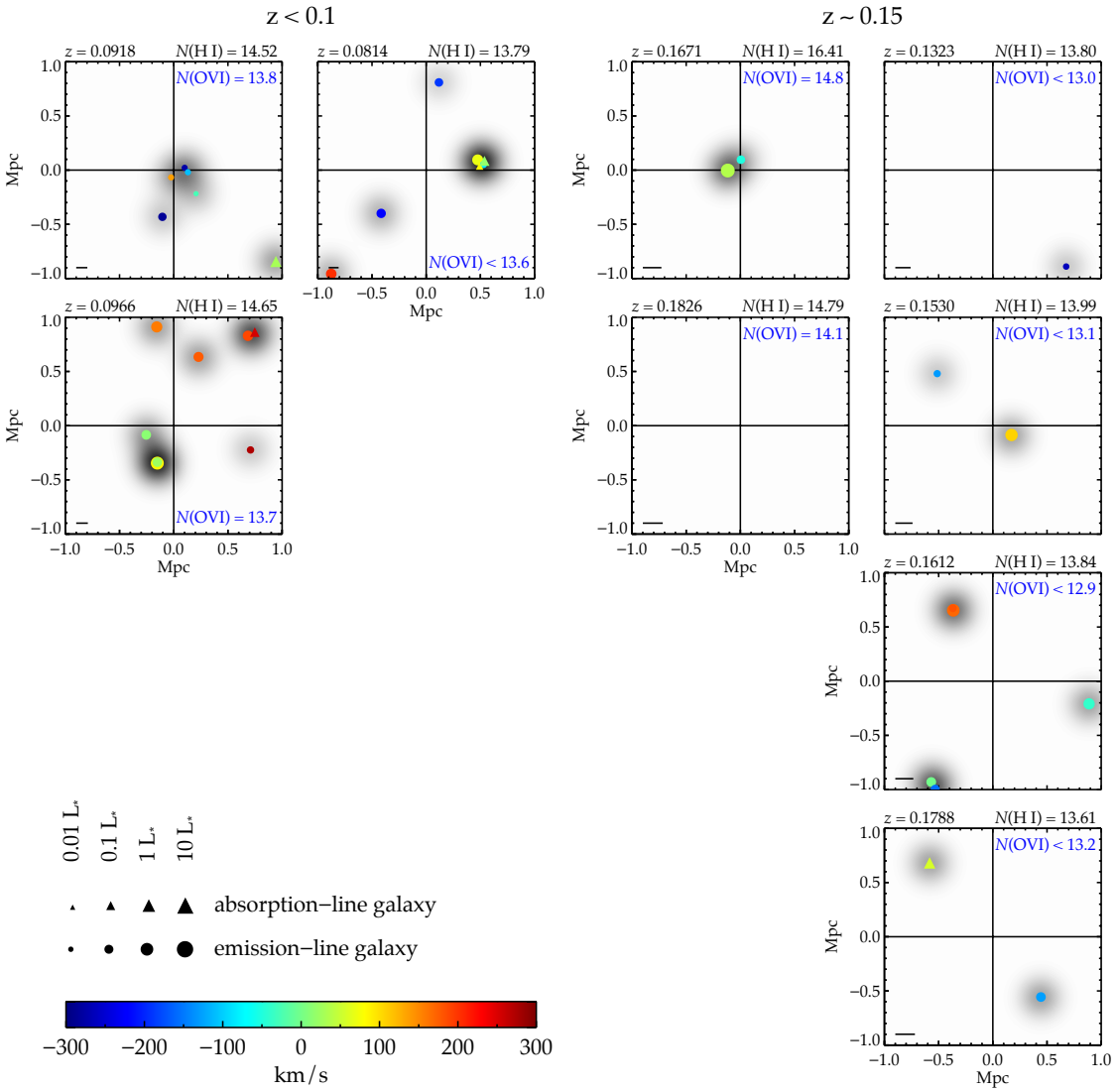

Considering the increasing survey incompleteness of faint ($< 0.1\,L_*$) galaxies with increasing redshift, we separate the galaxy–absorber sample into four redshift bins. For each redshift bin, we show the spatial and velocity distributions of galaxies around O VI absorbers in the left column and Lyα-only absorbers in the right column. Each panel is centered at the quasar, while positions of galaxies with projected line-of-sight velocity $|\Delta v| < 300$ km s^{-1} of the absorber are marked with circles for emission-line galaxies and triangles for absorption-line galaxies. The symbols are color-coded to indicate the line-of-sight velocity between each galaxy and the absorber. The symbol size specifies galaxy luminosity as shown in the figure legend. To help visualize the surface density of surrounding galaxies, we also introduce a gray-scale showing a luminosity-weighted galaxy surface density where each galaxy is represented by a Gaussian with FWHM = 300 kpc. The luminosity weighting assigns $L \geq L_*$ galaxies a peak of 1, $0.1 \leq L < L_*$ galaxies a peak of 0.7 and $L < 0.1\,L_*$ galaxies a peak of 0.4.

Figure 2.5 continued.

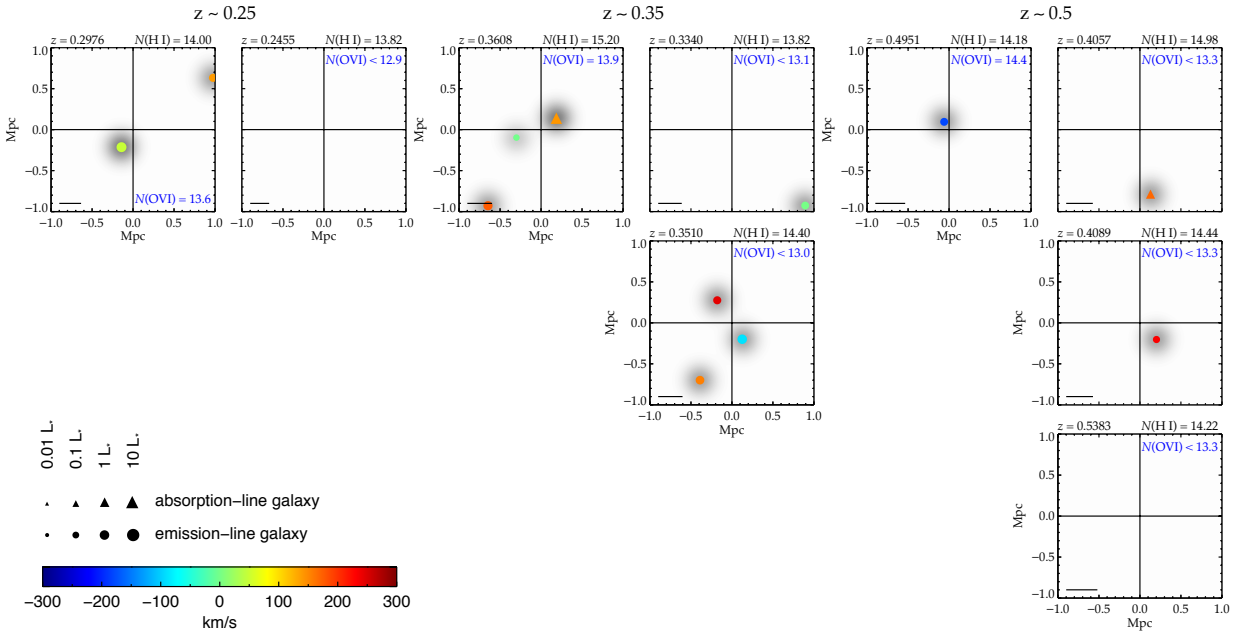

and the presence of any galaxies of $L > 0.3\,L_*$ at $\rho < 1$ Mpc. The lack of galaxies found in the vicinity suggests that this metal-enriched absorber resides in an apparent void. Finally, the O VI absorber at $z = 0.495$ with associated Ne VIII doublet (Narayanan et al. 2011) is found to be associated with an emission-line galaxy at $\rho = 110$ kpc (Chen & Mulchaey 2009). Our new survey has not uncovered any additional galaxies in the vicinity of the absorber. We are able to rule out the presence of any galaxies with $L > 0.1\,L_*$ at $\rho < 200$ kpc.

We also present in Figure 2.5 the galaxy environments of O VI and Lyα-only absorbers. Considering the increasing survey incompleteness of faint ($< 0.1\,L_*$) galaxies with increasing redshift, we separate the galaxy–absorber sample into four redshift bins. For each redshift bin, we show the spatial and velocity distributions of galaxies around O VI absorbers in the left column and Lyα-only absorbers in the right column. Each panel is centered at the quasar, while galaxy positions are marked with circles for emission-line galaxies and triangles for absorption-line galaxies. The symbols are color-coded to indicate the line-of-sight velocity between each galaxy and the absorber. The symbol size specifies galaxy luminosity as shown in the figure legend. To help visualize the surface density of surrounding galaxies, we also

Figure 2.6: Mean radial profiles of the galaxy distribution around O VI and Lyα-only absorbers in the field of PKS 0405−123

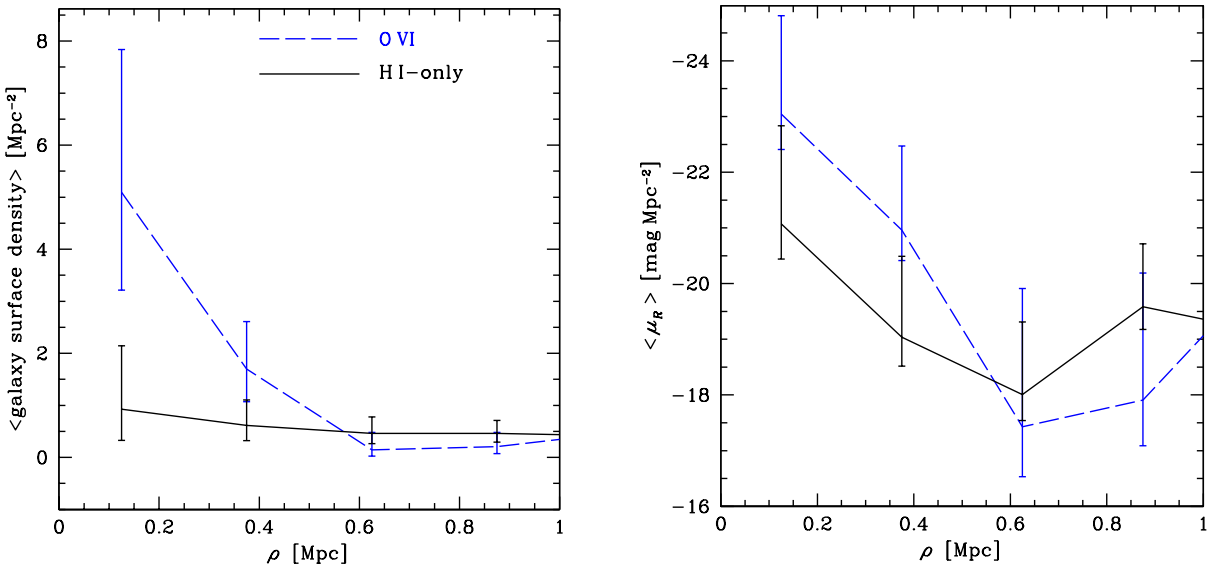

The *left* panel shows the mean surface density of galaxies versus projected distance around O VI (dashed line) and Lyα-only (solid line) absorbers, and the *right* panel shows the mean surface brightness profiles. Error-bars are computed from 68% Poisson confidence intervals. It is clear that there exists an overdensity of galaxies within $\rho \approx 500$ kpc radius of O VI absorbers, which is not seen around Lyα-only absorbers. Similarly, the mean galaxy surface brightness profile around O VI absorbers exhibits a steep rise by $\Delta\mu_R \approx +5\,\mathrm{mag\,Mpc^{-2}}$ toward the inner regions at $\rho \lesssim 500$ kpc, while the galaxy surface brightness profile around Lyα-only absorbers remains comparatively flat with $\Delta\mu_R \approx +2\,\mathrm{mag\,Mpc^{-2}}$ though the uncertainties are larger.

introduce a gray-scale showing luminosity-weighted galaxy surface density where each galaxy is represented by a Gaussian with FWHM = 300 kpc.

A qualitative finding based on Figure 2.5 is that a larger fraction of Lyα-only absorbers appear in underdense or relatively isolated galaxy environments in comparison to those of O VI absorbers. Considering all the absorbers together, six of the seven O VI absorption systems at $z < 0.5$ along the sightline are associated with at least one galaxy with $\rho \lesssim 300$ kpc. Four of the six O VI absorption systems at $z < 0.4$ are found in a group of multiple galaxies with $\rho \lesssim 300$ kpc. In contrast, of the 11 additional Lyα-only absorbers, only three have associated galaxies found at $\rho < 300$ kpc.

To quantify the potential difference in the observed galactic environments between O VI and Lyα-only absorbers, we perform two separate tests in the following discussion. First, we examine the mean radial profiles of galaxy properties averaged over all systems in each subsample. Second, we examine the distribution of galaxy properties within each subsample. In both tests, the comparisons are based on both the surface density of the galaxies and the surface brightness of star light.

2.4.1 Do O VI and Lyα*-only absorbers share similar azimuthally averaged galaxy distributions out to 1 Mpc?*

To determine whether or not O VI and Lyα-only absorbers occur in similar galaxy environments, we measure the mean radial profile of the galaxy distribution around these absorbers by first stacking the observed 2D distribution of galaxies around individual absorbers shown in Figure 2.5 and then computing an azimuthal average in annuli with increasing radius. The left panel of Figure 2.6 displays the mean galaxy surface density profiles around O VI absorbers (dashed line) and Lyα-only absorbers (solid line). Error-bars show our estimate of uncertainties due to counting statistics (e.g. Gehrels, 1986). It is clear that there exists an overdensity of galaxies within a $\rho \approx 500$ kpc radius of O VI absorbers, which is not seen

around Lyα-only absorbers.

Such a distinction between O VI and Lyα-only absorbers is also seen in the observed mean surface brightness profiles around these absorbers (the right panel of Figure 2.6) though with significantly larger uncertainties. While the mean galaxy surface brightness profile around O VI absorbers exhibits a steep rise of $\Delta\mu_R \approx +5\,\mathrm{mag\,Mpc^{-2}}$ toward the inner regions at $\rho \lesssim 500$ kpc, only a mild increase of $\Delta\mu_R \approx +2\,\mathrm{mag\,Mpc^{-2}}$ is seen in the galaxy surface brightness profile around Lyα-only absorbers.

2.4.2 Do O VI and Lyα*-only absorbers share similar galaxy distribution functions in the inner 500 kpc?*

The exercise presented in § 2.4.1 shows that the ensemble average of the radial profiles of galaxy surface density and surface brightness exhibit different characteristics at $\rho \lesssim 500$ kpc between O VI and Lyα-only absorbers. Here we focus on the inner regions of $\rho = 500$ kpc radius around individual absorbers and examine whether there is a difference in the distribution of galaxy properties within each subsample. This exercise provides further insights into the immediate galactic environments of individual absorbers.

The left panel of Figure 2.7 shows the cumulative fraction of absorbers originating in environments of no more than $N_{\rm gal}$ galaxies. It shows that while 16% of O VI absorbers occur in environments where no galaxies are found within a radius of $\rho = 500$ kpc, more than 50% of Lyα-only absorbers occur in such "voids". However, the samples are small and a two-population Kolmogorov-Smirnov (KS) test finds a p-value of 0.2.

Next, we examine the mean surface density of star light averaged over the area within 500 kpc radius in units of rest-frame R-band magnitude per square Mpc. This quantity allows us to account for missing galaxies that are too faint to be detected in our survey by including the survey limit in our analysis. Including non-detections, the right panel of Figure 2.7 shows the maximum possible cumulative fraction of absorbers arising in environments with mean galaxy

Figure 2.7: Cumulative distribution of galaxy environment near O VI and Lyα-only absorbers in the field of PKS 0405−123.

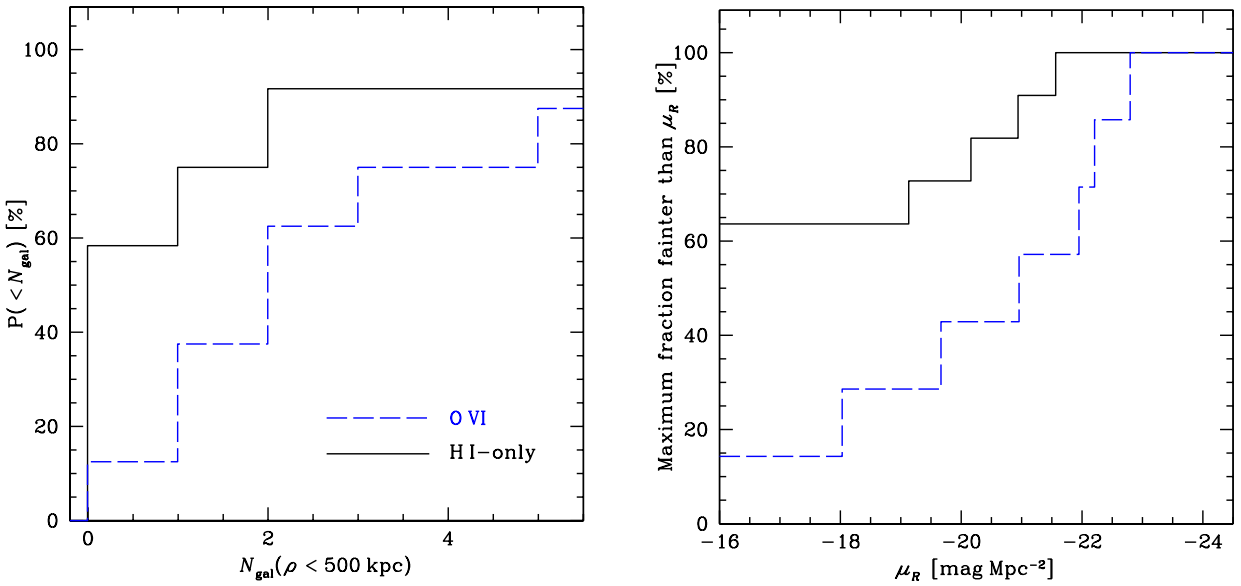

Cumulative fraction of absorbers originating in environments with no more than $N_{\rm gal}$ galaxies within a radius of $\rho = 500$ kpc (*left panel*) and with mean surface brightness (averaged over the area of 500 kpc radius) fainter than rest-frame R-band magnitude μ_R per square Mpc (*right panel*). While a larger fraction of Lyα-only absorbers ($> 50\%$ versus 16% for O VI absorbers) arise in environments where no luminous galaxies are found within a radius of $\rho = 500$ kpc, no statistically significant distinction can be made between the cumulative fraction of galaxy surface density around O VI and Lyα-only absorbers based on these small samples. Specifically, Kolmogorov-Smirnov (KS) tests on their cumulative distribution functions find p-values of 0.2 (galaxy density) and 0.08 (surface brightness).

surface brightness fainter than the designated value μ_R. Similar to the surface density plot in the left panel, we find that as much as 60% of Lyα-only absorbers originate in environments with galaxy surface brightness fainter than than $\mu_R \approx -19\,\mathrm{mag\,Mpc^{-2}}$, while no more than 35% of O VI absorbers are found in such low surface brightness environments. A KS test on the O VI and Lyα-only surface brightness distributions finds a p-value of 0.08.

2.5 Discussion and Conclusions

The high level of completeness achieved at faint magnitudes by our survey has allowed us to probe the galaxy populations to low luminosities and obtain better understanding of the nature of the absorbing systems. We have shown that O VI absorbers previously attributed to a gaseous medium connecting massive galaxy groups are, in fact, more closely associated with less massive groups containing at least one dwarf, emission-line galaxy. In total, four of seven known O VI absorbers along the PKS 0405−123 sightline reside in galaxy "groups" that contain at least one star-forming member. Two of the seven are found nearby to an emission-line galaxy and only one O VI absorber is found in a galaxy void. Therefore, we conclude that O VI absorbers primarily trace gas-rich environments as indicated by the presence of at least one low-mass, emission-line galaxy seen in our survey. However, the presence of O^{5+} ions could either be the result of starburst driven outflows or due to stripped material from galaxy interactions that also trigger star formation.

This is in stark contrast to lower ionization transitions such as Mg II that are found to reside primarily in the halos of isolated galaxies both with and without star formation (Steidel et al., 1997). One exception is those ultra-strong Mg II absorbers with rest-frame absorption equivalent width $W_r(2796) > 3$ Å. Three of these ultra-strong Mg II systems have been targeted for follow-up galaxy surveys and all three are found in groups containing multiple super-L_* galaxies (e.g. Whiting et al., 2006; Nestor et al., 2011; Gauthier, 2013), with an inferred group halo mass of $M_h \sim 10^{13}\,\mathrm{M_\odot}$. The galaxy "groups" found around O VI

absorbers in our survey contain primarily low-luminosity (and presumably low-mass) galaxies (see also Mulchaey & Chen, 2009), and are therefore not as massive as those found near ultra-strong Mg II absorbers. A detailed comparison of the dynamics between galaxies and absorbing gas may lead to further insights into the physical origin of these O VI absorbers.

In addition, our analysis reveals a clear distinction in the radial profiles of mean galaxy surface density and surface brightness around different absorbers. Specifically, O VI absorbers are found to reside in galaxy overdensities with significantly higher mean galaxy surface density and surface brightness at $\rho \lesssim 500$ kpc, while only a mild increase in galaxy surface brightness is seen at small ρ around strong Lyα-only absorbers.

On the other hand, Chen & Mulchaey (2009) showed that both strong Lyα absorbers of $\log N(\mathrm{H\,I}) \geq 14$ and O VI absorbers exhibit a comparable clustering amplitude as emission-line dominated galaxies. The apparent discrepancy between the finding of this chapter and those of Chen & Mulchaey (2009) may be explained by the intrinsic difference in the sample definition. Our current study is based on galaxies and absorbers found in a single field, and therefore limited by the small sample size. In particular, we have defined a controlled Lyα-only sample that includes Lyα absorbers that are as weak as $\log N(\mathrm{H\,I}) \approx 13.6$ in order to have a sufficiently large sample for a statistical analysis. In contrast, the O VI absorbers in the comparison sample all have associated Lyα with $\log N(\mathrm{H\,I}) > 14$. It is therefore unclear whether the observed distinction between the galactic environments of O VI and Lyα-only absorbers represents a fundamental difference between metal and H I absorbers, or between high and low H I column density clouds. We expect that such uncertainty in the interpretation of the observations will be resolved with a larger sample of galaxy and absorber data from different fields complemented by multi-band imaging data. Together, these data will help constrain galaxy star-formation rates and reveal the presence of any faint tidal features (e.g. Chen & Mulchaey, 2009).

Lastly, an intriguing outcome of our deep galaxy survey is the discovery of an O VI

absorber that is likely to reside in a "void". This O VI absorption system at $z \approx 0.183$, which exhibits two strong components separated by 70 km s^{-1}, does not have other ionic transitions detected to sensitive limits (Table 3; see also Prochaska et al. 2004). Our galaxy survey data rule out the presence of any galaxies of $L > 0.04\,L_*$ at $\rho < 250$ kpc or the presence of any galaxies of $L > 0.3\,L_*$ at $\rho < 1$ Mpc. The lack of additional ionic transitions associated with this absorber suggests that the gas may be hot and collisionally ionized. Also, the lack of galaxies found in the vicinity suggests that this absorber resides in an apparent void, similar to an O VI absorber at z=0.06807 for which Tripp et al. (2006) ruled out the presence of galaxies of $L > 0.04\,L_*$ at $\rho < 200$ kpc. While a likely explanation for the origin of the gas is the warm-hot intergalactic medium, it is unclear whether the relatively narrow line width is consistent with a diffuse intergalactic origin.

Acknowledgements

It is a pleasure to thank Jean-René Gauthier and the anonymous referee for helpful comments that significantly improved the manuscript. We thank Edward Villanueva and Daniel Kelson for their help with the COSMOS reduction pipeline and Joe Hennawi for his aid with the Low-Redux reduction pipeline. We made extensive use of the XIDL library provided by Jason Prochaska. We are grateful for the support provided by the staff at the Las Campanas Observatory and the Apache Point Observatory. SDJ acknowledges funding from a National Science Foundation Graduate Research Fellowship and a fellowship from the Illinois Space Grant Consortium. This research has made use of the NASA Astrophysics Data System and the NASA/IPAC Extragalactic Database (NED) which is operated by the Jet Propulsion Laboratory, California Institute of Technology, under contract with the National Aeronautics and Space Administration. This chapter contains data obtained with the 6.5-m Magellan Telescopes located at Las Campanas Observatory, Chile and data obtained with the Apache Point Observatory 3.5-meter telescope, which is owned and operated by the

Table 2.5: Summary of spectroscopically identified galaxies at $\rho < 1$ Mpc and $|\Delta v| < 300$ km s^{-1} of O VI absorbers in the spectrum of PKS 0405−123

ID	R.A. (J2000)	Decl. (J2000)	$\Delta\alpha$ ($''$)	$\Delta\delta$ ($''$)	$\Delta\theta$ ($''$)	ρ (kpc)	R (mag)	$z_{\rm spec}$	galaxy class[a]	L/L_*
$z_{\rm sys} = 0.09180$	$\log N({\rm H\,I}) = 14.52$		$\log N({\rm O\,VI}) = 13.83$		$N_{\rm gal} = 5$					
1835	04:07:49.4	-12:12:16	14.2	−39.3	41.8	71	21.31 ± 0.10	0.0923	E	0.02
2055	04:07:44.4	-12:11:24	−59.1	12.7	60.4	102	21.30 ± 0.09	0.0908	E	0.02
2080	04:07:43.2	-12:11:48	−76.7	−11.3	77.5	132	21.27 ± 0.09	0.0914	E	0.02
2212	04:07:40.2	-12:13:44	−120.7	−127.3	175.4	299	21.94 ± 0.13	0.0917	E	0.01
1698	04:07:52.6	-12:15:49	61.1	−252.3	259.6	439	19.74 ± 0.07	0.0908	E	0.07
$z_{\rm sys} = 0.09658$	$\log N({\rm H\,I}) = 14.65$		$\log N({\rm O\,VI}) = 13.70$		$N_{\rm gal} = 5$					
1457	04:07:58.1	-12:12:24	141.8	−47.3	149.5	267	19.03 ± 0.07	0.0966	E	0.15
1602	04:07:54.2	-12:14:45	84.6	−188.3	206.5	370	19.01 ± 0.07	0.0967	E	0.15
1601	04:07:54.2	-12:14:50	84.6	−193.3	211.0	379	16.74 ± 0.06	0.0969	E	1.24
2254	04:07:39.7	-12:05:42	−128.0	354.7	377.1	679	18.74 ± 0.07	0.0973	E	0.20
1659	04:07:54.4	-12:03:07	87.5	509.7	517.1	931	17.99 ± 0.06	0.0972	E	0.39
$z_{\rm sys} = 0.16711$	$\log N({\rm H\,I}) = 16.41$		$\log N({\rm O\,VI}) = 14.77$		$N_{\rm gal} = 2$					
80006	04:07:48.3	-12:11:03	−1.9	33.7	33.7	96	21.04 ± 0.00	0.1669	E	0.08
1753	04:07:51.2	-12:11:38	40.6	−1.3	40.6	116	17.43 ± 0.06	0.1672	E	2.13
$z_{\rm sys} = 0.18259$	$\log N({\rm H\,I}) = 14.79$		$\log N({\rm O\,VI}) = 14.12$		$N_{\rm gal} = 0$					
no galaxies of $L > 0.04\,L_*$ at $\rho < 250$ kpc and no galaxies of $L > 0.3\,L_*$ at $\rho < 1$ Mpc										
$z_{\rm sys} = 0.29762$	$\log N({\rm H\,I}) = 14.00$		$\log N({\rm O\,VI}) = 13.61$		$N_{\rm gal} = 1$					
1786	04:07:50.6	-12:12:25	31.8	−48.3	57.9	256	19.34 ± 0.07	0.2978	E	1.38
$z_{\rm sys} = 0.36078$	$\log N({\rm H\,I}) = 15.20$		$\log N({\rm O\,VI}) = 13.94$		$N_{\rm gal} = 2$					
1967	04:07:45.9	-12:11:09	−37.1	27.7	46.3	233	18.58 ± 0.07	0.3614	A	4.47
1716	04:07:52.5	-12:11:56	59.7	−19.3	62.7	316	23.01 ± 0.21	0.3608	E	0.08
$z_{\rm sys} = 0.49510$	$\log N({\rm H\,I}) = 14.18$		$\log N({\rm O\,VI}) = 14.41$		$N_{\rm gal} = 1$					
1862	04:07:49.1	-12:11:21	9.8	15.7	18.5	112	22.63 ± 0.17	0.4942	E	0.25

[a] galaxy classification: E→ emission-line dominated, A→ absorption-line dominated.

Astrophysical Research Consortium.

Table 2.6: Summary of spectroscopically identified galaxies at $\rho < 1$ Mpc and $|\Delta v| < 300$ km s^{-1} of Lyα-only absorbers in the spectrum of PKS 0405−123

ID	R.A. (J2000)	Decl. (J2000)	$\Delta\alpha$ ($''$)	$\Delta\delta$ ($''$)	$\Delta\theta$ ($''$)	ρ (kpc)	R (mag)	$z_{\rm spec}$	galaxy class[a]	L/L_*
$z_{\rm sys} = 0.08139$	$\log N({\rm H\,I}) = 13.79$		$\log N({\rm O\,VI}) < 13.62$		$N_{\rm gal} = 6$					
2757	04:07:27.3	-12:10:35	−309.8	61.7	315.9	486	17.70 ± 0.06	0.0817	E	0.35
2804	04:07:26.5	-12:11:12	−321.5	24.7	322.5	496	20.11 ± 0.07	0.0817	A	0.04
2860	04:07:24.9	-12:11:03	−345.0	33.7	346.6	530	20.40 ± 0.08	0.0811	E	0.03
2867	04:07:24.5	-12:10:41	−350.9	55.7	355.2	545	18.35 ± 0.07	0.0815	A	0.19
1117	04:08:06.9	-12:15:57	270.8	−260.3	375.6	571	18.81 ± 0.07	0.0806	E	0.12
2110	04:07:43.2	-12:02:49	−76.7	527.7	533.2	812	19.36 ± 0.07	0.0807	E	0.07
$z_{\rm sys} = 0.13233$	$\log N({\rm H\,I}) = 13.80$		$\log N({\rm O\,VI}) < 12.95$		$N_{\rm gal} = 0$					
no galaxies of $L > 0.1\,L_*$ at $\rho < 250$ kpc and no galaxies of $L > 0.16\,L_*$ at $\rho < 1$ Mpc										
$z_{\rm sys} = 0.15304$	$\log N({\rm H\,I}) = 13.99$		$\log N({\rm O\,VI}) < 13.14$		$N_{\rm gal} = 2$					
2034	04:07:44.0	-12:12:09	−65.0	−32.3	72.6	193	18.24 ± 0.07	0.1534	E	0.84
1334	04:08:01.6	-12:08:36	193.1	180.7	264.4	701	21.75 ± 0.13	0.1525	E	0.03
$z_{\rm sys} = 0.16121$	$\log N({\rm H\,I}) = 13.84$		$\log N({\rm O\,VI}) < 12.85$		$N_{\rm gal} = 3$					
1503	04:07:57.4	-12:07:41	131.5	235.7	269.9	752	18.19 ± 0.07	0.1619	E	0.99
1504	04:07:57.5	-12:07:34	133.0	242.7	276.7	771	21.45 ± 0.11	0.1619	E	0.05
2784	04:07:26.6	-12:12:52	−320.1	−75.3	328.8	912	19.08 ± 0.07	0.1611	E	0.43
$z_{\rm sys} = 0.17876$	$\log N({\rm H\,I}) = 13.61$		$\log N({\rm O\,VI}) < 13.16$		$N_{\rm gal} = 2$					
2282	04:07:38.4	-12:14:41	−147.1	−184.3	235.8	711	20.46 ± 0.08	0.1783	E	0.15
1345	04:08:01.6	-12:07:51	193.1	225.7	297.0	898	19.25 ± 0.07	0.1790	A	0.46
$z_{\rm sys} = 0.24554$	$\log N({\rm H\,I}) = 13.82$		$\log N({\rm O\,VI}) < 12.89$		$N_{\rm gal} = 0$					
no galaxies of $L > 0.07\,L_*$ at $\rho < 250$ kpc and no galaxies of $L > 0.5\,L_*$ at $\rho < 1$ Mpc										
$z_{\rm sys} = 0.33402$	$\log N({\rm H\,I}) = 13.82$		$\log N({\rm O\,VI}) < 13.12$		$N_{\rm gal} = 0$					
no galaxies of $L > 0.13\,L_*$ at $\rho < 250$ kpc and no galaxies of $L > 0.5\,L_*$ at $\rho < 1$ Mpc										
$z_{\rm sys} = 0.35099$	$\log N({\rm H\,I}) = 14.40$		$\log N({\rm O\,VI}) < 13.00$		$N_{\rm gal} = 3$					
1939	04:07:46.7	-12:12:17	−25.4	−40.3	47.7	235	20.18 ± 0.08	0.3506	E	0.95
1787	04:07:50.9	-12:10:41	36.2	55.7	66.4	329	21.48 ± 0.11	0.3521	E	0.29
1652	04:07:53.8	-12:13:58	78.7	−141.3	161.8	802	20.95 ± 0.09	0.3517	E	0.47
$z_{\rm sys} = 0.40571$	$\log N({\rm H\,I}) = 14.98$		$\log N({\rm O\,VI}) < 13.28$		$N_{\rm gal} = 1$					
80008	04:07:46.8	-12:14:02	−23.9	−145.3	147.3	800	20.93 ± 0.00	0.4065	A	0.69
$z_{\rm sys} = 0.40886$	$\log N({\rm H\,I}) = 14.44$		$\log N({\rm O\,VI}) < 13.28$		$N_{\rm gal} = 1$					
1975	04:07:45.9	-12:12:14	−37.1	−37.3	52.6	287	22.70 ± 0.21	0.4100	E	0.14
$z_{\rm sys} = 0.53830$	$\log N({\rm H\,I}) = 14.22$		$\log N({\rm O\,VI}) < 13.26$		$N_{\rm gal} = 0$					
no galaxies of $L > 0.5\,L_*$ at $\rho < 250$ kpc and no galaxies of $L > 0.5\,L_*$ at $\rho < 1$ Mpc										

[a] galaxy classification: E→ emission-line dominated, A→ absorption-line dominated.

CHAPTER 3

DISCOVERY OF A TRANSPARENT SIGHTLINE AT SMALL PROJECTED DISTANCE TO AN INTERACTING PAIR OF GALAXIES

The contents of this chapter have been published in the Monthly Notices of the Royal Astronomical Society and are reproduced here in accordance with the copyright agreement and with permission from the Oxford University Press.

Johnson, S. D., Chen, H.-W., Mulchaey, J. S., et al. 2014, MNRAS, 438, 3039

3.1 Introduction

The origin of the division of galaxies into the star-forming galaxies in the blue cloud and the more passive ones of the red sequence in color-magnitude diagrams, along with the corresponding division in morphologies, remains one of the most fundamental questions in galaxy evolution (e.g. Hubble, 1936; de Vaucouleurs, 1961; Strateva et al., 2001; Bell et al., 2004; Faber et al., 2007). Galaxies grow by a combination of accreting material from the intergalactic medium (IGM) and mergers (e.g. Genel et al., 2008), but the build-up of the red sequence requires mechanisms that rapidly halt or "quench" star-formation for long time-scales. Possible quenching mechanisms include: shock-heating of accreted gas (e.g. Dekel & Birnboim, 2006), gas stripping due to interactions with a cluster environment (e.g. Moore et al., 1996, 1998; Tonnesen & Bryan, 2009), and winds driven by starbursts or active galactic nuclei (e.g. Springel et al., 2005). One particularly intriguing picture is one in which galaxy mergers transform spirals into ellipticals (e.g. Larson et al., 1980; Barnes, 1989; Schweizer & Seitzer, 1992; Cox et al., 2006; Hopkins & Hernquist, 2009), drive the observed correlations between the passive fraction and galaxy density (e.g. Dressler, 1980; Poggianti et al., 2006), and quench star-formation by stripping gas through galaxy collisions (e.g. Spitzer & Baade,

1951; Toomre & Toomre, 1972; Balogh et al., 2000), or ram-pressure stripping (e.g. Gunn & Gott, 1972; Kenney et al., 2004). Yet despite decades of study, it is not clear whether galaxies are quenched by interaction related processes or intrinsic mechanisms such as a transition from cold-mode to hot-mode accretion.

Proposed quenching mechanisms operate by heating (e.g. Dekel et al., 2009), ejecting (e.g. Kereš et al., 2009), or stripping (in cluster environments; e.g. Balogh et al., 2000) the gaseous halos of galaxies, and consequently, the circumgalactic medium (CGM) provides a sensitive laboratory for studying the physical mechanisms that govern galaxy evolution. The diffuse gas of the CGM is generally too low in density to be directly observed in emission with existing facilities, but it can be studied through the use of rest-frame ultraviolet (UV) absorption features in the spectra of background sources. Over the last two decades, a great deal of effort has gone into constraining the properties of the CGM as a function of galaxy mass, luminosity, morphology, and color through observations of absorption features in the spectra of quasars at small projected distances from galaxies (e.g. Bergeron & Boissé 1991; Morris et al. 1993; Lanzetta et al. 1995; Churchill et al. 1996; Chen et al. 1998, 2001a; Tripp et al. 1998; Chen et al. 2001b; Bowen et al. 2002; Simcoe et al. 2006; Stocke et al. 2006; Wakker & Savage 2009; Chen & Mulchaey 2009; Wakker & Savage 2009; Chen et al. 2010; Gauthier et al. 2010, Steidel et al. 2010, Lovegrove & Simcoe 2011; Prochaska et al. 2011; Tumlinson et al. 2011; Thom et al. 2012; Werk et al. 2013). These studies show that the bimodal distribution of galaxies in color-magnitude diagrams is reflected in the gas content of the CGM. Observations of both H I components and heavy-element species such as O VI and Mg II demonstrate that cool ($T < 10^6$ K) gas is common around passive galaxies but with reduced covering fraction relative to star-forming galaxies (Chen & Mulchaey, 2009; Chen et al., 2010b; Gauthier et al., 2010; Tumlinson et al., 2011; Thom et al., 2012). The mechanisms responsible for quenching star-formation in the red sequence must remove or transform the highly ionized gaseous halos of quenched galaxies while maintaining the lower

ionization-state gas but at reduced levels.

The CGM is likely to be affected by galaxy interactions such as ram-pressure stripping and tidal forces, and studies of the impact of galaxy environment on the CGM may help constrain the relationship between quenching and environmental factors. Nevertheless, while existing studies of the CGM explore a range of galaxy properties, the influence of group and cluster environments on the CGM remains largely unexplored. Group galaxies exhibit more extended Mg II halos than isolated galaxies (Chen et al., 2010a; Bordoloi et al., 2011), and galaxy clusters exhibit an increased incidence of strong Mg II absorbers at $\rho < 1$ Mpc relative to the field (Lopez et al., 2008). At the same time, members of the Virgo cluster show a reduced covering fraction in Lyα absorption relative to galaxies in the field (Yoon et al., 2012). Additional studies that compare the CGM of cluster, group, and field galaxies are warranted.

In this chapter, we report the discovery of a transparent sightline harboring little $T < 10^6$ K gas at a small projected distance to an interacting pair of mature galaxies at $z = 0.12$. The sightline of the UV-bright quasar PG 1522+101 at $z_{\rm em} = 1.328$ passes at a projected distance of $\rho \lesssim 20$ kpc from the galaxy pair (see the right panel of Figure 3.1), enabling a study of the gas at small projected distances from the interacting pair. The galaxies are separated by 9 kpc in projected distance. We refer to the more luminous pair member as G1 and to the less luminous member as G2 throughout the chapter. This discovery represents an extreme example demonstrating the potential impact of galaxy environment on the CGM.

This chapter proceeds as follows. In Section 3.2 we present the imaging and spectroscopy of the galaxy pair as well as the UV and optical spectroscopy of PG 1522+101. In Section 3.3, we discuss the properties of the galaxy pair including: absolute magnitudes, colors, star-formation rates, gas-phase metallicities, and ages of the dominant stellar populations. In Section 3.4 we review the absorption features revealed in the quasar sightline and place limits on the possible presence of key ions. Finally, in Section 3.5, we briefly discuss the

Table 3.1: Summary of imaging observations of the galaxy pair in the field of PG 1522+101

Instrument	Filter	Exposure Time (s)	FWHM ($''$)	Date
VIMOS	B	470	0.8	2004 May
VIMOS	V	350	0.7	2004 May
VIMOS	R	90	0.7	2004 May
VIMOS	I	180	0.6	2004 May
UKIDSS	J	40	1.1	2007 Mar
UKIDSS	H	40	0.9	2007 Mar
UKIDSS	K	40	0.8	2007 Mar
LDSS3	r	1500	0.7	2009 Apr

implications of our study. Throughout the chapter, we adopt a Λ cosmology with $\Omega_{\rm m} = 0.3$, $\Omega_\Lambda = 0.7$, and $H_0 = 70\ {\rm km\,s^{-1}\,Mpc^{-1}}$. We perform K corrections with the IDL kcorrect library described in Blanton & Roweis (2007). All magnitudes reported here are in the AB system.

3.2 Data

PG 1522+101 is a UV bright quasar at high redshift ($z_{\rm em} = 1.328$), and consequently it represents a prime target for absorption studies of the IGM. A wealth of imaging and spectroscopic data in the PG 1522+101 field are available including: (1) optical and near-infrared imaging of the field, (2) optical spectroscopy of the galaxy pair, and (3) optical and UV spectroscopy of the quasar. In this section, we describe each of these three datasets and the related data-reduction and processing steps. The imaging data are summarized in Table 3.1, and the spectroscopic data are summarized in Table 3.2.

3.2.1 Galaxy imaging

Optical r-band images of the field around PG 1522+101 were obtained using the Low Dispersion Spectrograph 3 (LDSS3) on the Magellan Clay Telescope in April of 2009 as pre-imaging for our absorption blind redshift survey in the fields of UV bright quasars (see

Table 3.2: Summary of spectroscopic observations of the galaxy pair in the field of PG 1522+101

Target	Instrument / Disperser	Exposure Time (ks)	FWHM (Å)	Date
PG 1522+101	HIRESb	1.6	0.06	2010 Mar
PG 1522+101	COS / G130M	16	0.07	2010 Sep
PG 1522+101	COS / G160M	23	0.07	2010 Sep
G1	IMACS / 200l	14	9	2009 May
G1	IMACS / 200l	11	9	2010 May
G2	IMACS / 200l	11	9	2010 May

Chen & Mulchaey, 2009, and the previous Chapter). The observations consist of a sequence of five exposures of 300 seconds duration each with a full-width at half maximum (FWHM) seeing of $0.7''$. The LDSS3 image of the field was reduced using standard IRAF routines and is displayed in the right panel of Figure 3.1. The depth of the LDSS3 image reveals the presence of faint tidal features around the galaxy pair.

In addition to our LDSS3 images, multi-band optical and near-infrared images of the field are available in the public European Southern Observatory (ESO) Archive and in the United Kingdom Infrared Deep Sky Survey (UKIDSS; Hewett et al., 2006; Casali et al., 2007; Lawrence et al., 2007; Hambly et al., 2008; Hodgkin et al., 2009). The ESO imaging of the field (PI: Christopher Mullis, PID: 71.A-3030) was acquired serendipitously with the Visible MultiObject Spectrograph (VIMOS; Le Fèvre et al., 2003) in May of 2004 as part of an unrelated program. The VIMOS imaging of the pair includes a single exposure in each of the B, V, R, and I filters for 470, 350, 90, and 180 seconds respectively, under seeing conditions ranging from FWHM $= 0.8'' - 0.6''$. We reduced the VIMOS imaging with a custom set of software that bias subtracted and flat-fielded the data and in the case of the I-band image, removed the fringe pattern. We determined the zero-points of the VIMOS imaging data using field stars observed by the Sloan Digital Sky Survey (SDSS; York et al., 2000) and the SDSS-to-Johnson filter conversion formulae derived by Robert Lupton in 2005 and given in the SDSS Data Release 9 (Ahn et al., 2012) documentation. The UKIDSS imaging of the

Figure 3.1: Images of an interacting galaxy pair close to the sightline of PG 1522+101.

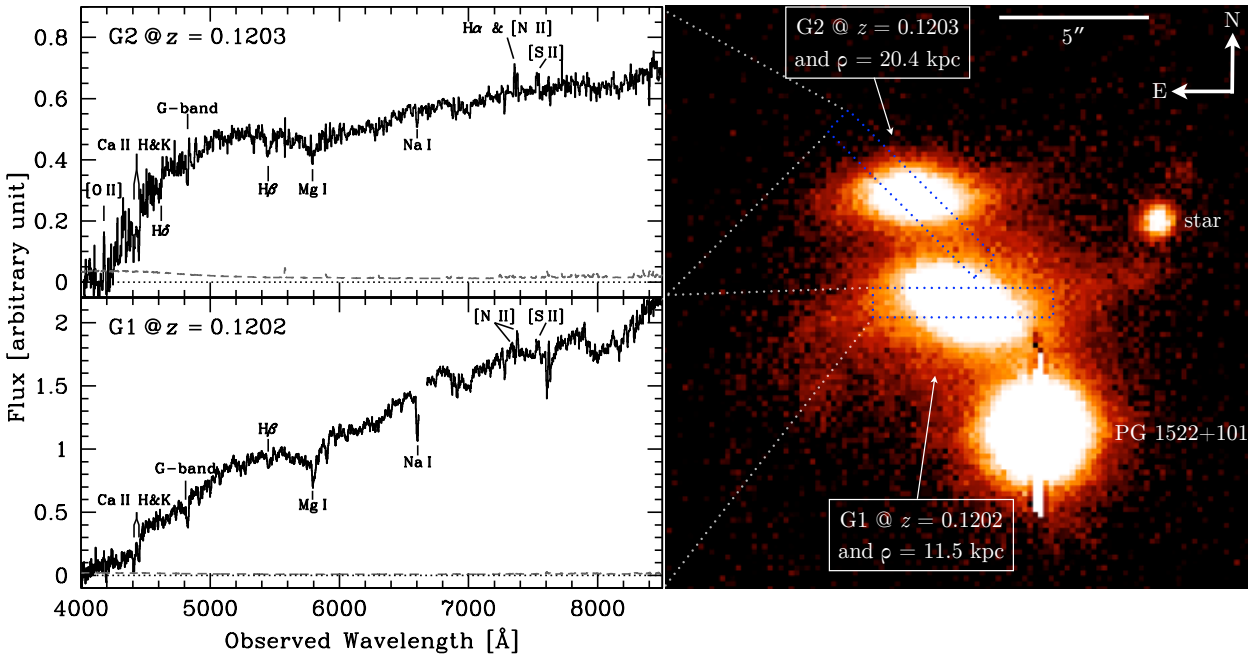

Left: IMACS spectra of the galaxy pair with the brighter member, G1, in the *bottom* panel and the fainter member, G2, in the *top* panel. The spectra are shown in black histogram, and the 1-σ error arrays are shown in gray dashed line. The zero-flux level is shown in black dotted line. Key spectral features in the galaxy spectra are labelled. Note that the flux calibrations of G1 and G2 are relative, so the continuum slopes of the two galaxies should not be compared. *Right*: LDSS3 r-band image of the galaxy pair and the quasar PG 1522+101, scaled and stretched to reveal the presence of faint tidal features. The faint tidal features are seen most prominently in the vicinity of G1. Objects in the field are labelled in white and the spatial scale and orientation of the image are shown in the top right corner. The slit positions and orientations used to observe G1 and G2 spectroscopically are shown in blue dotted line and white dotted lines lead the the eye from the slits to the corresponding spectra shown on the left. The star labelled in the image has been spectroscopically confirmed as part of our redshift survey in the quasar field.

Table 3.3: Summary of galaxy pair photometric properties

	θ	ρ	α[a]	i[b]	Apparent, Isophotal Magnitudes							Absolute Magnitudes[c]			
ID	($''$)	(kpc)	(deg)	(deg)	B_{AB}	V_{AB}	R_{AB}	I_{AB}	J_{AB}	H_{AB}	K_{AB}	M_B	M_R	M_K	log $M_*/M_\odot$[c]
G1	5.1	11.5	32	56	19.58 ± 0.03	18.32 ± 0.04	17.75 ± 0.07	17.18 ± 0.06	16.74 ± 0.06	16.38 ± 0.06	16.56 ± 0.06	-19.81	-21.12	-21.93	10.6
G2	9.4	20.4	56	58	20.40 ± 0.03	19.39 ± 0.04	18.91 ± 0.07	18.49 ± 0.06	18.38 ± 0.12	17.92 ± 0.12	17.98 ± 0.11	-18.82	-19.93	-20.50	10.0

Notes

[a] The azimuthal angle of the major axis of the galaxy from the line connecting the galaxy to the quasar sightline, measured North through East.

[b] Inclination angle of the galaxy disk measured from the major-to-minor axis ratio assuming an intrinsic, edge-on major-to-minor axis ratio of 0.2.

[c] Absolute, rest-frame magnitudes and stellar mass determined using the IDL kcorrect library v4_2 (Blanton & Roweis, 2007) which uses templates created with the Bruzual & Charlot (2003) stellar population synthesis code and emission-line models from Kewley et al. (2001).

field includes 40 second exposures in the J, H, and K filters taken under seeing conditions of FWHM = $1.1''$, $0.9''$, and $0.8''$ respectively. We retrieved the UKIDSS images of the field from the public UKIDSS Data Release 8 website and combined them into a single frame covering the full VIMOS field of view in each filter using the SWARP tool (Bertin et al., 2002). We converted the UKIDSS photometric zeropoints to the AB system using the conversions in Hodgkin et al. (2009).

In order to extract galaxy photometry from the VIMOS and UKIDSS data, we registered the images to a common origin and pixel scale using standard IRAF routines. Next, we formed a detection image by summing the background subtracted VIMOS V, R, and I-band images to enable detection of the low surface-brightness extent of the galaxies. We then defined the isophotal apertures (41 and 24 square arc seconds in area for G1 and G2) of the two galaxies in the summed detection image and calculated the total flux in these apertures in each bandpass using SExtractor (Bertin & Arnouts, 1996) in double-image mode. Finally, we corrected the galaxy photometry for foreground Milky Way extinction following Schlegel et al. (1998). The observed magnitudes of the two galaxies and other photometric properties are shown in Table 3.3.

3.2.2 Galaxy spectroscopy

Galaxies G1 and G2 were observed spectroscopically as part of our blind redshift survey in the fields of UV bright quasars with the short camera of IMACS in multi-object mode with the 200l grating and $1''$ slitlets. In this configuration, IMACS delivers spectral coverage

Table 3.4: Summary of galaxy pair spectroscopic properties

		absorption lines, W_r (Å)					emission lines, W_r (Å)				$\mathrm{SFR_{H\alpha}}$ [c]
ID	z	Ca II λ3934	G-band	Fe I λ4384	Mg I λ5185	Na I λ5897	[O I]λ6302	Hα [a]	[N II] λ6585	$12+\log$ O/H [b]	($M_\odot\,\mathrm{yr}^{-1}$)
G1	0.1202	10.0 ± 0.7	5.3 ± 0.2	1.7 ± 0.3	5.1 ± 0.2	3 ± 1	<0.1	-1.9 ± 0.3	-1.1 ± 0.2	≈ 9.0	≈ 0.08
G2	0.1203	6.9 ± 1.3	4.3 ± 0.4	1.3 ± 0.3	2.4 ± 0.3	1.7 ± 0.2	<0.2	-4.0 ± 0.3	-1.4 ± 0.2	≈ 8.7	≈ 0.06

Notes

[a] Hα emission-line equivalent width corrected for underlying stellar absorption based on stellar population synthesis models.

[b] Gas-phase Oxygen abundance estimate from the "N2" index, N2 = log ([N II] λ6585/Hα), using the relationship from Pettini & Pagel (2004). For reference, the estimated Oxygen abundance of the Sun is $12+\log$ O/H = 8.7 (Allende Prieto et al., 2001).

[c] The star-formation rate measurements for G1 and G2 is derived from Hα. The Hα line luminosity is estimated from the absolute, rest-frame R-band magnitude and the Hα equivalent width observed in our IMACS spectra. The Hα line luminosity is then converted to a star-formation rate using the relation from Kennicutt & Evans (2012).

from ≈ 4000 to ≈ 9000 Å with spectral resolution of FWHM ≈ 9 Å. G1 was observed in May of 2009 for a total of 14 ks and again in May of 2010 for a total of 11 ks. G2 was observed for a total of 11 ks in May of 2010. The IMACS data were reduced using the Carnegie Observatories System for MultiObject Spectroscopy (COSMOS) version 2.16 as described in the previous Chapter. The spectra were flux calibrated in a relative sense using a bright star on the multi-object mask, but no absolute flux standard is available. Since G1 and G2 were observed on different masks and were flux calibrated using different stars, the measured spectral slope of the galaxies cannot be compared. The galaxy redshifts are determined by fitting SDSS galaxy eigenspectra (e.g. Yip et al., 2004) and are corrected for the heliocentric motion of the Earth using the IRAF rvcorrect routine. The final redshifts for G1 and G2 are $z = 0.1202$ and $z = 0.1203$ respectively. Based on a comparison of galaxy redshifts in the PG 1522+101 field measured by both our survey and the SDSS[1], we estimate that the 1-σ uncertainty in the redshifts corresponds to ≈ 60 km s^{-1}. The reduced spectra of galaxies G1 and G2 are shown in the bottom left and top left panels of Figure 3.1 respectively, and the spectroscopic properties of the two galaxies are shown in Table 3.4.

3.2.3 COS and HIRES quasar spectroscopy

High quality UV spectra of PG 1522+101 were acquired with the Cosmic Origins Spectrograph (COS; Green et al., 2012) aboard the *Hubble Space Telescope* (*HST*) as part of

1. We note that G1 and G2 were not observed spectroscopically by the SDSS.

a blind survey for IGM absorption (PI: Todd Tripp, PID: 11741). The *HST* observations include six exposures totaling 16 ks with the G130M grating (covering the spectral range $1150 - 1450$ Å with a spectral resolution of FWHM ≈ 16 km s^{-1}) and eight exposures totaling 23 ks with the G160M grating ($1400 - 1800$ Å , FWHM ≈ 16 km s^{-1}). We combined the 1D, calibrated COS spectra using a custom software suite first described in Meiring et al. (2011). COS is a photon-counting instrument with very low dark backgrounds and minimal scattered light (see Green et al., 2012). This has two implications: (1) it is straightforward to estimate flux uncertainties based on photon counting statistics, and (2) in pixels with low flux levels (e.g., pixels in the cores of deep absorption lines), total counts in an exposure can be very low resulting in asymmetric (Poissonian) flux uncertainties. We evaluated these uncertainties by coadding exposures and accumulating gross and background counts in each pixel, which were used to determine uncertainties based on Poisson statistics (e.g. Gehrels, 1986). To correct for inaccuracies in the COS wavelength calibration, we aligned the exposures by cross correlating well-detected interstellar or extragalactic absorption lines, and likewise the G130M and G160M segments were aligned by cross correlating lines of comparable strength. COS spectra also exhibit fixed-pattern noise, due to shadows from the photocathode grid wires. We corrected the data for these fixed-pattern features using flatfields derived from high-S/N white dwarf observations (D. Massa, private communication) filtered to remove spurious high-frequency noise. Fixed pattern noise due to the hexagonal pattern in the micro-channel plate cannot be fully removed, but the significance of this fixed pattern noise is reduced by the combination of multiple exposures acquired with different central-wavelength settings.

In addition to the UV COS spectrum, high-resolution optical spectra of the quasar were acquired with the High Resolution Echelle Spectrometer with settings optimized for short-wavelength observations (HIRESb; Vogt et al., 1994) on the Keck I telescope (PI: Jason Prochaska, PID: U066Hb) in March of 2010. The HIRESb observations include two exposures totaling 1.6 ks with the $0.86''$ slit (covering the spectral range $3000 - 6000$ Å with spectral

resolution of FWHM $\approx 6\,\mathrm{km\,s^{-1}}$). We reduced the HIRES spectrum with standard techniques using the HIRedux package bundled in the XIDL library.

3.3 Galaxy pair properties

Galaxies G1 and G2 are separated from each other by 8.95 kpc in projected distance and 30 ± 60 km s^{-1} in line-of-sight velocity. The galaxies exhibit low-surface brightness features (see the right panel of Figure 3.1) characteristic of tidal disruption (though we cannot rule out the possibility of faint spiral arms). These faint features combined with the small projected distance and radial velocity difference indicate that G1 and G2 are strongly interacting.

G1 has a rest-frame R-band absolute magnitude $M_R = -21.12$, rest-frame optical color $M_B - M_R = 1.3$, and a best-fit stellar mass[2] of $\log M_*/M_\odot \approx 10.6$, while G2 has $M_R = -19.93$, $M_B - M_R = 1.1$, and $\log M_*/M_\odot \approx 10.0$. Adopting the stellar-to-halo mass relation of Moster et al. (2010) from an abundance matching approach, we estimate that the halo mass of the interacting galaxy pair is $\log M_{\mathrm{halo}}/M_\odot \approx 12.1$ with a corresponding virial velocity $v_{\mathrm{vir}} \approx 200$ km s^{-1}.

The colors of both galaxies are consistent with those of an evolved stellar population with some trace of ongoing star-formation. We estimate the star-formation rates of G1 and G2 using a combination of our imaging and spectroscopic data. First, we measure the rest-frame, Hα emission equivalent widths observed in the galaxy spectra. Our IMACS spectrum of G1 shows only weak Hα emission despite the presence of both [N II] and [S II] emission due to underlying stellar absorption. We correct for the stellar absorption based on the best-fit stellar-population synthesis (SPS) model described below after convolving and rebinning the SPS model spectrum to match the IMACS resolution and wavelength grid. The stellar absorption corrected Hα emission equivalent width of G1 is $W_r(\mathrm{H}\alpha) = -1.9 \pm 0.3$ Å. Similarly, we measure a stellar absorption corrected equivalent width of $W_r(\mathrm{H}\alpha) = -4.0 \pm 0.3$ Å for

2. Best-fit stellar masses are an ancillary product of the kcorrect code.

G2. Next, we estimate the Hα line luminosities of G1 and G2 using these equivalent widths and the R-band absolute magnitudes of the galaxies. Finally, we convert the Hα luminosities to star-formation rates using the formula from Kennicutt & Evans (2012). The estimated star-formation rates of G1 and G2 are $\mathrm{SFR}_{\mathrm{H}\alpha} \approx 0.08\,M_{\odot}\,\mathrm{yr}^{-1}$ and $\mathrm{SFR}_{\mathrm{H}\alpha} \approx 0.06\,M_{\odot}\,\mathrm{yr}^{-1}$ respectively.

In addition, we measure the [N II] λ6585 emission equivalent widths of G1 and G2 in order to estimate the gas-phase Oxygen abundance of the two galaxies using the "N2" index from Pettini & Pagel (2004). Galaxies G1 and G2 exhibit [N II] equivalent widths of $W_r(\mathrm{N\,II}\,\lambda6585) = -1.1 \pm 0.2$ and -1.4 ± 0.2 respectively. The corresponding Oxygen abundance estimates for G1 and G2 are $12 + \log(\mathrm{O/H}) \approx 9.0$ and $12 + \log(\mathrm{O/H}) \approx 8.7$. We note that our IMACS spectra are dominated by the central regions of these two galaxies, and in the presence of metallicity gradients, our gas-phase Oxygen abundances are upper limits. For reference, the estimated Oxygen abundance of the Sun is $12 + \log\,\mathrm{O/H} = 8.7$ (Allende Prieto et al., 2001).

The relatively high [N II] λ6585 to Hα line ratios observed in G1 and G2 raise the possibility that the galaxies host low-ionization nuclear emission-line regions (LINER) powered by active galactic nuclei (AGN). To address this possibility, we measure 3-σ upper limits on the equivalent width of [O I] λ6302 of $W_{\mathrm{r}}([\mathrm{O\,I}]\,\lambda6302) < 0.1$ Å for G1 and $W_{\mathrm{r}}([\mathrm{O\,I}]\,\lambda6302) < 0.2$ Å for G2. These non-detections of [O I] emission place limits on the [O I] to Hα emission-line ratios of $\log\,[\mathrm{O\,I}]/\mathrm{H}\alpha < -1.3$. This limit indicates that neither galaxy hosts a LINER AGN based on the models of Kewley et al. (2006). In addition, neither galaxy falls in the AGN region of the $W_r(\mathrm{H}\alpha)$ versus $\log\,\mathrm{N\,II}/\mathrm{H}\alpha$ classification system developed by Cid Fernandes et al. (2011) for weak emission-line galaxies. Finally, the images of G1 and G2 show no evidence for nuclear point-sources. We therefore conclude that neither G1 nor G2 hosts an AGN.

We also estimate the ages of the dominant stellar populations of G1 and G2 using a

Table 3.5: Summary of absorption limits associated with the interacting galaxy pair at $z = 0.1202$.

		H I		Si II	C II	Si III	Mg II	Si IV	C IV	O VI
	Δv		b							
z	(km s^{-1})	log N/cm^{-2}	(km s^{-1})	log N/cm^{-2}						
0.12022	+7	$< 13.5 \pm 0.06$[a]	28 ± 4	< 12.4[b]	< 13.3[b]	< 12.2[b]	< 12.2[b]	< 12.7[b]	< 13.2[b]	< 13.7[a]
0.12072	+140	$< 13.0 \pm 0.07$[a]	28 ± 7							

Notes

[a] Features are contaminated by intervening systems. Limits and measurements are based on a Voigt profile analysis described in Section 3.4.

[b] Limits are 3-σ and calculated over a 300 km s^{-1} window.

maximum-likelihood analysis that compares Stellar Population Synthesis (SPS) models with the observed properties of the two galaxies. We compute the SPS model spectra using the Bruzual & Charlot (2003) code with updated stellar libraries and evolutionary tracks (Bruzual & Charlot, 2010) and the dust model from Charlot & Fall (2000) which is parameterized by the optical depth τ_V applied to stars younger than 10 Myr and a fraction μ of τ_V in the diffuse interstellar medium (and hence applied to both young and old stars). The model spectra span a range in age from $\log\, t/\mathrm{Gyr} = -0.2$ to 1.1 in steps of $\Delta \log\, t/\mathrm{Gyr} = 0.03$; a range in the e-folding time from $\tau = 0.1$ to 0.5 Gyr in steps of $\Delta\tau = 0.1$ Gyr; a range in metallicity covering $Z = 0.005, 0.02, 0.2, 0.4, 1.0$, and $2.5\, Z_\odot$; and a range in dust properties with τ_V ranging from $\tau_V = 0$ to 2 in steps of $\Delta\tau_V = 0.2$ and $\mu = 0$ to 1 in steps of $\Delta\mu = 0.2$.

We compute the likelihood of each SPS model realization by comparing the apparent magnitudes of G1 and G2 and the rest-frame absorption-line equivalent widths of Ca II λ3934, the G-band, Fe I λ4384, Mg I λ5897, and Na I λ5897 of the two galaxies measured in our IMACS spectra (see Table 3.4). We include the absorption-line equivalent width measurements in our likelihood analysis in order to help break the age-metallicity degeneracy.

The maximum-likelihood age of the dominant stellar population of G1 is $\log\, t/\mathrm{Gyr} = 0.6 \pm 0.1$ and that of G2 is $\log\, t/\mathrm{Gyr} = 0.4^{+0.2}_{-0.1}$ after marginalizing over all other parameters. The stellar mass estimates of the two galaxies from our SPS modeling are consistent with those from kcorrect within uncertainties. The mean values of the other parameters are $Z = 1.1, 0.2\, Z_\odot$; $\tau = 0.3, 0.3$ Gyr; $\tau_v = 0.5, 0.8$; and $\mu = 0.3, 0.4$ for G1, G2. The mean

star-formation rates averaged over the last 10 Myr are SFR $= 0.01\,M_{\odot}\,\mathrm{yr}^{-1}$ for both G1 and G2. The specific star-formation rate of G2 is therefore approximately four times that of G1 since G1 is four times more massive. This is consistent with the bluer colors of G2 relative to G1.

Our spectroscopic survey of the field identified two additional galaxies of $0.2\,L_{*}$ at projected distances of 377 and 689 kpc from the quasar sightline with redshifts of $z = 0.1201$ and 0.1205. Therefore, G1 and G2 are likely members a small galaxy group.

3.4 The transparent sightline

The sightline of PG 1522+101 probes the environment of the interacting galaxy pair at $\rho = 11.5\,\mathrm{kpc}$ and an angle of 32 degrees from the major axis of G1, and at $\rho = 20.4\,\mathrm{kpc}$ and an angle of 56 degrees from the major axis of G2. Despite the small impact parameter, the quasar spectrum exhibits surprisingly little absorption associated with the galaxy pair with a total H I column density no greater than $\log N(\mathrm{H\,I})/\mathrm{cm}^{-2} = 13.65 \pm 0.05$ and no detected heavy element absorption within the virial velocity, $\Delta v = \pm 200\ \mathrm{km\,s}^{-1}$.

We measure the absorber properties based on a Voigt profile analysis using the VPFIT package (Carswell et al., 1987). In cases of component blending, we employ the minimum number of absorption components required to achieve a reasonable χ^2 value. The COS line-spread function (LSF) exhibits broad wings which contain up to 40% of the flux (Ghavamian et al., 2009). In order to properly account for the absorption that falls in the LSF wings, we convolve the Voigt profile models with the empirical, wavelength-dependent COS LSF[3]. The continuum normalized COS spectrum and best-fit models are displayed in Figure 3.2.

The Lyα absorption associated with the galaxy pair (see the top left panel of Figure 3.2) is contaminated by Lyβ at $z = 0.3278$, but the strength of the contaminating Lyβ absorption is constrained by the Lyα and Lyγ features observed in the COS spectrum. In order to

3. http://www.stsci.edu/hst/cos/performance/spectral_resolution/

Figure 3.2: Absorption profiles of halo gas around the interacting galaxy pair.

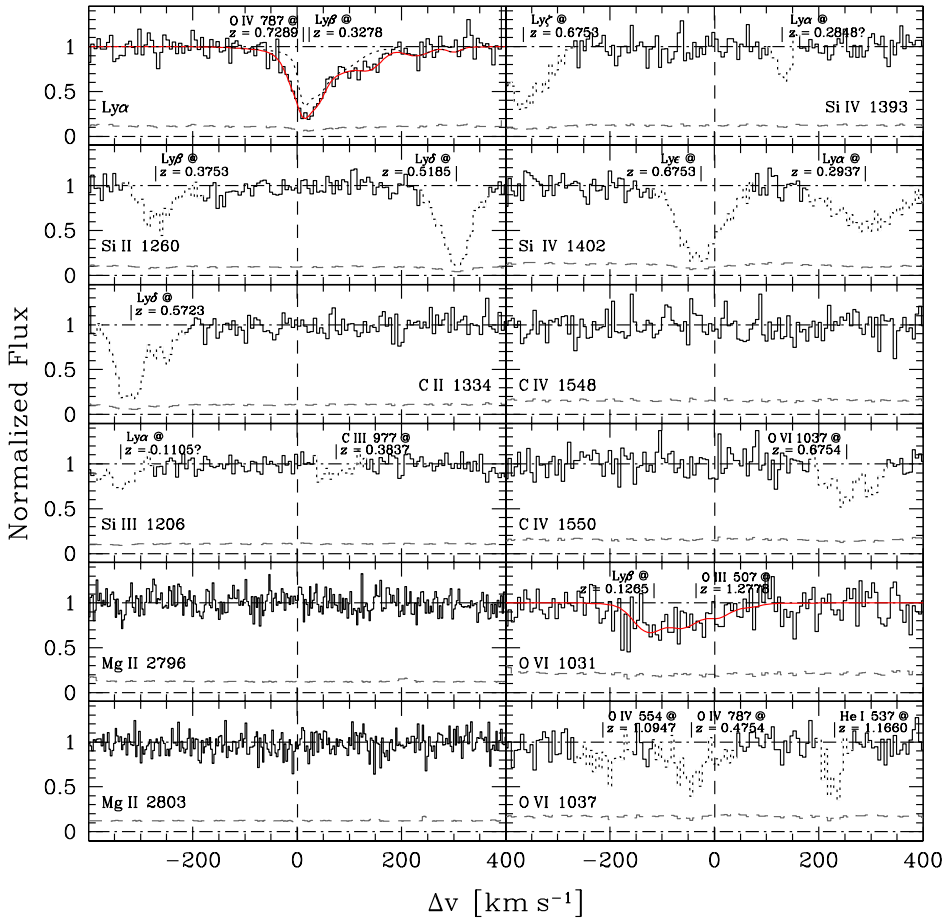

In each panel, the continuum normalized spectrum is shown in solid black, and the 1-σ errors are shown in gray dashed line. Contaminating features are dotted out and labelled except in the case of Lyα and O VI λ1031 which are discussed in detail both here and in the main text. The Lyα absorption associated with the galaxy pair is contaminated by both Lyβ at $z = 0.3278$ and O IV at $z = 0.7289$. We were able to accurately determine the strength of the contaminating Lyβ by simultaneously fitting a Voigt profile to the associated Lyα and Lyγ features at $z = 0.3278$. The strength of O IV at $z = 0.7289$ is, however, more difficult to estimate given the multiphase nature of the gas (see Lehner et al., 2013). We present in the top-left panel the observed absorption in black histogram together with the model for the contaminating Lyβ absorption in black dotted line. The data exhibit excess absorption which could be due to Lyα associated with the galaxy pair or O IV at $z = 0.7289$. Given the uncertain strength of O IV at $z = 0.7289$, we place a limit on the possible presence of H I associated with the galaxy pair by attributing all of the observed absorption to Lyα at $z = 0.12$. After removal of the Lyβ at $z = 0.3278$ (see the top panel of Figure 3.3), the data are best fit by two Voigt components at $\Delta v = +7$ and $+140$ km s^{-1} with column densities of $\log N(\mathrm{H\,I})/\mathrm{cm}^{-2} = 13.5 \pm 0.06, 13.0 \pm 0.07$ and line widths of $b = 28 \pm 4, 28 \pm 7$ km s^{-1} respectively. The best-fit model including these two components is shown in solid red line.

Figure 3.3: Possible H I and O VI absorption profiles associated with the galaxy pair after removal of contaminating features where possible.

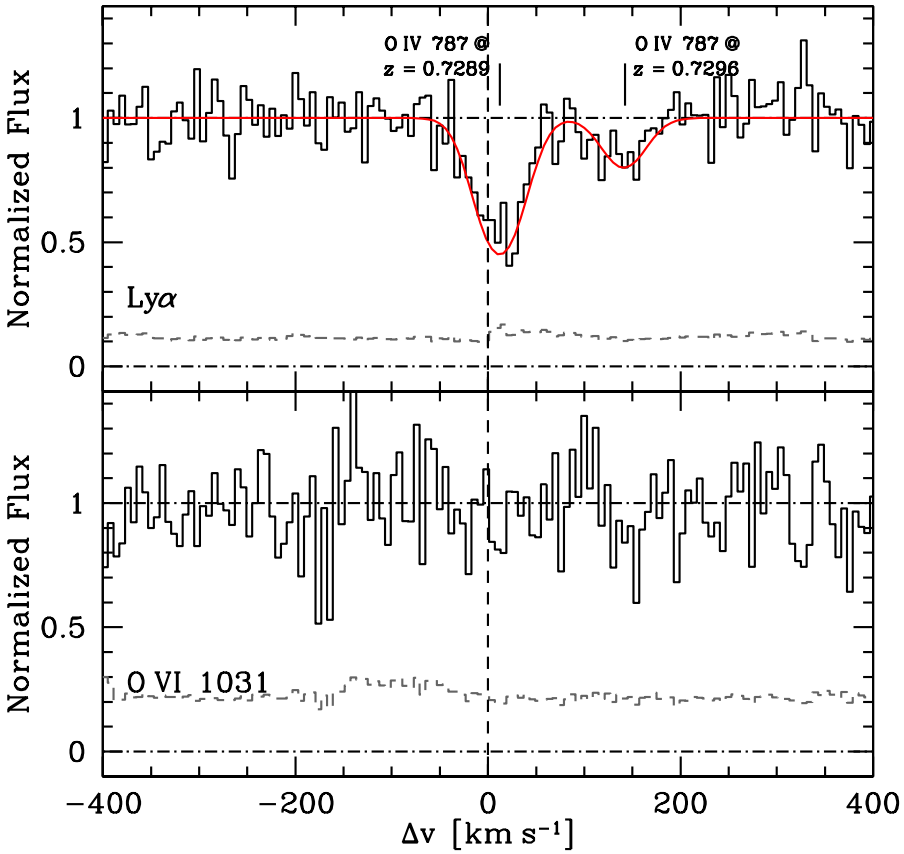

Same as Figure 3.2 but with contaminating features that are constrained by other transitions in the COS spectrum removed (see Section 4 for details). The absorption feature shown in the top panel could be due to Lyα associated with the galaxy pair at $z = 0.12$ and/or O IV λ787 from the multi-phase gas associated with an LLS at $z = 0.7289$. Attributing all of the observed absorption to Lyα at $z = 0.12$ leads to a total H I column density of $\log N(\mathrm{H\,I})/\mathrm{cm}^{-2} = 13.65 \pm 0.05$ (red solid line), which sets an upper limit to the amount of H I that can be associated with the galaxy pair. In the bottom panel, we show that no excess absorption is observed after removing the contaminating features and we place a limit of $\log N(\mathrm{O\,VI})/\mathrm{cm}^{-2} < 13.7$ on the OVI associated with the galaxy pair.

remove the Lyβ contamination, we perform a simultaneous Voigt profile fit to the Lyα and Lyγ transitions, resulting in a model for the corresponding Lyβ. We then divide the data by the modeled Lyβ absorption to remove the contamination due to the $z = 0.3278$ system (see the top panel of Figure 3.3).

After removal of the Lyβ absorption, the data show significant absorption which could be due to Lyα associated with the galaxy pair, O IV λ787 absorption from a Lyman limit system (LLS) at $z = 0.7289$, or a combination of the two. Lehner et al. 2013 report a metallicity and ionization parameter limit of [X/H] < -2.0 and $\log U > -3.2$ based on the H I, C III, and O III column densities detected in the LLS. With metallicity and ionization parameter within this range, we do not expect the O IV associated with the LLS to significantly contaminate the Lyα associated with the galaxy pair. However, O VI is detected in the LLS indicating a multi-phase nature, and the velocity structure seen in the LLS is consistent with the two absorption components seen in the top panel of Figure 3.3. Consequently, a significant portion of the observed absorption could be due to O IV associated with the LLS. We therefore place a limit on the possible presence of H I associated with the galaxy pair by attributing all of the observed absorption to Lyα at $z = 0.12$. The data are best fit by two Voigt components at $\Delta v = +7$ and $+140$ km s^{-1} with column densities of $\log N(\mathrm{H\,I})/\mathrm{cm}^{-2} = 13.5\pm0.06, 13.0\pm0.07$ and line widths of $b = 28 \pm 4, 28 \pm 7$ km s^{-1} respectively. The line-widths correspond to an upper limit on the gas temperature of $T < 5 \times 10^4$ K. We note that the line-width measurements are only valid under the assumption that the observed absorption is largely due to Lyα associated with the galaxy pair.

The O VI λ1031 absorption associated with G1 and G2 (see the second panel from the bottom on the left of Figure 3.2) is contaminated by Lyβ at $z = 0.1265$ and O III λ507 at $z = 1.2776$. In order to remove the contaminating absorption, we perform a Voigt profile analysis of the Lyα absorption at $z = 0.1265$ and O III λ702 absorption at $z = 1.2776$. We use these fits to model the contaminating absorption and divide the data by the model to

remove the contamination. The results are shown in the bottom panel of Figure 3.3). No excess absorption is observed and we place a 3-σ limit of log $N(\mathrm{O\,VI})/\mathrm{cm}^{-2} < 13.7$ on the O VI associated with the galaxy pair.

The other transitions shown in Figure 3.2 are not significantly contaminated. For these transitions, we calculate column density limits by measuring the 3-σ equivalent width limit over a 300 $\mathrm{km\,s}^{-1}$ window (significantly broader than the wings of the COS LSF) centered at $z = 0.1202$ and convert to the corresponding 3-σ limit in column density assuming that the gas is optically thin. We detect no other heavy-element absorption associated with G1 and G2 with column density limits of log $N(\mathrm{Si\,II})/\mathrm{cm}^{-2} < 12.4$, log $N(\mathrm{C\,II})/\mathrm{cm}^{-2} < 13.3$, log $N(\mathrm{Si\,III})/\mathrm{cm}^{-2} < 12.2$, log $N(\mathrm{Mg\,II})/\mathrm{cm}^{-2} < 12.2$, log $N(\mathrm{Si\,IV})/\mathrm{cm}^{-2} < 12.7$, and log $N(\mathrm{C\,IV})/\mathrm{cm}^{-2} < 13.2$. The column density limits of the absorption associated with the galaxy pair are summarized in Table 3.5. We are not able to place a limit on the presence of N V because the $\lambda\lambda 1238, 1242$ doublet is contaminated by a Lyman limit system at $z = 0.5185$.

We performed a series of Cloudy (Version 13; see Ferland et al., 2013) photoionization models in an attempt to constrain the physical conditions of the galaxy halo gas, but the H I, O VI, and other heavy element column density limits are not sufficient to place constraints on the metallicity and ionization state of the gas.

3.5 Discussion and Conclusions

We have identified an interacting pair of galaxies at $z = 0.12$ and $\rho < 20$ kpc from the sightline toward the background quasar PG 1522+101 at $z_{\mathrm{em}} = 1.328$. The galaxy pair is likely be part of a small galaxy group with two additional galaxies with spectroscopic redshifts detected within 1 Mpc and ± 300 $\mathrm{km\,s}^{-1}$ from the pair. The quasar sightline reveals surprisingly little absorption associated with the galaxy pair with a total H I column density no greater than log $N(\mathrm{H\,I})/\mathrm{cm}^{-2} = 13.65 \pm 0.05$ and no detected heavy-element absorption. The dearth of absorption is unusual when compared with results from previous absorption-

line surveys in the vicinities of field galaxies. In the top panel of Figure 3.4, we show the $W_r(\mathrm{Mg\,II}\,\lambda2796) - \rho$ relation from Chen et al. (2010a) along with the limit on the equivalent width of Mg II $\lambda2796$ associated with G1 and G2. All 15 field galaxies in the Chen et al. (2010a) sample at $\rho \lesssim 25$ kpc from the background quasar sightline exhibit a strong associated Mg II absorber, indicating a unity gas covering fraction. In contrast, the Mg II equivalent width limit for G1 and G2 falls more than an order-of-magnitude below the mean expected from the Chen et al. (2010a) sample.

Similarly, we show the H I column density versus ρ relation from Chen et al. (2001) and Werk et al. (2013) in the middle panel of Figure 3.4 along with the H I column density of gas associated with G1 and G2 which falls well below the mean expected from the Chen et al. (2001) and Werk et al. (2013) samples. We estimate that the probability of seeing such little absorption in a sightline at $\rho < 40$ kpc to two non-interacting galaxies with gaseous halos that overlap in projection is less than 0.2%

In addition, we detect no O VI absorption associated with the galaxy pair indicating an absence of the warm-hot halo gas commonly seen around galaxies with detectable star-formation (e.g. Chen et al., 2001; Tumlinson et al., 2011). In the bottom panel of Figure 3.4, we show the O VI column density versus ρ relation from Werk et al. (2013) along with the O VI column density limit of gas associated with G1 and G2. The O VI column density limit falls an order-of-magnitude below the mean expected from galaxies with detectable star-formation in the Werk et al. (2013) sample.

Cool gas is commonly detected in the halos of galaxies out to several hundred kpc in both 21-cm studies at low redshift (e.g. Oosterloo et al., 2007; Grossi et al., 2009) and in more sensitive absorption-line studies at higher redshift (e.g. Chen et al., 2010a; Tumlinson et al., 2011; Thom et al., 2012). At the same time, a reduced H I gas mass is commonly seen in groups of galaxies (e.g. Verdes-Montenegro et al., 2001; Pisano et al., 2011; Catinella et al., 2013). The gaseous halos of the interacting galaxies presented here could have been

tidally stripped, expelled, or heated to $T \gg 10^6$ K by an interaction-triggered feedback mechanism such as a starburst or an active-galactic nucleus (AGN) driven wind. However, there is no observational evidence for a recent burst of star-formation or AGN activity, making more direct stripping or heating by the galaxy interaction a more likely explanation for the dearth of absorption near the galaxy pair. The reservoirs of cool gas in the galaxy halos have been significantly depleted possibly indicating that the galaxies are in the process of interaction-induced quenching. Based on a single sightline alone, however, we cannot rule out the presence of significant cool gas in the galaxy halos since the halos could be characterized by a reduced but non-zero covering fraction. Indeed, our observations cannot rule out the presence of a substantial H I gas disk. For galaxies with stellar masses similar to that of G1, we expect an H I gas disk with mass of $M_{\rm H\,I} \sim 10^{9-10}\,M_\odot$ based on the stellar to H I mass relation from Catinella et al. (2013). Adopting the H I disk mass to cross-section scaling relation from Rosenberg & Schneider (2003), we infer an expected H I disk radius of $R_{\rm H\,I} \sim 7 - 30$ kpc. It is therefore possible that G1 possesses an H I disk within the normal mass range but which is not large enough to intercept the sightline of PG 1522+101.

The transparent sightline at low impact parameter to two interacting galaxies presented here underscores the potential impact of galaxy interactions on the gaseous halos of galaxies. It suggests that galaxy interactions can significantly reduce the reservoir of cool gas in galaxy halos without a strong feedback mechanism. However, the relationship between galaxy environment and halo gas content remains largely unexplored. We are aware of only two other low impact parameter sightlines probing close and possibly interacting galaxy pairs. One consists of two red ($M_B - M_R > 1.0$) galaxies at $z = 0.226$ separated by 17 kpc and probed by a quasar sightline at projected distances of $\rho = 30$ kpc. Chen et al. (2010a) report the detection of an associated Mg II absorption system at $\Delta v = 0$ km s^{-1} with $W_r(\text{Mg II}\,\lambda2796) = 0.54 \pm 0.08$ Å for this galaxy pair. The other galaxy pair consists of two star-forming galaxies separated by 16 kpc at $z = 0.095$ and is probed at $\rho < 30$ kpc by

Figure 3.4: Comparison between the limits placed on absorbing gas associated with the galaxy pair and observations those of more isolated galaxies from the literature.

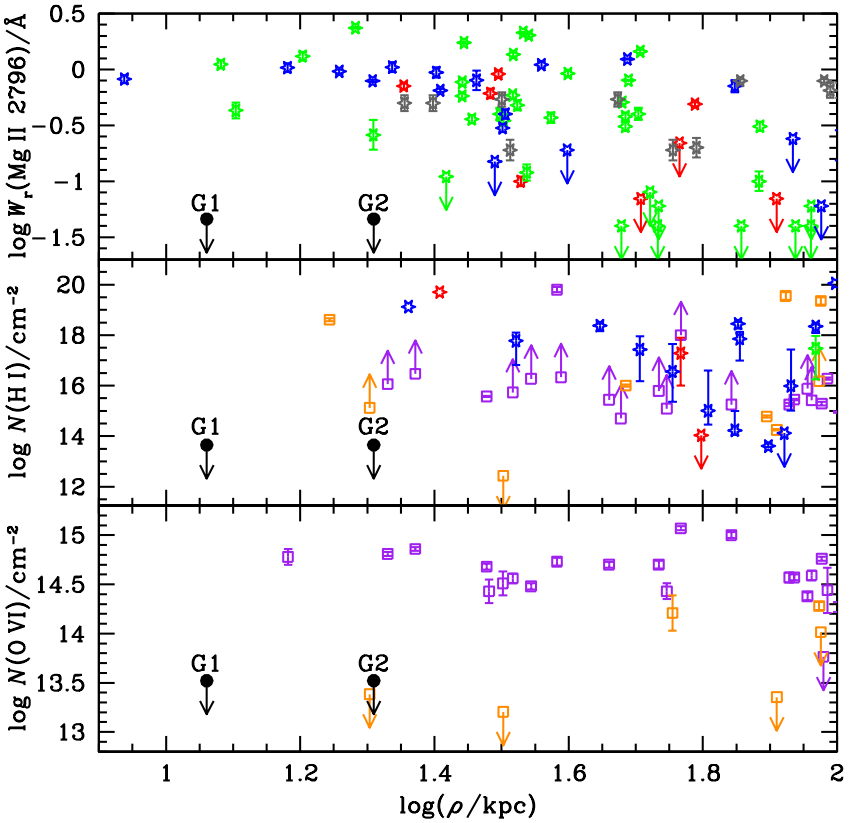

top: Equivalent width of Mg II λ2796 versus ρ reproduced from Chen et al. (2010a) after converting to the cosmology used in this work. The galaxies are shown as six-sided stars and separated into classes by color with S0 galaxies in red, disk galaxies in green, and irregulars in blue (see Chen et al. 2010a for details). In addition, group galaxies are shown in gray. Detections are shown with 1-σ uncertainties and non-detections are indicated by arrows showing 2-σ upper limits. G1 and G2 are shown in black and labelled. The Mg II equivalent width limit for G1 and G2 falls more than an order-of-magnitude below the mean expected from the Chen et al. (2010a) sample. *middle*: H I column density as a function of impact parameter reproduced from Chen et al. (2001) and Werk et al. (2013) after converting to the cosmology used in this work. Galaxies from Chen et al. (2001) are shown with a six-sided star and 1-σ error bars. Upper limits are 2-σ and are indicated by arrows. The sample is divided into S0 (red), early-type disk (green), and late-type disk (blue) galaxies. Galaxies from Werk et al. (2013) are shown as open squares. The Werk et al. (2013) star-forming sample is shown in purple and the passive sample is shown in orange. G1 and G2 are shown as black dots and labelled. The H I column density limit of gas associated with G1 and G2 falls more than two orders-of-magnitude below the mean expected from the Chen et al. (2001) and Werk et al. (2013) samples. *bottom*: O VI column density as a function of impact parameter. Symbols and coloring follow those of the middle panel.

the sightline of the UV-bright quasar SDSS J0820+2334 (see Werk et al., 2012). There is a moderate Lyα absorber with $\log N(\mathrm{H\,I})/\mathrm{cm}^{-2} = 14.0 \pm 0.1$ associated with this galaxy pair ($\Delta v = 0$) with no detected metal-line absorption.

The observed H I absorption is significantly weaker than what is expected for a sightline at low impact parameter to non-interacting galaxies. There is a strong Lyα system with $\log N(\mathrm{H\,I})/\mathrm{cm}^{-2} = 15.3 \pm 0.5$ and associated C IV and O VI absorption at $\Delta v = +300$ $\mathrm{km\,s}^{-1}$, the same velocity as a more luminous, star-forming galaxy at $\rho = 140$ kpc. The presence the more luminous, star-forming galaxy complicates the interpretation of this system. Further exploration of the impact of galaxy environment and interactions on the gaseous content of galaxy halos will likely require a systematic survey of quasar sightlines probing the environments of group galaxies.

CHAPTER 4

ON THE POSSIBLE ENVIRONMENTAL EFFECT IN DISTRIBUTING HEAVY ELEMENTS BEYOND INDIVIDUAL GASEOUS HALOS

The contents of this chapter have been published in the Monthly Notices of the Royal Astronomical Society and are reproduced here in accordance with the copyright agreement and with permission from the Oxford University Press.

Johnson, S. D., Chen, H.-W., & Mulchaey, J. S. 2015, MNRAS, 449, 3263

4.1 Introduction

Galaxies grow by a combination of gas accretion from the intergalactic medium (IGM) and mergers. After heavy element enrichment, it is expected that gas is subsequently ejected back to the IGM through starburst and AGN driven winds (e.g. Murray et al., 2011) or by stripping during galaxy interactions (e.g. Wang, 1993; Gauthier, 2013). The low-density gas of the circum-galactic medium (CGM) is at the nexus of these baryon cycles, and it represents a potentially significant, multiphase reservoir that can fuel star-formation on long time-scales (e.g. Maller & Bullock, 2004). Moreover, the CGM constitutes a sensitive laboratory for studying the physical processes that control the inflow and outflow of baryons from galaxies and for testing sub-grid feedback recipes implemented in simulations of galaxy evolution (e.g. Hummels et al., 2013; Ford et al., 2013; Cen, 2013; Shen et al., 2013b; Liang et al., 2016).

The density of the CGM is nearly always too low to be studied in emission with existing facilities. Nevertheless, a great deal of progress has been made via UV absorption-line spectroscopy of background objects at low projected distances, d, from foreground galaxies. Observations of the H I Lyman series (e.g. Chen et al., 1998; Tripp et al., 1998; Wakker & Savage, 2009; Stocke et al., 2013; Rudie et al., 2013; Tumlinson et al., 2013), the Mg II

doublet (e.g. Bowen et al., 1995; Chen et al., 2010a; Gauthier et al., 2010; Bordoloi et al., 2011), the C IV doublet (e.g. Chen et al., 2001; Borthakur et al., 2013; Liang & Chen, 2014; Bordoloi et al., 2014), and the O VI doublet (e.g. Chen & Mulchaey, 2009; Wakker & Savage, 2009; Prochaska et al., 2011b; Tumlinson et al., 2011; Mathes et al., 2014; Stocke et al., 2014; Turner et al., 2014) have been particularly fruitful.

Cool, metal-enriched gas traced by Mg II, C II, Si II, Si III, and C IV absorption is observed out to impact parameters of 0.7 times the galaxy virial radius ($d \approx 0.7\,R_{\rm h}$) around both late-type and early-type galaxies of $L \lesssim L_*$ alike[1]. At larger projected distances, the incidence of these absorption species decreases sharply to near zero. Liang & Chen (2014) present two possible explanations for this "metal-boundary": (1) an inability of galactic outflows and satellite accretion to efficiently deposit heavy element enriched gas at distances greater than $0.7\,R_{\rm h}$ or (2) an inability of cool-warm gas clouds to form and survive at larger distances.

In contrast, highly-ionized and enriched gas traced by the O VI doublet is found to better reflect the bimodal distribution of galaxies in color-magnitude diagrams. In particular, strong O VI systems are found at high incidence out to $d = 150$ kpc around star-forming galaxies but at lower incidence around more quiescent ones (Chen & Mulchaey, 2009; Tumlinson et al., 2011). Moreover, O VI detections have been reported around sub-L_* galaxies out to $d = 300$ kpc which corresponds to $1 - 3\,R_{\rm h}$ (Prochaska et al., 2011b). However, the sample of galaxies probed at such large distances by absorption spectroscopy is small and the spatial extent of O VI bearing gas around galaxies remains an open question.

To examine the spatial dependence of O VI absorption around galaxies, we have assembled a sample of 95 galaxies that are probed in absorption by quasar sightlines with UV spectra from the Cosmic Origins Spectrograph (COS; Green et al., 2012) on the *Hubble Space Telescope* (HST). These galaxies are drawn from a highly complete ($\gtrsim 80\%$ complete for galaxies of $L > 0.1L_*$ at $z < 0.4$ and $d < 500$ kpc) survey of faint galaxies in the fields of

1. There is evidence that C IV absorption is more extended around starburst galaxies (Borthakur et al., 2013), and more massive luminous red galaxies exhibit reduced Mg II absorption (Gauthier et al., 2010).

four high signal-to-noise COS quasar sightlines. The high completeness of the galaxy survey enables a detailed investigation of possible environmental dependence of extended gas around galaxies. To increase the number of massive galaxies in the study, we include eleven galaxies with stellar masses of $\log M_*/M_\odot > 11$ from the Sloan Digital Sky Survey (SDSS; York et al., 2000) probed in absorption with archival COS quasar spectra. We refer to these galaxy samples collectively as the extended-CGM (eCGM) survey and combine it with 42 galaxies from the COS-Halos program (Werk et al., 2012; Tumlinson et al., 2013) which are primarily at $d < 150$ kpc. Together, the two samples contain 148 galaxies and enable an investigation of the absorption properties of galaxy halos over two decades in projected distance.

The chapter proceeds as follows: In Section 4.2 we describe the galaxy sample. In Section 4.3 we describe the corresponding absorption-line measurements. In Section 4.4 we characterize the observed H I and O VI absorption as a function of projected distance. In Section 4.5 we discuss the implications of our survey results. Throughout the chapter, we adopt a Λ cosmology with $\Omega_{\rm m} = 0.3$, $\Omega_\Lambda = 0.7$, and $H_0 = 70$ km s^{-1} Mpc^{-1}.

4.2 The extended-CGM galaxy sample

To assemble the eCGM galaxy sample, we combined our own absorption-blind survey data targeting galaxies of $r_{\rm AB} < 23$ mag in the fields of HE 0226-4110, PKS 0405-123, LBQS 1435-0134, and PG 1522+101 with spectroscopic galaxies in the Sloan Digital Sky Survey Data Release 10 (SDSS; York et al., 2000; Ahn et al., 2014). The HE 0226-4110, PKS 0405-123, LBQS 1435-0134, and PG 1522+101 fields were selected because of the high completeness levels ($\gtrsim 80\%$) achieved by our surveys for galaxies as faint as $L = 0.1\,L_*$ at $z < 0.4$ and $d < 500$ kpc. At smaller projected distances of $d = 100$ and 200 kpc, the survey completeness increases to 100% and 90% respectively (see Figure 2 of Johnson et al., 2013)[2]. We included

2. Here, we adopt a characteristic luminosity of L_* galaxies of $M_r = -21.5$ based on the luminosity function measurements from Montero-Dorta & Prada (2009) and Loveday et al. (2012).

Table 4.1: Summary of eCGM sample galaxy and absorber properties.

Quasar sightline	Galaxy R.A. (J2000)	Galaxy Dec. (J2000)	$z_{\rm gal}$	$\log(M_*/M_\odot)_{gr}$	class[a]	envi.[b]	survey	d (kpc)	$d/R_{\rm h}$	log N/cm^{-2} H I[c]	log N/cm^{-2} O VI[c]
J0042−1037	00:42:22.27	−10:37:35.2	0.0950	9.5	Late	I	COS-Halos	15	0.1	$14.80 - 18.50$	14.70 ± 0.22
J0226+0015	02:26:12.98	+00:15:29.1	0.2274	10.4	Early	I	COS-Halos	81	0.4	14.36 ± 0.06	< 13.12
HE0226−4110	02:27:46.27	−40:53:15.1	0.1120	10.4	Early	I	IMACS	826	4.1	< 12.88	< 12.90
HE0226−4110	02:27:57.47	−40:57:25.7	0.2952	8.6	Late	I	IMACS	884	9.8	13.36 ± 0.05	< 12.75
HE0226−4110	02:28:01.44	−40:57:55.7	0.3863	9.8	Late	I	IMACS	846	6.5	13.39 ± 0.04	< 12.66
HE0226−4110	02:28:04.31	−40:55:57.4	0.1772	10.5	Early	NI	IMACS	435	2.1	< 12.23	< 13.07
HE0226−4110	02:28:04.52	−40:57:02.3	0.3971	11.1	Late	NI	IMACS	648	1.8	13.99 ± 0.02	13.57 ± 0.09
HE0226−4110	02:28:09.37	−40:57:44.5	0.3341	9.7	Late	NI	IMACS	346	2.6	< 12.36	< 12.75
HE0226−4110	02:28:10.23	−40:55:48.1	0.1248	8.5	Late	I	IMACS	230	2.3	12.88 ± 0.05	< 12.84
HE0226−4110	02:28:10.50	−40:58:57.3	0.3268	9.4	Early	I	IMACS	547	4.7	< 12.35	< 13.05
HE0226−4110	02:28:11.32	−40:56:36.7	0.2804	8.4	Late	I	IMACS	244	2.8	13.73 ± 0.01	-1
HE0226−4110	02:28:11.59	−40:58:53.8	0.2492	8.6	Late	I	IMACS	419	4.5	13.38 ± 0.03	< 13.16
HE0226−4110	02:28:13.89	−40:59:46.2	0.3939	10.2	Late	I	IMACS	812	5.2	< 12.36	< 12.62
HE0226−4110	02:28:14.56	−40:57:22.7	0.2065	8.9	Late	NI	IMACS	37	0.4	15.27 ± 0.06	14.37 ± 0.01
HE0226−4110	02:28:16.29	−40:57:27.2	0.2678	10.3	Early	I	IMACS	75	0.4	< 12.97	< 12.87

Notes

The full table is available in the online version of the paper.

[a] Galaxy classification with "Early" for early-type, absorption-line dominated galaxies and "Late" for late-type, emission-line dominated galaxies

[b] Galaxy environment class as defined in the text with "I" for isolated, "NI" for non-isolated, and "A" for ambiguous cases.

[c] Total column density measured in the COS sightline within $\Delta v = \pm 300$ km s^{-1} of the galaxy systemic redshift. In cases where O VI or H I column densities cannot be measured due to contamination, the value is set to -1.

SDSS galaxies to increase the number of eCGM sample members of log $M_*/M_\odot > 11$. The resulting galaxy sample is summarized in Table 4.1, and its construction is described in this section.

Our galaxy surveys in the HE 0226-4110, PKS 0405-123, LBQS 1435-0134, and PG 1522+101 fields were carried out with the IMACS (Dressler et al., 2011) and LDSS3 spectrographs on the Magellan Telescopes (Shectman & Johns, 2003) targeting galaxies as far as $\Delta\theta = 10'$ from the quasar sightline (corresponding to $d = 1.1$ Mpc at $z = 0.1$). The resulting redshift catalogs and corresponding absorption-line measurements for the HE 0226-4110, PKS 0405-123 fields were published in Chen & Mulchaey (2009) and Johnson et al. (2013). The published survey data include deep B-, V-, and R-band photometry in the HE 0226-4110 field. The LBQS 1435-0134, and PG 1522+101 galaxy redshift catalogs and corresponding IMACS g-, r-, and i-band photometry will be published in Johnson et al. in prep. For the PKS 0405-123 field, we retrieved g-, r-, and i-band images from the Mosaic II CCD Imager on the Blanco 4-m telescope from the NOAO archive (PI: Brian Keeney; PID=2008B-0194). The Mosaic II images consist of 7×75 second exposures in each bandpass. We measured the galaxy photometry using Source Extractor (Bertin & Arnouts, 1996) with settings described in

Johnson et al. (2014).

To increase the number of massive galaxies in the eCGM sample, we cross-matched galaxies of $\log M_*/M_\odot > 11$ in the SDSS DR10 spectroscopic survey with quasar sightlines that have public, high signal-to-noise COS spectra published in Danforth et al. (2014). For the SDSS galaxies, we adopted u-, g-, r-, i-, and z-band cmodel magnitudes[3].

From this parent sample of galaxies, we selected those with projected distances from the quasar sightline $d < 1$ Mpc, within the redshift range $z \approx 0.1 - 0.4$, and with redshift at least $10,000$ km s^{-1} below the quasar redshift. O VI detections have been reported at projected distances of up to 300 kpc from sub-L_* galaxies (Prochaska et al., 2011b) which corresponds to $2 - 3$ times the galaxy halo virial radius. The $d = 1$ Mpc cut was chosen to be sufficiently large to search for absorption at $d/R_{\rm h} = 2 - 3$ around more massive galaxies that have virial radii of $R_{\rm h} \approx 300$ kpc. The redshift lower limit was chosen so that the O VI doublet falls within the COS wavelength range. We note that the redshift range for which the O VI doublet is observable with COS depends on the settings used for the observations. The redshift lower limit therefore varied slightly from sightline to sightline. The redshift upper limit was motivated by the depth of our IMACS redshift surveys which are sensitive to galaxies of $L > 0.1\,L_*$ at $z \lesssim 0.4$. The requirement that the galaxy redshift be at least $10,000$ km s^{-1} below the quasar redshift was imposed to avoid confusion with gas outflowing from the quasar (e.g. Wild et al., 2008). In total, 106 galaxies met these criteria with eleven galaxies from the SDSS and 95 from our survey data.

For each galaxy, we measured the rest-frame, g- and r-band absolute magnitudes using the multi-band optical photometry[4] described above and the kcorrect tool (Blanton & Roweis, 2007). We then estimated mass-to-light ratios using the relation shown in Equation 4.1 which is a fit of the stellar mass to r-band light ratio (in solar units) for low redshift galaxies in the

3. The results presented in this chapter do not change if model rather than cmodel magnitudes are adopted for SDSS galaxies.

4. Corrected for Milky Way extinction from Schlegel et al. (1998).

NASA-Sloan atlas (e.g. Maller et al., 2009). For galaxies redder than $M_g - M_r = 0.15$ in the rest-frame, the fit is a quadratic in $M_g - M_r$. For galaxies bluer than $M_g - M_r = 0.15$, we set the mass-to-light ratio to $\log(M_*/L_r) = -0.6$ which corresponds to an imposed minimum age of ≈ 0.3 Gyr for a simple stellar population with solar metallicity.

$$\log(M_*/L_r) = \begin{cases} -0.6 & M_g - M_r < 0.15 \\ -1.01 + 2.95(M_g - M_r)\ldots & M_g - M_r \geq 0.15 \\ -1.67(M_g - M_r)^2 & \end{cases} \tag{4.1}$$

We then estimated the stellar mass of the eCGM galaxies using Equation 4.2 and the mass-to-light ratios from Equation 4.1.

$$\log(M_*/M_\odot)_{gr} = 1.872 - 0.4M_r + \log(M_*/L_r) \tag{4.2}$$

The rest-frame g- and r- band stellar mass estimates from Equations 4.1 and 4.2 reproduce the NASA-Sloan stellar masses which are calculated with kcorrect, a Chabrier (2003) initial mass function and GALEX $FUV + NUV$ and SDSS $ugriz$ photometry with a systematic error of less than 0.02 dex and 1σ scatter of less than 0.15 dex for galaxies of $M_r = -16$ to -24 as shown in Figure 4.1. The NASA-Sloan atlas contains low-redshift galaxies of $z < 0.055$ so the use of a mass-to-light ratio relation based on these galaxies for the $z = 0.1 - 0.4$ eCGM sample may result in systematic errors due to galaxy evolution over cosmic time. To estimate the magnitude of this systematic error, we compared stellar masses calculated using Equations 4.1 and 4.2 to those based on precise $ugriz$ photometry for $z = 0.1 - 0.4$ galaxies from the PRIMUS galaxy survey (Coil et al., 2011). The systematic error introduced by using a $z < 0.055$ relation for $z = 0.1 - 0.4$ galaxies is less than 0.1 dex over the luminosity range spanned by the eCGM sample.

The eCGM galaxy sample spans a stellar mass range of $\log M_*/M_\odot = 8.4 - 11.5$ with a median of $\log M_*/M_\odot = 10.3$ as shown in Figure 4.2.

Figure 4.1: Residuals between rest-frame g- and r-band based stellar masses and those from the NASA-Sloan atlas.

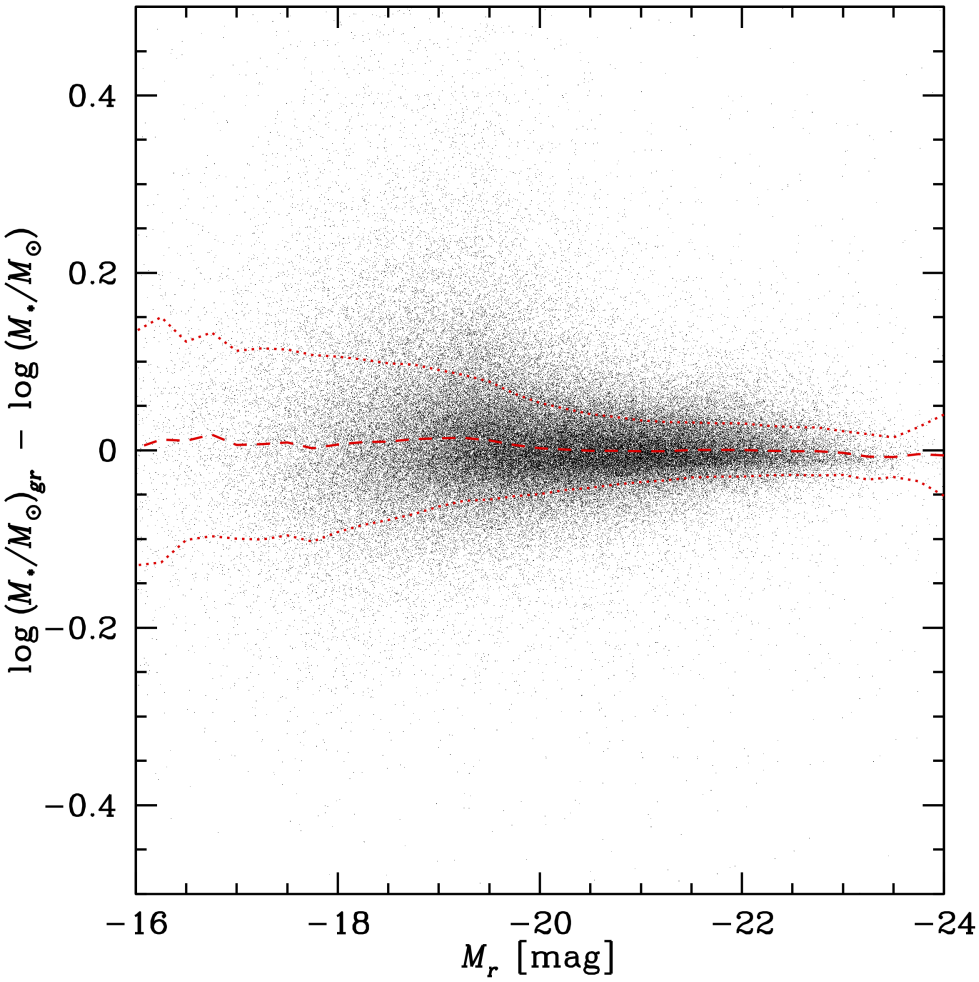

Each point represents a NASA-Sloan galaxy. The dashed red line shows the median residuals in M_r bins with widths of 0.25 mags. The dotted red lines mark $\pm 1\sigma$ from the median in each bin. Within the NASA-Sloan atlas, the systematic error is less than 0.02 dex with 1σ scatter of less than 0.15 dex.

Figure 4.2: Distribution of projected distance, d, between each galaxy and the nearby COS quasar sightline versus stellar mass.

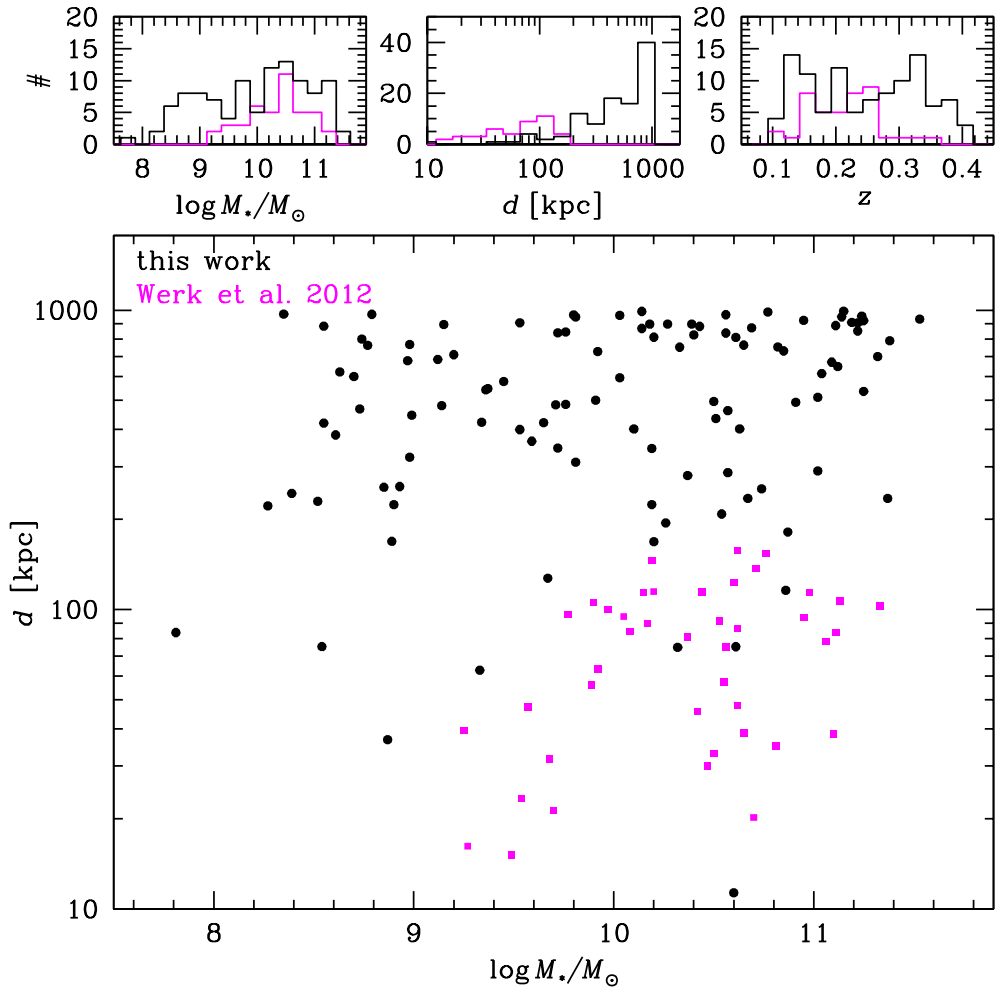

The eCGM galaxy sample is shown in black and the COS-Halos survey is shown in magenta. The *top* three panels show the stellar mass, projected distance, and redshift distributions of the eCGM and COS-Halos galaxy samples.

In order to compare absorption properties of galaxies across a range of stellar mass, we measured projected distance in units of the galaxy dark matter halo virial radius defined by Bryan & Norman (1998) using the stellar-to-halo mass relation from Kravtsov et al. (2014). To ensure consistency across the sample, we re-measured the virial radii of the COS-Halos galaxies using the same methods. We note that our virial radius estimates are as much as 50% smaller than those of Tumlinson et al. (2013) because of the use of a different stellar-to-halo mass relation. The differences between the stellar-to-halo mass relations from Kravtsov et al. (2014) and previous work such as Moster et al. (2010) and Behroozi et al. (2013) are driven by systematic errors in the galaxy photometry in the catalogs used by Moster et al. (2010) and Behroozi et al. (2013) (see Bernardi et al., 2013). The stellar-to-halo mass relation from Kravtsov et al. (2014) is in good agreement with independent constraints from weak lensing (e.g. Reyes et al., 2012).

To search for correlations between CGM properties and the presence of star-formation, we spectroscopically classified galaxies as late-type (emission-line dominated) and early-type (absorption-line dominated) based on a PCA fitting technique described in Chen & Mulchaey (2009).

Unlike some previous surveys, we did not restrict the eCGM galaxy sample to isolated galaxies only. Instead, we classified galaxies as "non-isolated" or "isolated" based on the presence or absence of nearby neighbors. In the HE 0226-4110, PKS 0405-123, LBQS 1435-0134, and PG 1522+101 fields, where our galaxy survey data are highly complete, we classified galaxies as "non-isolated" if they have a spectroscopic neighbor within a projected distance of less than 500 kpc, a radial velocity difference of $|\Delta v| < 300$ km s^{-1}, and with stellar mass of at least one-third of that of the eCGG or COS-Halos survey member. Otherwise, we classified galaxies without such nearby neighbors as "isolated".

Among non-isolated galaxies, the relevant projected distance between the quasar sightline and the galaxy is not clear apriori, and care must be taken in defining the distance to a

non-isolated galaxy to prevent a bias when comparing with isolated ones. For example, a mass or light-weighted projected distance could be large even though the gas detected in absorption may be more closely associated with a less massive "group" member close to the quasar sightline. *To avoid a bias that could make the gas around non-isolated galaxies appear artificially extended, we define the distance to non-isolated galaxies as the minimum value of* $d/R_{\rm h}$ *among "group" members.* This distance definition is a self-consistent choice for comparing the spatial extent of absorbing gas around isolated and non-isolated galaxies.

The available galaxy survey data in the COS-Halos and SDSS fields are not sufficiently complete to confidently classify galaxies by environment based on spectroscopy alone. To classify these galaxies, we performed a literature search to identify members of previously known galaxy groups (e.g. McConnachie et al., 2009) and clusters (e.g. Koester et al., 2007). In addition, we visually inspected the SDSS images in the vicinity of each galaxy to search for likely neighbors based on galaxy brightness, size, color, and SDSS photometric redshift. We classified galaxies with such neighbors as non-isolated and those without as isolated.

4.3 Absorption data

For each galaxy in the eCGM sample, we searched for H I and O VI absorption in the COS quasar spectra within a radial velocity interval of $\Delta v = \pm 300$ km s^{-1} of the galaxy systemic redshift. Tumlinson et al. (2011) found that the radial velocity distribution of O VI absorption-components around galaxies at $d < 150$ kpc is characterized by a standard deviation of $\sigma \approx 100$ km s^{-1}. The $\Delta v = \pm 300$ km s^{-1} search window was chosen to include the vast majority of absorption associated with the eCGM and COS-Halos galaxies[5]. If H I or O VI absorption was detected, we adopted available Voigt profile fitting results from Johnson et al. (2013), Tumlinson et al. (2013), Werk et al. (2013), and Savage et al. (2014).

5. The results presented in this chapter do not change if the velocity window is increased to $\Delta v = \pm 600$ km s^{-1}.

When these measurements are not available, we performed our own Voigt profile fitting using the VPFIT package (Carswell et al., 1987) as described in Johnson et al. (2013). If H I or O VI absorption was not detected, we placed 2σ upper limits on the equivalent width, integrating over a velocity interval of 75 $\mathrm{km\,s^{-1}}$ for H I and 90 $\mathrm{km\,s^{-1}}$ for O VI. We then converted this equivalent width limit to a column density assuming that the gas is optically thin. The 75 $\mathrm{km\,s^{-1}}$ and 90 $\mathrm{km\,s^{-1}}$ integration windows correspond to the median full-width-at-half-maximum of unsaturated H I and O VI absorption components found in the eCGM survey.

For 19 galaxies, Tumlinson et al. (2013) report only lower limits on H I column density due to saturation in all available Lyman series transitions. For these galaxies, we place *upper limits* on the possible H I column density based on the lack of damping wings detected in Lyα. To do so, we measured the Lyα absorption equivalent width and converted this to a H I column density upper limit assuming a single component with doppler width $b = 20$ $\mathrm{km\,s^{-1}}$.

4.4 The extent of H I and O VI absorption around galaxies

With the galaxy and absorption data described in Sections 4.2 and 4.3, we characterize the H I and O VI column densities of the eCGM and COS-Halos galaxy sightlines as a function of projected distance in Figure 4.3. The covering fractions for strong H I and O VI absorption systems of $\log N(\mathrm{H\,I})/\mathrm{cm^{-2}} > 14.0$ and $\log N(\mathrm{O\,VI})/\mathrm{cm^{-2}} > 13.5$ are shown in Figure 4.4. The uncertainties in covering fractions are calculated using standard binomial statistics, and we do not include galaxies with non-detections with upper limits greater than $\log N(\mathrm{H\,I})/\mathrm{cm^{-2}} > 14.0$ or $\log N(\mathrm{O\,VI})/\mathrm{cm^{-2}} > 13.5$ in the calculations. When multiple galaxies are associated with the same absorption system, we show only the galaxy at the smallest d/R_{h}.

Figure 4.3: Column density within $\Delta v = \pm 300$ km s^{-1} versus projected distance measured in units of the galaxy virial radius.

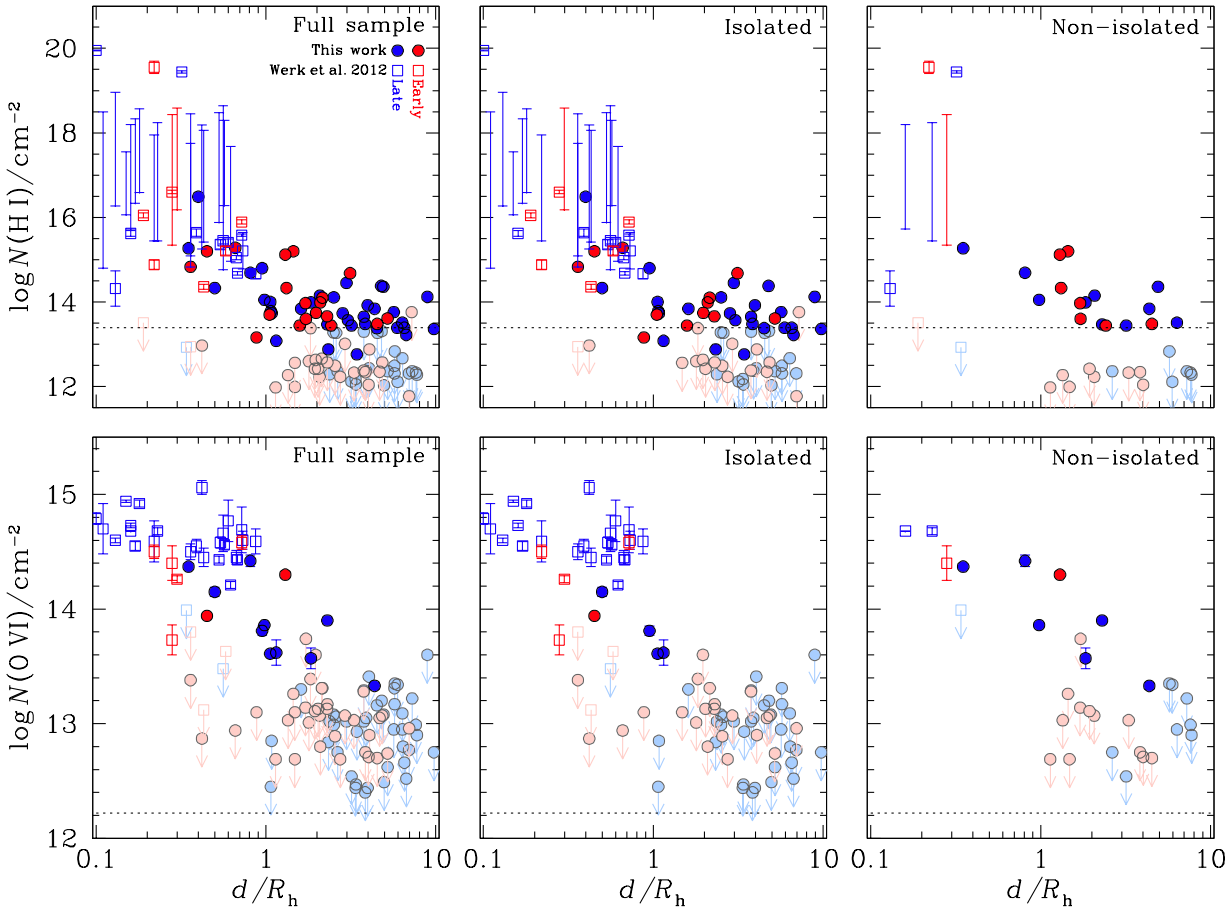

H I absorption is shown in the *top* panels and O VI on the *bottom*. The full galaxy samples are shown in the *left* column and are separated into isolated and non-isolated members in the *middle* and *right* columns respectively. Late- and early-type galaxies are shown in blue and red respectively. eCGM galaxies are displayed as filled circles and COS-Halos galaxies as open squares. Non-detections are shown as 2σ upper limits marked by downward arrows and lighter coloring. The vertical error bars represent 1σ statistical uncertainties reported by VPFIT and do not include uncertainty due to continuum placement. Galaxies with upper limits greater than $\log N/\mathrm{cm}^{-2} = 14.0$ are not considered to have sensitive constraints on the gas column density and are not displayed. The mean absorption expected from random sightlines based on the $\frac{d^2\mathcal{N}}{dNdz}$ measurement from Danforth et al. (2014) is shown as horizontal dotted line.

Figure 4.4: Covering fraction for strong H I and O VI absorption systems as a function of $d/R_{\rm h}$.

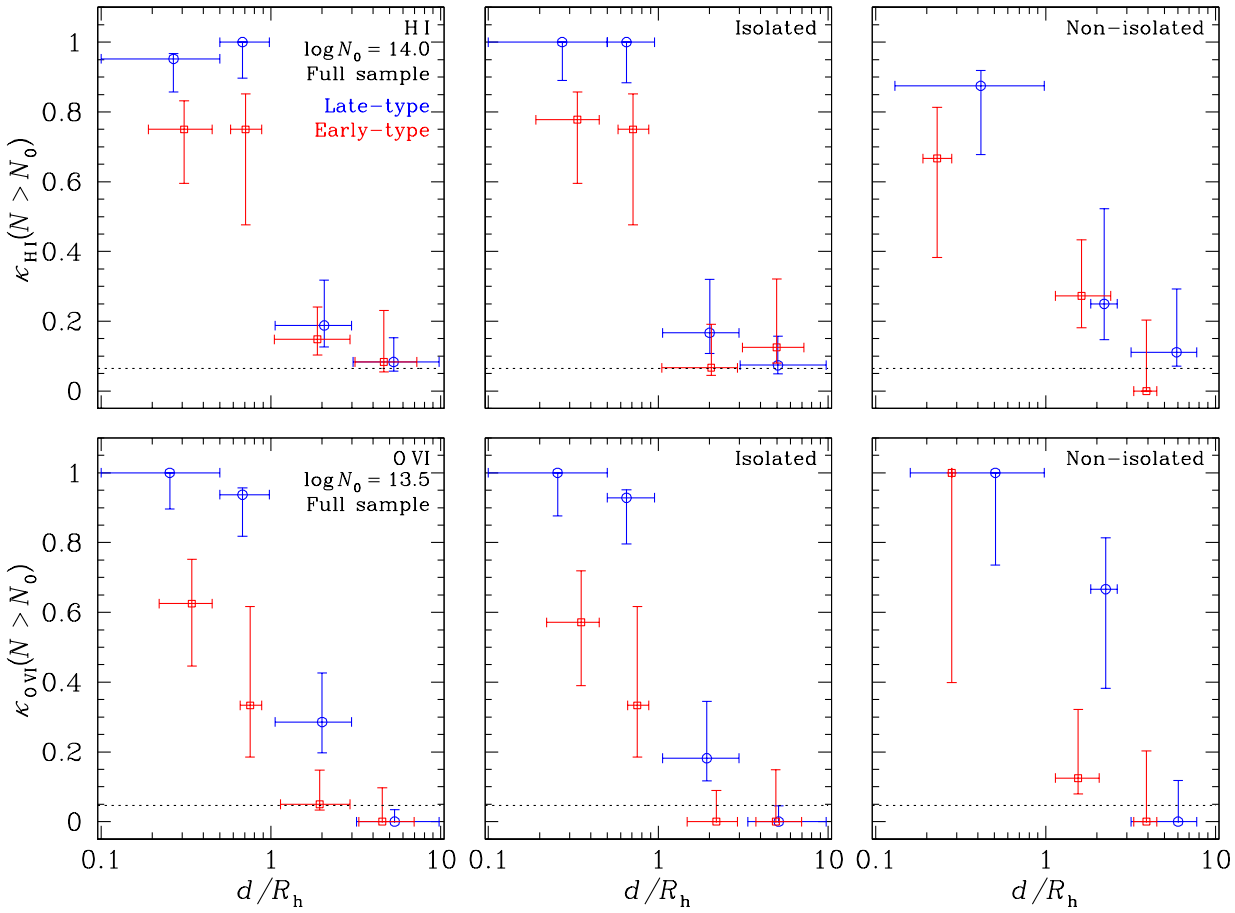

The *top* panels show the covering fraction for H I column density greater than $\log N_0({\rm H\,I})/{\rm cm}^{-2} = 14.0$ and the *bottom* panels show the covering fraction for O VI column density greater than $\log N_0({\rm O\,VI})/{\rm cm}^{-2} = 13.5$. The late-type galaxy samples are shown in blue and early-type in red. The full eCGM and COS-Halos samples are shown on the *left*, isolated galaxies in the *middle*, and non-isolated ones on the *right*. The horizontal error bars mark the full range of galaxies within each bin and vertical error bars represent 68% confidence intervals calculated using standard binomial statistics. We do not include non-detections with column density limits greater than N_0 in the covering fraction calculation. For both H I and O VI, we show the expected covering fraction for random sightlines based $\frac{d^2\mathcal{N}}{dNdz}$ measurements from Danforth et al. (2014).

4.4.1 H I

Consistent with previous surveys (e.g. Chen et al., 2001), we find a clear trend of decreasing H I column density with increasing projected distance (see the top panels of Figures 4.3 and 4.4). Lyman-limit systems (LLS) and partial Lyman-limit systems ($\log N(\mathrm{H\,I})/\mathrm{cm}^{-2} \gtrsim 16$) are common at $d < R_{\mathrm{h}}$, but none are found at larger distances. Considering the eCGM and COS-Halos samples together, we identify strong H I systems with $\log N(\mathrm{H\,I})/\mathrm{cm}^{-2} > 14$ around 48 of 54 galaxies at $d < R_{\mathrm{h}}$ indicating a mean covering fraction of $\langle \kappa_{\mathrm{H\,I}} \rangle = 0.89^{+0.03}_{-0.06}$. At larger distances of $d/R_{\mathrm{h}} = 1 - 3$ such H I absorption systems are found for only 7 of 43 galaxies ($\langle \kappa_{\mathrm{H\,I}} \rangle = 0.16^{+0.07}_{-0.04}$). The H I covering fraction decreases to levels consistent with expectations from coincidental absorption systems unrelated to the galaxy survey members at $d > 3\,R_{\mathrm{h}}$.

To determine whether galaxy environment has an influence on H I absorption far from galaxies, we show the column densities and covering fractions for isolated and non-isolated galaxies in the bottom middle and bottom right panels of Figures 4.3 and 4.4. Though the only two galaxies detected at $d > R_{\mathrm{h}}$ with $\log N(\mathrm{H\,I})/\mathrm{cm}^{-2} \gtrsim 15$ have nearby neighbors, there is no clear enhancement in H I absorption in the non-isolated sample. A series of logrank tests over the range of $d/R_{\mathrm{h}} = 1 - 3$ finds no evidence for differential H I absorption between the isolated and non-isolated samples. We note, however, that contamination from coincidental Lyα absorbers in the IGM is non-neglegible. This contamination may obscure a difference in outer-halo H I absorption between the two samples.

Cross-correlation studies such as Chen & Mulchaey (2009) and Tejos et al. (2014) indicate that strong H I absorption systems primarily reside in the gaseous halos of star-forming galaxies. To investigate the possibility of enhanced H I absorption in galaxies with recent star-formation activity, we show late- and early-type galaxies in blue and red respectively in Figures 4.3 and 4.4. Late-type galaxies exhibit excess H I absorption relative to early-type galaxies at projected distances of $d < R_{\mathrm{h}}$. In particular, we find that 35 of 36 late-type

galaxies at $d < R_{\rm h}$ are associated with H I systems of log N(H I)/cm$^{-2} > 14.0$ indicating a mean covering fraction of $\langle\kappa_{\rm H\,I}\rangle = 0.97^{+0.01}_{-0.06}$ compared to 13 of 18 early-type galaxies ($\langle\kappa_{\rm H\,I}\rangle = 0.72^{+0.08}_{-0.12}$). However, a comparison of the distributions of H I column densities found at $d < R_{\rm h}$ around late- and early-type galaxies is complicated by the poorly determined H I column densities for the LLS and partial-LLS that are common at small projected distances (see discussion in Tumlinson et al., 2013).

At larger distances of $d/R_{\rm h} = 1{-}3$ the H I covering fraction for systems with log N(H I)/cm$^{-2} >$ 14 are similar for late- and early-type galaxies. However, covering fractions are somewhat insensitive to the underlying H I column density distribution. To compare the H I column density distribution of late- and early-type galaxies in the outer halo, we perform a logrank test and find that the probability that the column densities around the two galaxy classes at $d/R_{\rm h} = 1 - 3$ are drawn from the same underlying distribution to be $P = 2\%$. To investigate the nature of this likely differential H I absorption around late- and early-type galaxies at large projected distances, we compare the H I column densities of the two samples using the Kaplan-Meier estimator, an unbiased, non-parametric estimator of cumulative distributions in the presence of upper limits (see Feigelson & Nelson, 1985) in Figure 4.5. We find excess H I absorption around late-type galaxies driven primarily by moderate strength absorption systems of log N(H I)/cm$^{-2} \approx 13.5$ to 14.0. Based on the Kaplan-Meier curves, we infer a median H I column density of $\langle\log N(\mathrm{H\,I})/\mathrm{cm}^{-2}\rangle \approx 13.8$ for late-type galaxies at $d/R_{\rm h} = 1 - 3$. For early-type galaxies, the fraction of H I detections at these distances is too small for a robust measurement of the median, but we are able to place an upper limit on the median H I column density of $\langle\log N(\mathrm{H\,I})/\mathrm{cm}^{-2}\rangle \lesssim 13.4$.

4.4.2 O VI

Like H I, we find a clear anti-correlation between O VI column density and projected distance (see the bottom left panel of Figure 4.3). Strong O VI systems with log N(O VI)/cm$^{-2} \approx$

Figure 4.5: Cumulative fraction, P, of galaxies at $d/R_{\rm h} = 1-3$ with total H I column densities no greater than the value of log N(H I)/cm^{-2} on the x-axis.

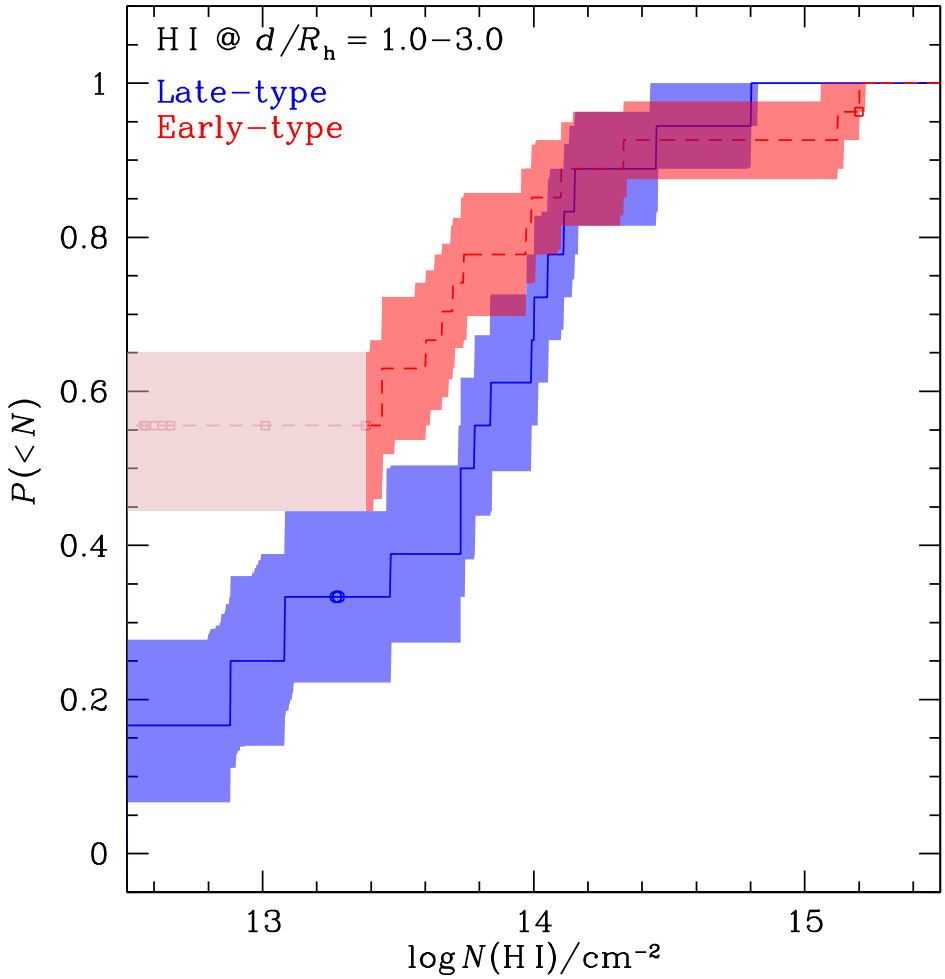

The late-type galaxies are shown in blue solid line and early-type as red dashed line. The cumulative distributions are estimated using the Kaplan-Meier curve, an unbiased, non-parametric estimator of the cumulative distribution in the presence of upper-limits. The Kaplan-Meier estimator changes value at detections but not at non-detections. For clarity, non-detections with upper limits are shown as open symbols. The shaded bands represent 68% confidence intervals including uncertainty due to both sample variance and column density measurement errors calculated with combined boot-strap and Monte-Carlo resampling. At column densities smaller than the highest upper limit that is less than the lowest detection, the Kaplan-Meier estimator represents an upper limit on the cumulative distribution. These column density ranges are shown in faded color.

$14.5 - 15.0$ are common at $d \lesssim R_{\rm h}$ but are rare at larger projected distances. O VI systems with $\log N({\rm O\,VI})/{\rm cm}^{-2} \approx 13.5 - 14.0$ are detected out to $d/R_{\rm h} = 2.3$, but at larger distances, no such strong O VI systems are found. Considering the eCGM and COS-Halos samples as a whole, we find O VI absorption with $\log N({\rm O\,VI})/{\rm cm}^{-2} > 13.5$ for 36 of 42 galaxies at $d < R_{\rm h}$ indicating a mean covering fraction of $\langle \kappa_{\rm O\,VI} \rangle = 0.86^{+0.04}_{-0.07}$. Isolated galaxies exhibit O VI absorption out to $d \approx R_{\rm h}$, beyond the "metal-boundary" seen in C IV and lower ions at $d \approx 0.7\,R_{\rm h}$. At $d/R_{\rm h} = 1 - 3$ strong O VI absorption systems are found for only 5 of 34 galaxies ($\langle \kappa_{\rm O\,VI} \rangle = 0.15^{+0.08}_{-0.04}$). At larger distances of $d > 3\,R_{\rm h}$, the O VI covering fraction decreases to levels consistent with expectations from coincidental absorption systems unrelated to the galaxy survey members (see the bottom left panel of Figure 4.4).

The high completeness of the galaxy survey enables a detailed investigation of possible environmental dependence of extended gas around galaxies. We show O VI column density and covering fraction versus $d/R_{\rm h}$ for isolated and non-isolated galaxies separately in the bottom middle and bottom right panels of Figures 4.3 and 4.4. The decrease in incidence of strong O VI systems at $d \approx R_{\rm h}$ is particularly sharp among isolated galaxies. Of the 51 isolated galaxies at $d > R_{\rm h}$ in the sample we detect $\log N({\rm O\,VI})/{\rm cm}^{-2} > 13.5$ absorption systems for only two galaxies (at $d/R_{\rm h} = 1.1$ and 1.2) indicating a mean covering fraction of $\kappa_{\rm O\,VI} = 0.04^{+0.05}_{-0.01}$. In contrast, three non-isolated galaxies at $d/R_{\rm h} = 1.3, 1.8$, and 2.3 are found to have absorption systems with $\log N({\rm O\,VI})/{\rm cm}^{-2} > 13.5$ out of a sample of 24 such galaxies at $d > R_{\rm h}$ ($\kappa_{\rm O\,VI} = 0.13^{+0.10}_{-0.04}$). This suggests that the O VI absorption around non-isolated galaxies is more extended than around isolated galaxies.

To evaluate the possibility that non-isolated galaxies have more extended O VI absorbing gas, we compare the O VI column density distributions of the isolated and non-isolated galaxy samples at $d > 1.5\,R_{\rm h}$. A logrank test finds that the probability that the O VI column densities of the isolated and non-isolated galaxies at $d > 1.5\,R_{\rm h}$ are drawn from the same underlying distribution to be $P < 1\%$. The results of the logrank test are insensitive to

the choice of $d > 1.5\,R_{\rm h}$ cut-off and return a result of $P < 1\%$ over the full range of cut-off distances between 1.2 and $1.8\,R_{\rm h}$ and $P < 2\%$ between 1.1 and $2.2\,R_{\rm h}$. These findings indicate that galaxies with nearby neighbors exhibit more extended O VI absorbing gas than isolated galaxies.

Though the completeness of our galaxy survey is high, it is possible that the detections of O VI at large distances from non-isolated galaxies could be due to the presence of an additional neighbor closer to the sightline that was not observed in our survey. However, the survey incompleteness applies to the isolated and non-isolated galaxies equally. In addition, the galaxy survey completeness levels increase at small projected distances from the quasar sightline (see Figure 2 of Johnson et al., 2013). In particular, at the redshifts and distances of the non-isolated galaxies detected in O VI absorption at $d > R_{\rm h}$, our galaxy survey data are $> 90\%$ complete for galaxies as faint as $0.1\,L_*$.

Previous surveys (e.g. Chen & Mulchaey, 2009; Tumlinson et al., 2011) found that late-type galaxies exhibit enhanced O VI absorption relative to more massive early-type galaxies at $d \lesssim 150$ kpc. We confirm that late-type galaxies show enhanced O VI absorption at $d < R_{\rm h}$ relative to early-type ones. However, O VI absorption systems with $\log N({\rm O\,VI})/{\rm cm}^{-2} > 13.5$ are found for six of eleven early-type galaxies at $d < R_{\rm h}$ indicating a non-negligible covering fraction of $\langle \kappa_{\rm O\,VI} \rangle \approx 0.55^{+0.13}_{-0.14}$. At larger distances of $d/R_{\rm h} = 1 - 3$ we find O VI absorption with $\log N({\rm O\,VI})/{\rm cm}^{-2} > 13.5$ for four of 14 late-type galaxies $\langle \kappa_{\rm O\,VI} \rangle \approx 0.29^{+0.14}_{-0.09}$ compared to one of 19 early-type galaxies $\langle \kappa_{\rm O\,VI} \rangle \approx 0.05^{+0.10}_{-0.02}$. Interestingly, the only early-type galaxy exhibiting a strong O VI system at $d > R_{\rm h}$ is the brightest member of a maxBCG cluster (Koester et al., 2007) at $d = 1.3\,R_{\rm h}$ from the quasar sightline. A logrank test finds that the probability that the O VI column densities found at $d/R_{\rm h} = 1 - 3$ from late- and early-type galaxies are drawn from the same underlying distribution to be $P = 1\%$. We note that the O VI excess in the outer halos of late-type galaxies is driven by absorption systems with $\log N({\rm O\,VI})/{\rm cm}^{-2} \approx 13.5 - 14.0$ while the excess at smaller projected distances is driven by

stronger systems with $\log N(\mathrm{O\,VI})/\mathrm{cm}^{-2} \approx 14.5$.

4.5 Discussion

Using a highly complete survey ($\gtrsim 80\%$) of faint galaxies ($L > 0.1\,L_*$) at $z < 0.4$ and $d < 500$ kpc in the fields of four COS quasar sightlines with high signal-to-noise spectra available in the Mikulski Archive for *HST*, we have searched for the key features that determine the extended gaseous properties of galaxy halos in H I and O VI absorption. Our main findings are:

1. galaxies with nearby neighbors exhibit enhanced O VI absorption at $d > R_{\rm h}$ relative to isolated galaxies;

2. among isolated galaxies, O VI absorption extends to $d \approx R_{\rm h}$, beyond the extent observed in lower ionization species such as Si III and C IV; and

3. late-type galaxies exhibit enhanced H I and O VI absorption beyond characteristic halo radii at $d/R_{\rm h} = 1 - 3$.

4.5.1 Possible environmental effect in distributing heavy elements to $d > R_{\rm h}$

Among isolated galaxies without neighbors within 500 kpc and with stellar mass ratio greater than one-third, we find that O VI absorption is confined to within $d < 1.2\,R_{\rm h}$. None of the 18 isolated galaxies at $d/R_{\rm h} = 1.2-3.0$ in our survey are found to have O VI absorption in the COS quasar spectrum. In contrast, three out of ten galaxies with nearby neighbors probed at $d/R_{\rm h} = 1.2 - 3.0$ are found to exhibit O VI absorption with $\log N(\mathrm{O\,VI})/\mathrm{cm}^{-2} > 13.5$. On the other hand, no evidence for differential H I absorption is found between the isolated and non-isolated galaxy samples. These findings suggest that galaxy interactions play a key role in distributing heavy elements to large distances from galaxy centers, well beyond the enriched gaseous halos that surround individual galaxies.

Galaxy interactions can produce heavy elements at large projected distances through tidal stripping during satellite accretion (e.g. Wang, 1993) or ram-pressure stripping (e.g. Gunn & Gott, 1972). Recently, *HST* images of galaxy clusters have revealed that ram pressure stripping can remove and compress copious amounts of gas from in-falling galaxies as evidenced by vigorous starbursts in debris trails (Ebeling et al., 2014). Moreover, a galaxy survey in the field of an ultra-strong Mg II absorption system near a luminous red galaxy revealed a group of evolved galaxies with no evidence of recent star-formation activity (Gauthier, 2013). The lack of star-formation in the group and kinematics of the Mg II absorption are most readily explained if the Mg II absorber arises from stripped gas. Finally, in Johnson et al. (2014) we presented the discovery of a "transparent" sightline with no strong H I, Mg II or O VI absorption at $d < 20$ kpc from a pair of strongly interacting galaxies separated by a projected distance of 9 kpc. The lack of strong absorption systems detected at such small projected distance from this galaxy pair can be explained if the inner halo gas of the two galaxies has been stripped to larger distances during the galaxy interaction.

4.5.2 Comparison with Prochaska et al. 2011

Prochaska et al. (2011b) found that galaxies at $z \lesssim 0.1$ and of $-21.1 < M_r < -18.6$ exhibit near unity covering fraction at $d < 300$ kpc and concluded that such "sub-L_*" galaxies possess O VI bearing gaseous halos that extend to $d \approx 3\,R_{\rm h}$. Our highly complete galaxy survey data shed new light on these observations, indicating that O VI absorption at such large distances from galaxy halos arise in systems of multiple galaxies. Indeed, a literature search of the NASA Extragalactic database for spectroscopic neighbors reveals that all of the galaxies of $-21.1 < M_r < -18.6$ from Prochaska et al. (2011b) with O VI absorption at $d \gtrsim R_{\rm h}$ have neighbors within $d = 500$ kpc and satisfy our definition of a non-isolated galaxy (see Figure 4.6). The data from Prochaska et al. (2011b) are therefore consistent with our conclusion that isolated galaxies exhibit low covering fractions at $d \gtrsim 1.2\,R_{\rm h}$ and support the

possibility that galaxy interactions are effective at producing O VI absorbing gas at large projected distances.

4.5.3 O VI absorption in isolated galaxies beyond the "metal-boundary" at $d/R_{\rm h} = 0.7$

Even among isolated galaxies, O VI absorption extends beyond the "metal-boundary" observed by Liang & Chen (2014) at $d = 0.7\,R_{\rm h}$ in lower-ionization state, enriched gas traced by absorbers such as Si II, Si III, C II, and C IV. Specifically, we find O VI absorption for seven of ten isolated galaxies at $d/R_{\rm h} = 0.7$ to 1.2. The presence of O VI absorption in the outer regions of isolated galaxy halos indicates some heavy element enrichment at large radii and that highly ionized, O VI bearing clouds can form or survive in the outer halo while Si II, Si III, and C IV bearing clouds cannot. Using the mean absorption found in a stack of isolated galaxies in the eCGM and COS-Halos samples at $d/R_{\rm h} = 0.7 - 1.2$, we estimate the mean metallicity of these clouds. In the stack, we measure absorption of $\log N({\rm H\,I})/{\rm cm}^{-2} = 14.4$, $\log N({\rm O\,VI})/{\rm cm}^{-2} = 13.9$, and place an upper limit on C III absorption of $\log N({\rm C\,III})/{\rm cm}^{-2} < 12.6$. Assuming photoionization equilibrium models calculated with Cloudy (Ferland et al., 1998) Version 10.0, a photoionization background from Haardt & Madau (2012) at $z = 0.2$, and solar abundance patterns, these mean column densities are consistent with gas in photoionization equilibrium with ionization parameter $\log U = -1.1$ and a metallicity of one-tenth solar. The O VI and H I bearing gas may not be co-spatial allowing the ionization parameter of the H I gas to be lower. If this is the case, then the upper limit on C III absorption places stricter upper limits on the mean gas metallicity. We therefore place an upper limit of one-tenth solar on the mean metallicity of outer-halo H I gas clouds at $d \approx R_{\rm h}$. This is consistent with the metallicity upper limit of one-tenth solar found by Liang & Chen (2014) based on C IV non-detections at $d > 0.8\,R_{\rm h}$.

Figure 4.6: O VI column density versus $d/R_{\rm h}$ for sub-L_* galaxies of $-21.1 < M_r < -18.6$.

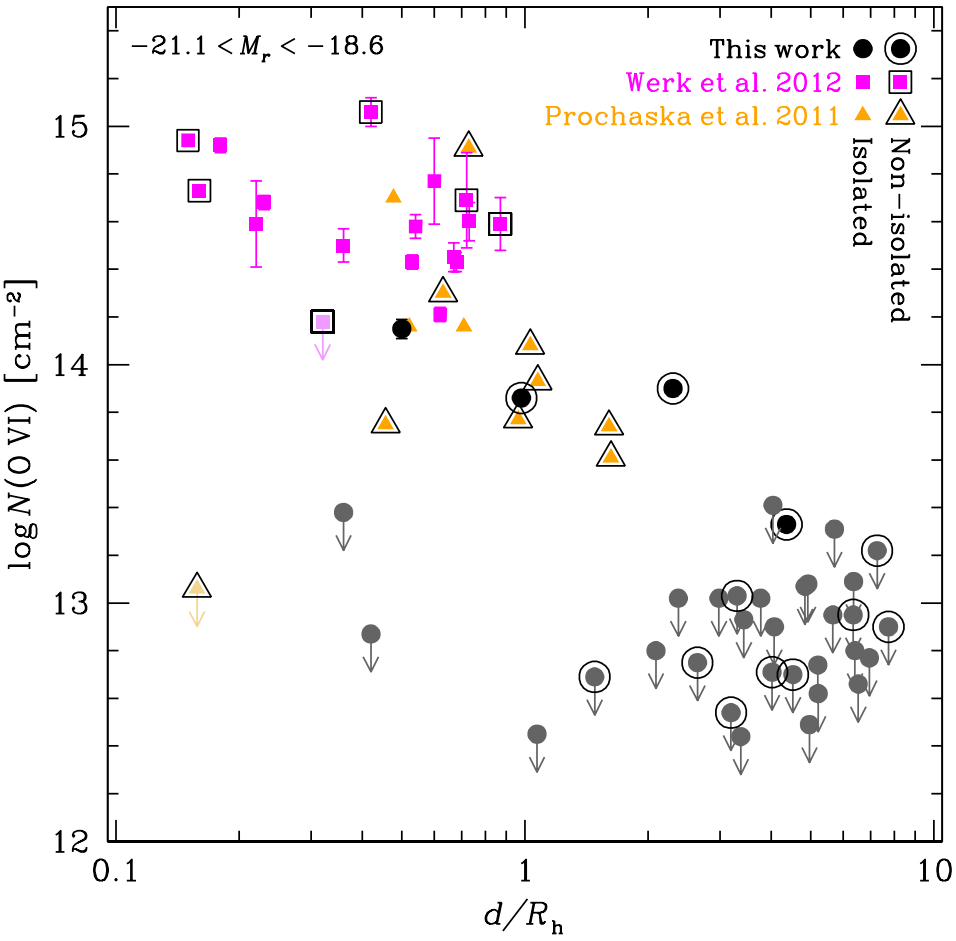

Galaxies from the eCGM survey are shown as black circles, those from Werk et al. (2012) as magenta squares, and those from Prochaska et al. (2011b) as orange triangles. Non-isolated galaxies are outlined by large black symbols.

4.5.4 Differential H I and O VI absorption between late- versus early-type galaxies

We find excess H I and O VI absorption around late-type galaxies relative to early-type ones at $d/R_{\rm h} = 1-3$ with 99% and 98% confidence respectively, extending previous results from Chen & Mulchaey (2009), Tumlinson et al. (2011), and Tejos et al. (2014) to larger distances. The O VI excess around late-type galaxies could be explained if the ionization mechanisms that produce O VI absorbing gas are the result of star-formation (e.g. photoionization from a young stellar population). However, this is not consistent with the observed H I excess unless the ionization mechanism is effective at producing highly ionized heavy element species but ineffective at ionizing hydrogen (e.g. Auger ionization).

Higher levels of H I and O VI absorption around late-type galaxies could be simultaneously explained if the absorption systems trace starburst driven outflows. However, simulations from Oppenheimer & Davé (2008) that incorporate strong, momentum-driven winds find that these outflows are characterized by a turnaround radius of $R_{\rm turn} = 80 \pm 20$ kpc with only weak dependence on mass and redshift at $z < 1$. For the late-type galaxies in our survey, this corresponds to only $R_{\rm turn}/R_{\rm h} \approx 0.4$, far less than $d/R_{\rm h} = 1-3$. Alternatively, the excess H I and O VI absorption at large distances from late-type galaxies can be explained if H I, O VI, and star-formation are observational signatures of halos in cosmic environments with multi-phase gaseous reservoirs.

The late-type members of the eCGM and COS-Halos galaxy samples are systematically less massive than the early-type members with mean stellar masses of $\log\langle M_*/M_\odot\rangle = 10.2, 10.9$ corresponding to inferred halo masses of $\log\langle M_h/M_\odot\rangle = 11.7, 12.6$ respectively. The mean doppler parameter of the H I absorption components detected at $d/R_{\rm h} = 1-3$ from eCGM galaxies is $b = 40$ km s^{-1} which indicates that the H I absorbers trace cool-warm, $T \lesssim 10^5$ K gas. Our survey data are therefore consistent with a decreased incidence of cool-warm gas around more massive halos. This extends previous results from Gauthier et al. (2010) and

Yoon et al. (2012) who found reduced cool-warm gas absorption in $> 10^{13} M_{\odot}$ mass halos relative to less massive ones. A larger sample of early-type galaxies probed in absorption is required to differentiate the effects of recent star-formation activity and mass.

Acknowledgements

We thank Michael Rauch, Gwen Rudie, Juna Kollmeier, Don York, Jean-René Gauthier, Rik Williams, Cameron Jia Liang, Daniel D. Kelson, and Andrey Kravtsov for many helpful discussions. SDJ gratefully acknowledges support from The Brinson Foundation and The Observatories of the Carnegie Institute for Science who generously supported and hosted his studies in 2013-2014.

This chapter includes data gathered with the 6.5 meter Magellan Telescopes located at Las Campanas Observatory, Chile.

Based on observations made with the NASA/ESA Hubble Space Telescope, obtained from the Data Archive at the Space Telescope Science Institute, which is operated by the Association of Universities for Research in Astronomy, Inc., under NASA contract NAS 5-26555.

Funding for SDSS-III has been provided by the Alfred P. Sloan Foundation, the Participating Institutions, the National Science Foundation, and the U.S. Department of Energy Office of Science. The SDSS-III web site is http://www.sdss3.org/. SDSS-III is managed by the Astrophysical Research Consortium for the Participating Institutions of the SDSS-III Collaboration including the University of Arizona, the Brazilian Participation Group, Brookhaven National Laboratory, Carnegie Mellon University, University of Florida, the French Participation Group, the German Participation Group, Harvard University, the Instituto de Astrofisica de Canarias, the Michigan State/Notre Dame/JINA Participation Group, Johns Hopkins University, Lawrence Berkeley National Laboratory, Max Planck Institute for Astrophysics, Max Planck Institute for Extraterrestrial Physics, New Mexico State University,

New York University, Ohio State University, Pennsylvania State University, University of Portsmouth, Princeton University, the Spanish Participation Group, University of Tokyo, University of Utah, Vanderbilt University, University of Virginia, University of Washington, and Yale University.

This research made use of NASA's Astrophysics Data System (ADS) and the NASA/IPAC Extragalactic Database (NED) which is operated by the Jet Propulsion Laboratory, California Institute of Technology, under contract with the National Aeronautics and Space Administration.

Funding for PRIMUS is provided by NSF (AST-0607701, AST-0908246, AST-0908442, AST-0908354) and NASA (Spitzer-1356708, 08-ADP08-0019, NNX09AC95G).

This research draws upon data provided by Brian Keeney as distributed by the NOAO Science Archive. NOAO is operated by the Association of Universities for Research in Astronomy (AURA) under cooperative agreement with the National Science Foundation.

CHAPTER 5

ON THE ORIGIN OF EXCESS COOL GAS IN QUASAR HOST HALOS

The contents of this chapter have been published in the Monthly Notices of the Royal Astronomical Society and are reproduced here in accordance with the copyright agreement and with permission from the Oxford University Press.

Johnson, S. D., Chen, H.-W., & Mulchaey, J. S. 2015, MNRAS, 452, 2553

5.1 Introduction

In order to reproduce the low stellar-to-halo mass ratios of high mass galaxies (e.g. Conroy & Wechsler, 2009; Behroozi et al., 2013; Kravtsov et al., 2014) both semi-analytic (e.g. Benson et al., 2003) and hydrodynamic simulations of galaxy evolution must incorporate strong feedback from active galactic nuclei (AGN) and quasars (for a recent review, see Kravtsov & Borgani, 2012). Moreover, hydrodynamic simulations of galaxy evolution that incorporate AGN feedback are better able to reproduce the properties of galaxies observed in emission (e.g. Springel et al., 2005; Di Matteo et al., 2005; Sijacki et al., 2007; Schaye et al., 2010; Gabor & Davé, 2012; Vogelsberger et al., 2013; Li & Bryan, 2014). While promising, these implementations of quasar feedback are subject to significant systematic uncertainties driven by poorly constrained aspects of quasar and AGN physics, and direct observations of quasar feedback are available for only a small number of systems (for a recent review, see Fabian, 2012).

The low-density gas of the circum-galactic medium (CGM) provides a sensitive laboratory for discriminating between possible feedback models, and different feedback prescriptions result in order-of-magnitude changes in CGM observables predicted in hydrodynamic simulations of galaxies (Hummels et al., 2013; Ford et al., 2013; Shen et al., 2013a; Agertz & Kravtsov,

2015; Suresh et al., 2015). The density of the CGM is nearly always too low to be studied in emission with existing facilities, but significant progress can be made by studying the gas in absorption when bright background objects are serendipitously found at low projected distances, d, from foreground galaxies.

Over the last decade, large samples totaling nearly one thousand galaxies at $z \approx 0$ to 2 with constraints on extended gas properties from absorption spectroscopy have been assembled using a combination of ground and space-based telescopes. In particular, observations of the H I Lyman series (e.g. Chen et al., 1998; Tripp et al., 1998; Wakker & Savage, 2009; Stocke et al., 2013; Rudie et al., 2013; Tumlinson et al., 2013) and doublet transitions due to heavy element ions such as Mg II (e.g. Bowen et al., 1995; Chen et al., 2010a; Gauthier et al., 2010; Bordoloi et al., 2011; Lovegrove & Simcoe, 2011), C IV (e.g. Chen et al., 2001; Borthakur et al., 2013; Liang & Chen, 2014; Bordoloi et al., 2014), and O VI (e.g. Chen & Mulchaey, 2009; Wakker & Savage, 2009; Prochaska et al., 2011b; Tumlinson et al., 2011; Mathes et al., 2014; Stocke et al., 2014; Turner et al., 2014; Johnson et al., 2015b) have been particularly fruitful.

Recently, observing campaigns leveraging large imaging and spectroscopic surveys such as the Sloan Digital Sky Survey (SDSS; York et al., 2000) and dedicated campaigns on large, ground-based telescopes have extended the study of the relationship between galaxy and halo gas properties to galaxies hosting quasars using projected quasar-quasar pairs. Foreground quasars at both $z \approx 1$ and $z > 2$ exhibit a high incidence of optically thick, metal-enriched absorption systems traced by H I Lyα, C II, C IV, and Mg II absorption along the transverse direction at $d \lesssim 300$ kpc but low incidence along the foreground quasar sightline itself (Bowen et al., 2006; Hennawi et al., 2006; Hennawi & Prochaska, 2007; Farina et al., 2013; Hennawi & Prochaska, 2013; Prochaska et al., 2013; Farina et al., 2014; Prochaska et al., 2014). This contrast indicates that the ionizing emission from quasars is highly anisotropic, in qualitative agreement with the unified theory of AGN (e.g. Antonucci, 1993; Netzer, 2015).

The high incidence of optically thick gas at $d < 300$ kpc from quasars at $z \approx 2$ is in significant excess relative to that found for inactive galaxies both at $z < 1$ (Chen et al., 2010a; Gauthier et al., 2010; Lovegrove & Simcoe, 2011) and at $z \approx 2$ (Rudie et al., 2012). Insights into the possible origin of this excess gas can be gained from state-of-the-art hydrodynamic simulations that include stellar but not AGN feedback (e.g. Fumagalli et al., 2014). In particular, simulations with stellar feedback are able to comfortably reproduce the observed incidence of Lyman-limit systems around inactive, Lyman-break galaxies at $z \approx 2$ but underpredict the incidence around quasar hosts by more than a factor of two (Faucher-Giguère et al., 2015). This discrepancy suggests that AGN feedback may be responsible for the excess observed in absorption around quasar hosts. Alternatively, the discrepancy could be the result of an inability of the simulations to resolve the physical scales relevant to the formation or survival of cool gas clouds in massive halos (Fumagalli et al., 2014; Meiksin et al., 2015) or if a substantial portion of the gas arises in less luminous galaxies neighboring the quasar hosts (Rahmati et al., 2015; Suresh et al., 2015).

To better understand the relationship between AGN activity and halo gas, we searched the SDSS Data Release 12 (Eisenstein et al., 2011; Alam et al., 2015) and compiled an exhaustive sample of 195 quasars at $z \approx 1$ with constraints on Mg II absorption at $d < 300$ kpc from background quasars. This large dataset enables a search for correlations between quasar properties and extended, cool circumgalactic gas around the quasar hosts.

The chapter proceeds as follows: In Section 5.2 we describe the quasar sample and corresponding absorption-line measurements. In Section 5.3, we characterize the absorption as a function of projected distance, redshift, and quasar luminosity. In Section 5.4, we discuss the implications of our findings.

Throughout the chapter, we adopt a Λ-cosmology with $\Omega_{\rm m} = 0.3$, $\Omega_\Lambda = 0.7$, and $H_0 = 70\,{\rm km\,s^{-1}\,Mpc^{-1}}$. All magnitudes are in the *AB* system (Oke & Gunn, 1983) and corrected for foreground Milky Way extinction following Schlafly & Finkbeiner (2011).

5.2 Quasar sample

To compile a large sample of foreground-background quasar[1] pairs with constraints on Mg II absorption, we retrieved a list of the 395,281 quasars classified by the SDSS-III automated classification and redshift measurement pipeline (Bolton et al., 2012) as of Data Release 12. From this sample, we selected foreground-background quasar pairs that meet the following criteria:

1. The projected distance between the foreground and background quasars at the foreground quasar redshift satisfies $d < 300$ kpc.

2. The velocity difference between the foreground and background quasars satisfies $\Delta v(z_{\rm b}, z_{\rm f}) < -10,000$ km s^{-1}.

3. The expected wavelengths of the Mg II doublet at the redshift of the foreground quasar is covered by the SDSS spectrum of the background quasar.

4. The expected wavelengths of the Mg II doublet is outside of the Lyα forest in the background quasar spectrum. and

5. The signal-to-noise ratio in the background quasar spectrum is sufficient to detect a moderate strength Mg II absorption system with rest-frame equivalent width of $W_{\rm r}(2796) > 0.3$ Å at 3-σ significance at the foreground quasar redshift (a signal-to-noise ratio of 20 per SDSS resolution element).

The upper limit on the projected distance was chosen to correspond to the expected virial radii of quasar host halos at $z > 0.4$. The requirement that $\Delta v < -10,000$ was chosen to avoid confusion with gas outflowing from the background quasar (e.g. Wild et al., 2008). The requirement that the wavelengths of the Mg II doublet at the foreground quasar redshift

1. Throughout this chapter, we refer to objects with broad-line emission and power-law dominated continua as quasars irrespective of the sub-division of AGN into quasars and Seyferts based on luminosity.

Table 5.1: Summary of foreground quasar and transverse Mg II absorption properties. The full table is available in the on-line version of Johnson et al. (2015a)

	Foreground quasar						Absorption properties		
Name	Right Ascension (J2000)	Declination (J2000)	z[a]	$\log L_{\rm bol}/{\rm erg\,s^{-1}}$	$\Delta\theta$ ($''$)	d (kpc)	$W_{\rm r}(2796)$[b] (Å)	Δv (km s^{-1})	Ref.[c]
J0954+3734	09:54:54.70	+37:34:19.7	1.544	46.3	3.1	26	1.10 ± 0.17	660	1
J0836+4841	08:36:49.40	+48:41:50.0	0.657	45.7	4.1	28	1.90 ± 0.11	−130	1
J0842+4733	08:42:57.37	+47:33:42.6	1.556	46.5	3.4	29	3.70 ± 0.30	−790	4
J1550+1120	15:50:43.59	+11:20:47.5	0.4358	46.0	5.2	29	< 0.25	n/a	4
J1106+4635	11:06:17.17	+46:35:24.5	1.602	46.5	4.4	37	1.12 ± 0.15	−130	4
J1108+3306	11:08:07.90	+33:06:11.3	1.502	46.5	5.5	46	5.75 ± 0.26	810	4
J0938+5317	09:38:04.21	+53:17:43.9	2.063	45.9	5.7	47	0.48 ± 0.04	310	3
J2312+1444	23:12:52.70	+14:44:58.6	0.7678	45.2	6.4	47	0.39 ± 0.12	−100	1
J1427−0121	14:27:58.88	−01:21:30.3	2.281	46.6	6.2	51	0.45 ± 0.02	−80	3
J0909+1629	09:09:57.08	+16:29:06.5	0.7275	45.2	7.1	51	< 0.15	n/a	4

Notes

[a] Quasars with redshifts from narrow [O II] or [O III] are shown to four decimal places and three decimal places otherwise.

[b] For non-detections, we report 3-σ upper limits integrated over a 250 km s^{-1} velocity interval.

[c] Reference: 1 → Bowen et al. (2006), 2 → Farina et al. (2013, 2014), 3 → Prochaska et al. (2014), 4 → This work

fall outside of the Lyα forest in the background quasar spectrum was chosen to ensure that absorption attributed to Mg II is not the result of coincidental Lyα absorption systems. Finally, the requirement that the signal-to-noise ratio in the background quasar spectrum is sufficient to detect absorption systems of $W_{\rm r}(2796) > 0.3$ Å was chosen to correspond to the typical sensitivities of existing studies of Mg II absorption around quasars at $z \approx 1$ (e.g. Farina et al., 2013, 2014).

The search yielded a sample of 195 foreground-background quasar pairs which we visually inspected to ensure that the automated classifications as broad-line (Type 1) quasars and redshifts from the SDSS database are robust. For each of the 195 quasar pairs, we then measured foreground quasar properties and Mg II absorption properties as described in Sections 5.2.1 and 5.2.2 respectively. The sample is summarized in Table 5.1.

5.2.1 Foreground quasar redshifts and luminosities

Quasar redshifts from the SDSS pipeline are biased by ≈ 600 km s^{-1} due to asymmetric, blue-shifted emission profiles of broad-line region emitting gas (Gaskell, 1982; Tytler & Fan, 1992; Richards et al., 2002; Hewett & Wild, 2010). This bias exceeds the velocity difference typically found between galaxies and associated Mg II absorption at $d < 150$ kpc (Chen et al., 2010a) so more accurate redshifts are required. When available, we adopted redshifts from Hewett & Wild (2010) and otherwise, we calculated the quasar redshifts using the template and cross-correlation techniques described in Hewett & Wild (2010). In addition, for quasars with narrow [O II] or [O III] emission, we measured the redshifts from these narrow emission lines by fitting gaussian profiles and adopting the rest-frame line centroid wavelengths from Hewett & Wild (2010).

Uncertainties in narrow-line based redshifts due to centroid uncertainties are typically small, $\sigma \approx 30$ km s^{-1}, but [O III] redshifts can be blueshifted due to outflows in the narrow-line region (Boroson, 2005). To evaluate the significance of this bias, we compared [O II]

and [O III] emission redshifts for quasars within our SDSS sample and found a mean bias of $\Delta v(z_{\rm O\,II}, z_{\rm O\,III}) = -30$ km s^{-1} with a 1-σ scatter of 70 km s^{-1}.

Broad-line based cross-correlation redshifts exhibit larger scatter with significant, non-Gaussian wings in the redshift error distribution due to population variance in broad-line profiles. To evaluate the uncertainties in our broad-line based redshifts, we remeasured the cross-correlation redshifts for quasars with narrow-line emission but with the narrow-lines masked during the cross-correlation. We then compared these broad-line redshifts with the narrow-line redshifts. The bias in the broad-line based cross-correlation redshifts is consistent with zero and the 68%, 95%, 99%, and 99.7% uncertainties correspond to $150, 370, 1000$, and 1500 km s^{-1} respectively.

In addition to improved redshifts, we measured quasar bolometric luminosities based on monochromatic, continuum luminosity measurements and the bolometric corrections from Richards et al. (2006). The monochromatic luminosities were estimated by fitting a power-law continuum plus Fe II template (Vestergaard & Wilkes, 2001) model to line-free continuum regions of the SDSS quasar spectra with rest-frame wavelength intervals of $\lambda_r = 1350-1360, 1445-1465, 1700-1705, 2155-2400, 2480-2675$, and $2925-3500$ Å. The uncertainties in the quasar bolometric luminosities are dominated by sample variance in quasar spectral energy distributions which result in errors of ≈ 0.3 dex (see discussion in Richards et al., 2006).

In order to include previously reported quasars with absorption line constraints at $d < 300$ kpc, we measured bolometric luminosities for quasars from Bowen et al. (2006); Farina et al. (2013, 2014) and Prochaska et al. (2014) with available SDSS spectra using the same techniques. For the quasars from Farina et al. (2013) and Farina et al. (2014) without SDSS spectra we adopted the bolometric luminosity estimates reported by Farina et al. (2013) and Farina et al. (2014) which were measured using a similar continuum fitting procedure. For those quasars from Bowen et al. (2006) and Prochaska et al. (2014) without

public spectra, we estimated luminosities by finding close matches in redshift and apparent magnitude space in the quasar sample from Shen et al. (2011) which has monochromatic luminosities estimated from continuum fitting. These broad-band based luminosities reproduce spectroscopic measurements with a standard deviation of 0.2 dex.

The redshift, luminosity, and projected distance distributions of the resulting quasar catalogs are displayed in the Figure 5.1. The samples from Bowen et al. (2006), Farina et al. (2013), Farina et al. (2014), and this work are characterized by mean redshifts of $\langle z \rangle \approx 1$ while the sample from Prochaska et al. (2014) is characterized by $\langle z \rangle = 2.2$. The quasar sample presented in this chapter spans a luminosity range of $\log L_{\rm bol}/{\rm erg\,s^{-1}} = 44.4$ to 46.8 (see the left panel of Figure 5.1), extending the study of gas in absorption around quasars to lower luminosities than were previously available.

5.2.2 Absorption-line measurements

In order to place constraints on the transverse Mg II absorption near the foreground quasars, we visually searched the background quasar spectra for possible Mg II λ2796 absorption within $|\Delta v| < 1500$ km s^{-1} of the foreground quasar redshift. The large search window was chosen to ensure that uncertainties in broad-line based quasar redshifts do not bias the results of this study. In addition, this velocity search window is the same as was used by Prochaska et al. (2014) which simplifies the comparison between that work and our $z \approx 1$ sample.

When absorption was identified, we measured the absorption equivalent width and centroid in the following steps. First, we locally fit the continuum by defining feature-free continuum regions at lower and higher wavelengths and fit an outlier-resistant line to these continuum regions. We then continuum normalized the flux and error arrays and calculated the rest-frame equivalent width and equivalent width error by direct integration over a user-defined interval. We accepted the absorption according to a 3-σ detection threshold and additionally required that the identification of the absorption feature as Mg II λ2796 be confirmed by the

Figure 5.1: Characterization of the foreground quasar sample

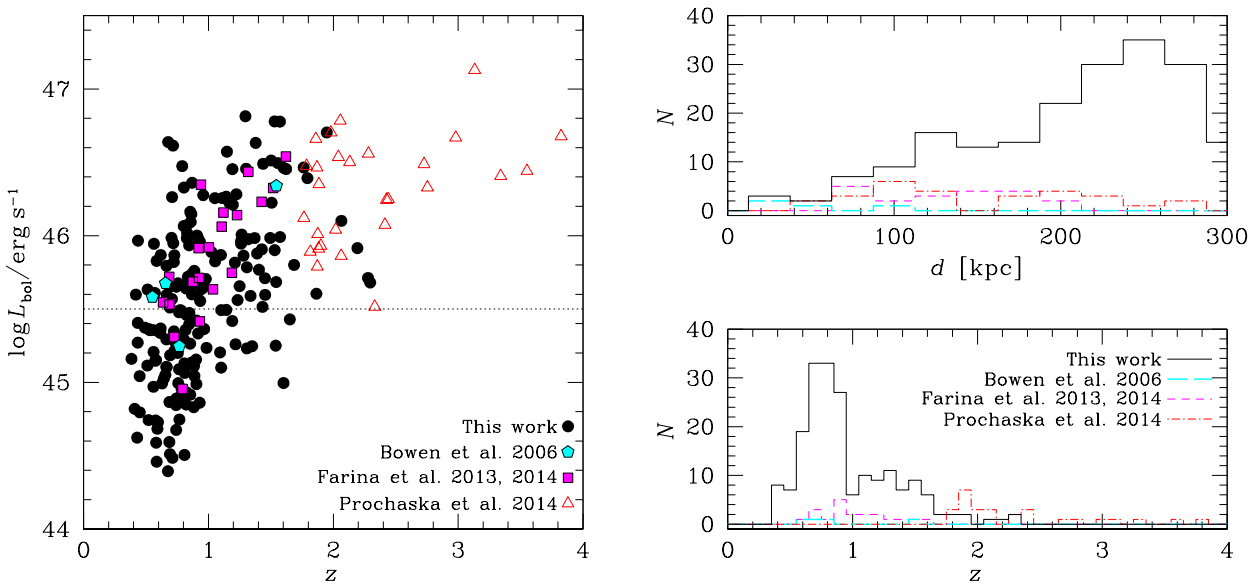

left: Bolometric luminosity of the foreground quasars versus foreground quasar redshift. The horizontal dotted line marks $\log L_{\rm bol}/{\rm erg\,s^{-1}} = 45.5$, the division between the luminous and low-luminosity quasars used throughout the chapter. *right*: Projected distance (*top*) and redshift (*bottom*) histograms. In all three panels, quasars from Bowen et al. (2006), Farina et al. (2013) or Farina et al. (2014), Prochaska et al. (2014), and this work are displayed in cyan, magenta, red, and black respectively, with symbols and line-styles indicated in the legend. The quasars from Bowen et al. (2006), Farina et al. (2013), Farina et al. (2014), and this work have available constraints on the transverse Mg II absorption from the spectra of background quasars. Mg II absorption constraints are unavailable for the quasar sample from Prochaska et al. (2014) due to the higher redshift range. For these quasars, C II rather than Mg II serves as a signature of cool, high H I column density gas.

presence of at least one other absorption feature at the same redshift (e.g. Mg II λ2803, Mg I λ2852, or Fe II $\lambda\lambda$2344, 2374, 2382, 2586, 2600). Finally, we measured the absorber centroid and full-width-at-half-maximum (FWHM) by fitting a gaussian profile to the Mg II λ2796 absorption and used the centroid to measure the absorber redshift. In a few cases, multiple absorption components are found at $|\Delta v| < 1500$ km s^{-1}. For these quasars, we report the total Mg II λ2796 equivalent width and report $\Delta\, v$ for the strongest component. Each of these cases is discussed further in Section 5.3.2.

In the case of non-detections, we placed 3-σ upper limits on the Mg II λ2796 equivalent width by integrating the continuum normalized error array over a 250 km s^{-1} window centered at the foreground quasar redshift. The 250 km s^{-1} window corresponds to the mean FWHM of Mg II λ2796 detections in our sample. Two example quasars probed in absorption, one with detected Mg II absorption and one without, are showcased in Figure 5.2 to demonstrate the data quality afforded by the SDSS spectra.

In one case, J1250$-$0105, we identified possible Mg II λ2796 absorption with 3-σ significance but were unable to confirm the identification by detection of another line. For this quasar, we placed a limit on the Mg II λ2796 equivalent width by measuring the limit on Mg II λ2803 and multiplied by two (the ratio of the oscillator strengths of the two transitions). We note that the results presented in this chapter do not change if the possible Mg II λ2796 absorption for this quasar is treated as a detection.

In a few cases, we detected absorption from the Mg II doublet but with the λ2796 member contaminated by heavy element absorption from another absorption system at a distinct redshift. For these objects, we fitted the Mg II and contaminating absorption profiles using the VPFIT package (Carswell et al., 1987; Carswell & Webb, 2014) and measured Mg II λ2796 equivalent width from the model fit.

Finally, we added absorption-line measurements from the foreground-background quasar samples previously reported in the literature in Bowen et al. (2006); Farina et al. (2013, 2014),

Figure 5.2: Example quasars probed in Mg II absorption

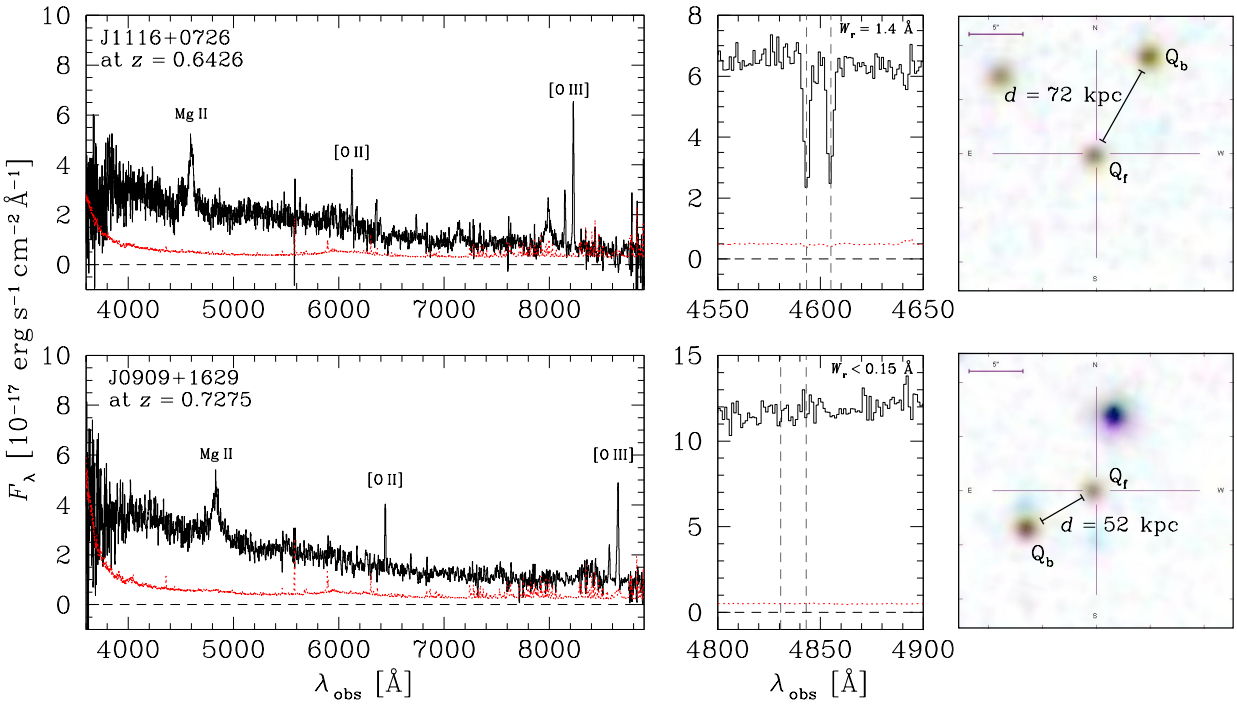

The *top* panels display a quasar detected in Mg II absorption at $d = 72$ kpc and the bottom panels display a quasar without detected Mg II absorption at $d = 52$ kpc. The *left* panels display the SDSS spectra of the foreground quasars. The *middle* panels display the SDSS spectra of the background quasars with the expected positions of the Mg II doublet members at the systemic redshift of the foreground quasar marked by vertical dashed lines. In both the left and middle panels, the flux and error arrays are shown in black histogram and dotted red line respectively. The zero-flux level is marked by a horizontal, black dashed line. The SDSS image of the fields around the quasars are shown on the *right* with the position of the foreground and background quasars labelled as $\mathrm{Q_f}$ and $\mathrm{Q_b}$ respectively. The purple line at the top left of each image is $5''$ in length.

and Prochaska et al. (2014). The sample from Bowen et al. (2006) contains four foreground quasars probed at $d = 26, 29, 47$, and 98 kpc all of which are detected in Mg II absorption with equivalent widths ranging from $W_{\rm r}(2796) = 0.4$ to 1.9 Å. We included quasars from Farina et al. (2013) and Farina et al. (2014) after converting their 2-σ detection limits to 3-σ, applying a uniform cut requiring sufficient signal in the background quasar spectrum to detect an absorption system of $W_{\rm r}(2796) > 0.3$ Å, and restricting the Mg II search window to $|\Delta v| < 1500$ km s^{-1}.

The quasar sample from Prochaska et al. (2014) spans a redshift range of $z = 1.8 - 3.8$, and consequently Mg II absorption constraints are not available with the existing optical spectra. Mg II absorption traces cool ($T \sim 10^4$ K) gas (Bergeron & Stasińska, 1986) with high H I column densities of $N({\rm H\,I}) \approx 10^{18} - 10^{22}$ (Rao et al., 2006). At $z \gtrsim 2$, C II λ1334 absorption can serve as an alternative tracer of such cool, high column density gas. Neutral magnesium and carbon share similar ionization potential and we therefore expect the ratio of Mg II to C II equivalent width to approximately follow the rest-frame wavelength ratios, $W_{\rm r}(2796)/W_{\rm r}(1334) = 2.09$ for saturated systems with line-widths dominated by non-thermal broadening. Empirically, low-redshift galaxies with constraints on both Mg II and C II equivalent widths from Werk et al. (2013) exhibit a mean ratio of $W_{\rm r}(2796)/W_{\rm r}(1334) = 1.7$. In order to compare the cool gas contents around high redshift quasars with the sample in this work, we adopted this mean ratio to convert from the C II equivalent widths reported in Prochaska et al. (2014) to expected Mg II equivalent widths (consistent with the conversion from Prochaska et al. (2014)). To maintain a uniform cut in absorption sensitivity, we restricted the quasar sample from Prochaska et al. (2014) to those with signal-to-noise in the background spectrum sufficient to detect a C II λ1334 absorption system of $W_{\rm r}(1334) > 0.18$ Å at 3-σ significance. This sensitivity corresponds to the $W_{\rm r}(2796) > 0.3$ Å sensitivity requirement adopted for the $z \approx 1$ samples with constraints on Mg II absorption.

5.3 Mg II absorption near quasars

With the quasar and absorption-line measurements described in Section 5.2 in hand, we characterize the Mg II absorption found around quasars as a function of projected distance, luminosity, and redshift in Section 5.3.1. In addition, we explore the kinematics of the absorption systems in Section 5.3.2 and discuss associated Mg II absorption systems found along the sightline to the foreground quasar itself in Section 5.3.3.

5.3.1 Dependence on projected distance, luminosity, & redshift

We characterize Mg II equivalent width as a function of projected distance in the left panel of Figure 5.3 and display the measurements from Bowen et al. (2006); Farina et al. (2013, 2014), and Prochaska et al. (2014) for comparison. The Mg II equivalent widths exhibit an anti-correlation with projected distance that is driven by a decrease in incidence at large projected distances. To verify the significance of this anti-correlation between equivalent width and projected distance, we perform a generalized Kendall-τ rank correlation test including the non-detections as upper limits (Isobe et al., 1986). The Kendall test finds an anti-correlation characterized by a coefficient of -0.3 with a high significance of $p \ll 1\%$[2]. The anti-correlation is driven primarily by a decrease in the incidence of absorption systems at $d \gtrsim 100$ kpc rather than by a decrease in the mean equivalent width of detections. Interestingly, strong absorption systems of $W_{\rm r}(2796) > 1.0$ Å are observed at $d > 100$ kpc, in stark contrast to L_* galaxies at $z < 1.5$ (Chen et al., 2010a; Lovegrove & Simcoe, 2011).

Using a sample of quasars probed in absorption by background quasar spectra placing constraints on C II absorption, Prochaska et al. (2014) found excess absorption for quasars at $z \approx 2.2$ compared to quasars probed in Mg II at $z \approx 1$ (Farina et al., 2013, 2014). Prochaska et al. (2014) interpreted this excess as redshift evolution in the properties of quasar host halos.

2. We note that the measurement uncertainties will tend to bias the correlation coefficient toward zero and perform this test to estimate the statistical significance of the anti-correlation within our sample rather than to measure the coefficient.

Figure 5.3: Mg II absorption equivalent width and covering fraction versus projected distance from the foreground quasar.

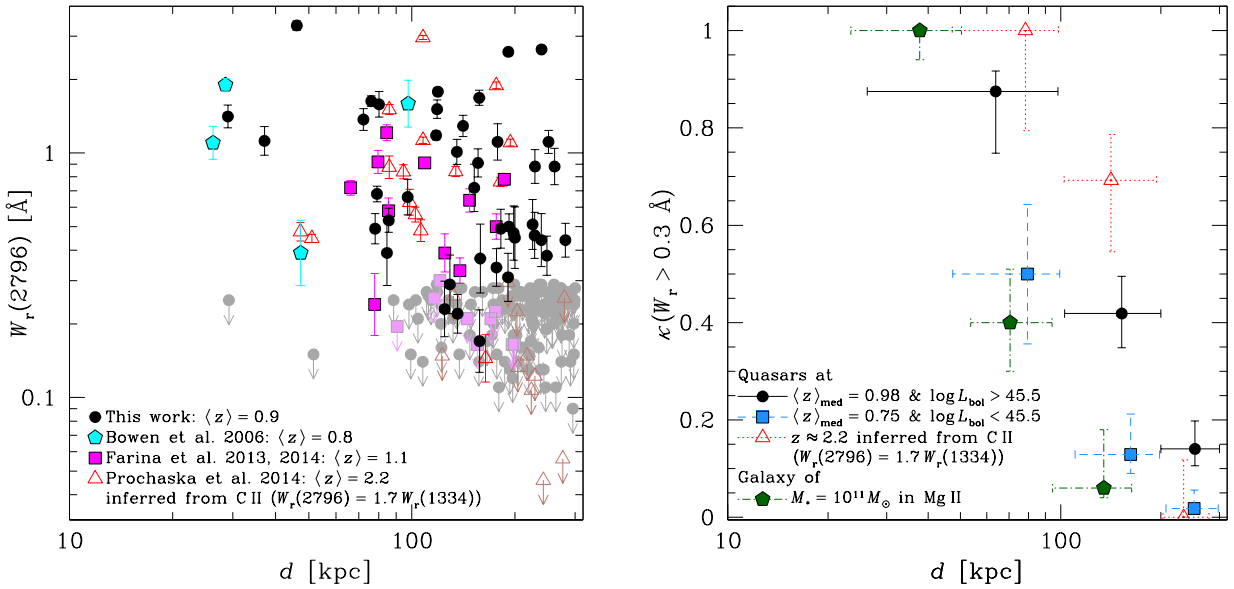

left: Rest-frame Mg II λ2796 equivalent width versus projected distance. Symbols and coloring are as in Figure 5.1. Non-detections are shown as 3-σ upper limits marked by downward arrows and lighter shading. *right*: Covering fraction for absorption systems with $W_r(2796) > 0.3$ Å as a function of projected distance for the quasars probed in Mg II with luminous quasars ($\log L_{bol}/\mathrm{erg\,s^{-1}} > 45.5$) in black solid line and low-luminosity quasars ($\log L_{bol}/\mathrm{erg\,s^{-1}} < 45.5$) in blue dashed line. For comparison, the covering fraction for luminous quasars at $z \approx 2.2$ based on the sample probed in C II from Prochaska et al. (2014) is shown in red dotted line. Finally, we also show the expected covering fraction for galaxies with stellar mass $\log M_*/M_\odot = 11$ in green dash-dot line. The vertical error bars mark 68% confidence intervals calculated from binomial statistics with a flat prior ($\kappa \in [0, 1]$) and the horizontal error bars mark the full range of projected distances contributing to each bin. The bins are chosen to span the range of $d = 0 - 300$ kpc in 100 kpc wide intervals. We note that the expected incidence of coincidental Mg II absorption systems unrelated to the quasars within the velocity search window is insignificant ($\kappa_{rand} = 0.01$) based on the Mg II $\partial N/\partial z \partial W_r$ measurement from Zhu & Ménard (2013). The SDSS quasars are drawn from a flux-limited survey and consequently, the luminous quasars occur at a higher median redshift of $\langle z \rangle_{med} = 0.98$ compared to $\langle z \rangle_{med} = 0.75$ for the low-luminosity quasars. The higher gas covering fractions observed for the luminous quasars could therefore be the result of luminosity-dependence, redshift evolution, or a combination of the two. The observed correlation between covering fraction and luminosity is isolated from the possible effects of redshift evolution in Figure 5.4.

However, the quasars in the $z \approx 2.2$ sample from Prochaska et al. (2014) are characterized by high luminosities (see left panel of Figure 5.1), and it is not clear that they form a representative sample for the entire quasar population. To investigate this possibility, we combine our SDSS quasars with those reported in the literature with Mg II constraints (Bowen et al., 2006; Farina et al., 2013, 2014) and divide the resulting combined Mg II sample at the median luminosity into luminous quasars of $\log L_{\rm bol}/{\rm erg\,s^{-1}} > 45.5$ and low-luminosity ones of $\log L_{\rm bol}/{\rm erg\,s^{-1}} < 45.5$. In doing so, we restrict the combined Mg II quasar sample to those with $z < 1.8$ where the sample follows the well defined redshift-luminosity trend seen in Figure 5.1. We note that this luminosity division also corresponds to the traditional division of AGN into quasars and Seyfert galaxies (e.g. Schmidt & Green, 1983).

Both the luminous and low-luminosity quasars exhibit decreasing covering fraction as a function of projected distance as shown in the right panel of Figure 5.3. In particular, the low-luminosity quasar covering fraction decreases from $\kappa_{\rm Mg\,II} = 0.50 \pm 0.14$ at $d < 100$ kpc to $\kappa_{\rm Mg\,II} = 0.13^{+0.08}_{-0.04}$ and $\kappa_{\rm Mg\,II} = 0.02^{+0.04}_{-0.01}$ at $d = 100 - 200$ and $200 - 300$ kpc respectively. The Mg II covering fractions for low-luminosity quasars are consistent within uncertainties with expectations for inactive galaxies with stellar masses $\log M_*/M_\odot \approx 11$ based on the covering fraction and stellar mass scaling relation measurements from Chen et al. (2010a) and Chen et al. (2010b)[3]. A stellar mass of $\log M_*/M_\odot \approx 11$ is chosen for this comparison because it is the expected stellar mass of galaxies with halo masses similar to quasar hosts (Shen et al., 2013b) based on the stellar-to-halo mass relation from Behroozi et al. (2013). On the other hand, the luminous quasars exhibit enhanced covering fraction that are a factor of ≈ 2 or more higher than those of the low-luminosity quasars over the full range of projected distances studied here with $\kappa_{\rm Mg\,II} = 0.88^{+0.04}_{-0.13}$ at $d < 100$ kpc, $\kappa_{\rm Mg\,II} = 0.42 \pm 0.07$ at $d = 100 - 200$, and $\kappa_{\rm Mg\,II} = 0.14^{+0.06}_{-0.03}$ at $d = 200 - 300$.

3. The galaxy sample from Chen et al. (2010a) is based on a sample of $L \approx L_*$ galaxies at $z \lesssim 0.2$, but the scaling relations in Chen et al. (2010b) remain valid at $z < 2$ (Lovegrove & Simcoe, 2011; Chen, 2012; Liang & Chen, 2014).

To verify the significance of the excess Mg II absorption around luminous quasars relative to low-luminosity ones over the full range of projected distances studied here, we also calculate the covering fraction at $d < 300$ kpc for the low-luminosity quasars and luminous quasars and find $\kappa_{\rm Mg\,II} = 0.10^{+0.04}_{-0.02}$ and $0.34^{+0.05}_{-0.04}$ respectively. In addition, we perform a logrank test (Feigelson & Nelson, 1985) comparing the distributions of the Mg II equivalent widths for the low-luminosity quasars and redshift weighted luminous quasars at $d < 300$ kpc. The test yields a logrank statistic of $L_n = 15.2 \pm 3.7$, which confirms that the luminous quasars exhibit excess Mg II absorption relative to low-luminosity quasars. The probability of measuring $L_n = 15.2$ or greater if the two quasar populations exhibit identical Mg II absorbing properties is $p \ll 1\%$.

While the low- and high-luminosity quasars exhibit distinct gas covering fractions, it is possible that the difference in gas covering fraction is the result of redshift evolution in quasar host halo gas properties. In particular, the SDSS quasar sample is drawn from a flux-limited survey, and consequently the luminous quasars in our sample occur at higher median redshift of $\langle z \rangle_{\rm med} = 0.98$ compared to $\langle z \rangle_{\rm med} = 0.75$ for the low-luminosity quasars as shown in Figure 5.1. The excess absorption observed around the luminous quasars could therefore be the result of luminosity dependence, redshift evolution, or a combination of the two. To isolate the luminosity dependence, we restrict the luminous quasar sample to $z < 1$ in order to match the median redshift of the luminous quasar sample to that of the low-luminosity quasars. The covering fraction for the luminous quasars at $z < 1$ and $d < 300$ kpc is $\kappa_{\rm Mg\,II} = 0.32^{+0.07}_{-0.05}$ compared to $\kappa_{\rm Mg\,II} = 0.10^{+0.04}_{-0.02}$ for the low-luminosity quasars. A logrank test comparing the Mg II equivalent width distribution of the low-luminosity quasars with that of the luminous quasar at $z < 1$ confirms this excess with a significance of $p \ll 1\%$. The comparison of the Mg II absorption incidence between the luminous and low-luminosity quasars with restricted redshift ranges indicates that the observed correlation between covering fraction and luminosity is not being driven by underlying redshift evolution.

The observed correlation between Mg II absorption covering fraction and quasar luminosity can explain a significant portion of the excess cool gas found for quasars at $z \approx 2.2$ relative to those at $z \approx 1$. Nevertheless, the covering fractions for the luminous quasars at $z \approx 1$ probed in Mg II at $d = 100 - 200$ kpc are somewhat lower than those of the $z \approx 2.2$ quasars probed in C II from Prochaska et al. (2014) ($\kappa = 0.69^{+0.09}_{-0.15}$). This possible difference between the $z \approx 1$ and $z \approx 2$ samples could be the result of additional correlation with luminosity, a difference in projected distance distribution between the $z \approx 1$ and $z \approx 2.2$ samples, or evolution in cool gas content of quasar host halos.

To differentiate these possibilities, we plot the covering fraction of Mg II absorption systems with $W_{\rm r}(2796) > 0.3$ Å at $d < 200$ kpc as a function of luminosity for the combined Mg II quasar sample after resampling to mimic the flatter projected distance distribution of the Prochaska et al. (2014) sample in the left panel of Figure 5.4. The resampling is accomplished by randomly resampling the quasars probed in Mg II without replacement to construct a maximal possible sample with the projected distance distribution mimicking that of Prochaska et al. (2014). The random resampling is repeated a large number of times to measure the mean covering fraction. Uncertainties in the mean covering fraction are calculated from binomial statistics with the sample size of the largest possible subsample with flat projected distance distribution.

The low-luminosity quasars ($\log \langle L_{\rm bol}/{\rm erg\,s^{-1}} \rangle = 45.2$) exhibit a mean covering fraction of $\kappa_{\rm Mg\,II} = 0.25^{+0.10}_{-0.06}$ while the luminous ones ($\log \langle L_{\rm bol}/{\rm erg\,s^{-1}} \rangle = 45.9$) exhibit a covering fraction of and $\kappa_{\rm Mg\,II} = 0.6^{+0.06}_{-0.07}$ at $d < 200$ kpc, indicating a strong correlation between quasar luminosity and the incidence of extended Mg II absorbing gas. A similar trend of increasing covering fraction with luminosity is observed when the sample is restricted to $z < 1$ (see the blue points in Figure 5.4). The trend of increasing covering fraction with luminosity found for the $z \approx 1$ quasars connects smoothly with the high covering fractions ($\kappa = 0.76^{+0.07}_{-0.13}$) found for high-luminosity quasars ($\log \langle L_{\rm bol}/{\rm erg\,s^{-1}} \rangle = 46.2$) at $z \approx 2.2$ from

Figure 5.4: Mg II covering fraction as a function of quasar luminosity and redshift.

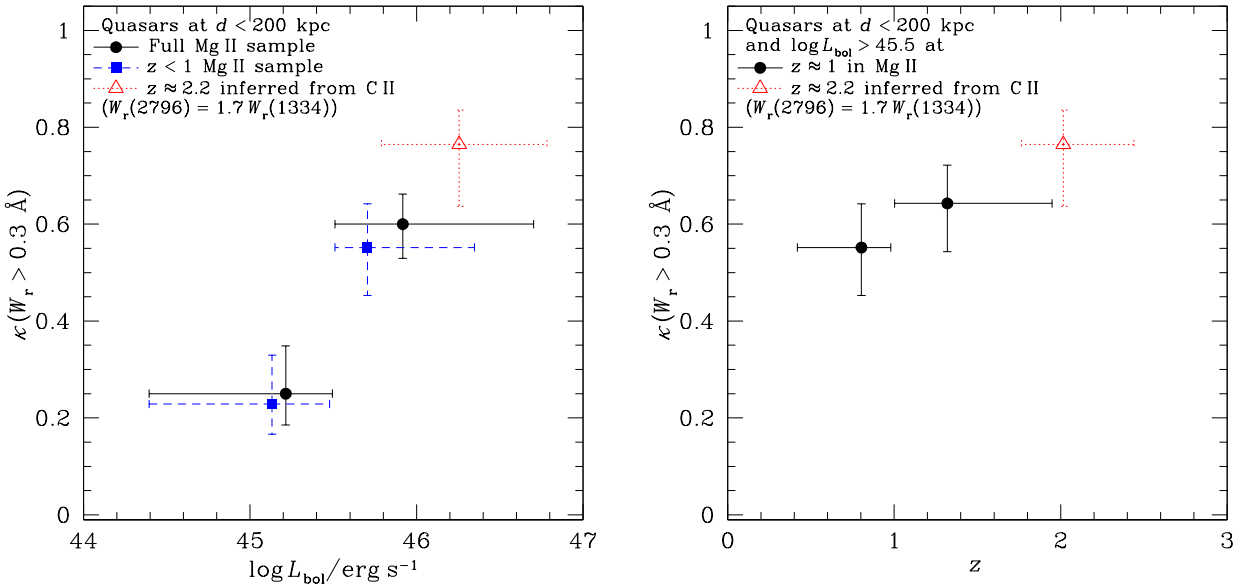

left: Covering fraction at $d < 200$ kpc of Mg II absorption systems of $W_{\rm r}(2796) > 0.3$ Å as a function bolometric luminosity of the foreground quasars. To isolate the correlation with luminosity from possible redshift evolution, we also show the covering fraction as a function of bolometric luminosity with the quasar sample restricted to $z < 1$ in blue. This redshift restriction is chosen so that the median redshift of the luminous quasars matches that of the low-luminosity quasars. *right*: Covering fraction at $d < 200$ for quasars of $\log\, L_{\rm bol}/{\rm erg\,s^{-1}} > 45.5$ as a function of redshift. In both panels, the vertical error bars mark 68% confidence intervals estimated from binomial statistics and the horizontal error bars mark the full range contributing to each bin. In both panels, the Mg II quasar sample is resampled to mimic the projected distance distribution of the $z \approx 2.2$ sample from Prochaska et al. (2014) (red).

Prochaska et al. (2014) (see the left panel of Figure 5.4). We note that in calculating the covering fraction for quasars from Prochaska et al. (2014), we restrict the sample to $z < 2.5$ where the Prochaska et al. (2014) sample closely follows the redshift-luminosity trend seen in the $z \approx 1$ samples (see the left panel of Figure 5.1).

With the correlation between Mg II absorption incidence and quasar luminosity in mind, we search for any additional dependence of Mg II absorption on redshift. To do so, we plot the covering fraction at $d < 200$ kpc of the luminous quasars as a function of redshift after resampling to mimic the projected distance distribution of the Prochaska et al. (2014) quasar sample in the right panel of Figure 5.4. At $z < 1$ and $z = 1 - 2$, the luminous quasars probed in Mg II exhibit covering fractions of $\kappa_{\rm Mg\,II} = 0.55^{+0.09}_{-0.10}$ and $0.64^{+0.08}_{-0.10}$ at $d < 200$ kpc, consistent with no evolution between $z < 1$ and $z = 1 - 2$. The corresponding covering fraction for the $z \approx 2.2$ sample from Prochaska et al. (2014) is $\kappa = 0.76 \pm 0.12$, consistent with the covering fractions found for the $z < 1$ quasars at the level of 1.3σ. The increase from $\kappa_{\rm Mg\,II} = 0.53^{+0.11}_{-0.12}$ at $z < 1$ to $\kappa = 0.76^{+0.07}_{-0.13}$ at $z \approx 2.2$ is suggestive, but a larger sample of quasars at $z \approx 2$ is required to investigate further. In addition, optical spectra of background sightlines toward quasars at $z < 2.5$ can provide constraints on Mg II absorption which would eliminate the additional systematic uncertainty in converting between Mg II and C II absorption equivalent widths.

5.3.2 Kinematics

To characterize the kinematics of the Mg II absorption systems around quasars, we plot histograms of the radial velocity differences between the quasars and Mg II systems in the left panel of Figure 5.5. The radial velocity histograms are characterized by a core that is consistent with the velocity spread found around galaxies ($\sigma \approx 150$ km s^{-1}; Chen et al., 2010a), but 29 out of 67 Mg II components (43%) are found at radial velocity differences with $|\Delta v| > 300$ km s^{-1} compared to 2 out of 47 galaxies (4%) in Chen et al. (2010a). Ten of 29

quasars with narrow-line redshifts and detected Mg II absorption are found to have Mg II absorption at $|\Delta v| = 300 - 1500$ km s^{-1} (34%) indicating that the majority of the large velocity differences are not the result of the uncertainties in broad-line based quasar redshifts (see the top left panel of Figure 5.5). Such large velocity differences are found among both high- and low-luminosity quasars, though the sample of low-luminosity quasars with Mg II absorption is small (see the bottom left panel of Figure 5.5).

In addition to large radial velocity differences, six quasars in the SDSS sample are found to have multiple, resolved Mg II absorption complexes spread over hundreds to thousands of km s^{-1} in the background quasar spectrum. The complex kinematics found for these six quasars are visualized in the right panel of Figure 5.5. The Mg II doublet members are separated by a wavelength difference that corresponds to $\Delta v = 770$ km s^{-1}, creating the potential for confusion between absorber kinematics and the weaker doublet member. To avoid this confusion in visualizing the systems of multiple Mg II absorption complexes, we fit the Mg II absorption using the VPFIT package and plot the data after dividing by the fit for the λ2803 doublet member. We note that each absorption "complex" in the SDSS spectra would likely be resolved into multiple components in high resolution spectra.

5.3.3 Narrow, associated absorption systems

A few percent of optically selected quasars exhibit narrow, "associated" absorption-line systems ($z_{\rm abs} \approx z_{\rm qso}$) along the sightline to the quasar itself (e.g. Weymann et al., 1979; Wild et al., 2008; Vanden Berk et al., 2008). Associated absorption-line systems could arise in gas associated with the quasar, the interstellar medium of the quasar host, or the interstellar/circum-galactic medium of neighboring galaxies, but the ionizing radiation from the quasar is expected to photoevaporate Mg II absorbing clouds out to distances of ≈ 1 Mpc along the quasar sightline (Hennawi & Prochaska, 2007; Wild et al., 2008). A recent comparison between quasars with narrow, associated Mg II absorption and a control sample

Figure 5.5: Kinematics of the Mg II absorbers identified near quasar hosts.

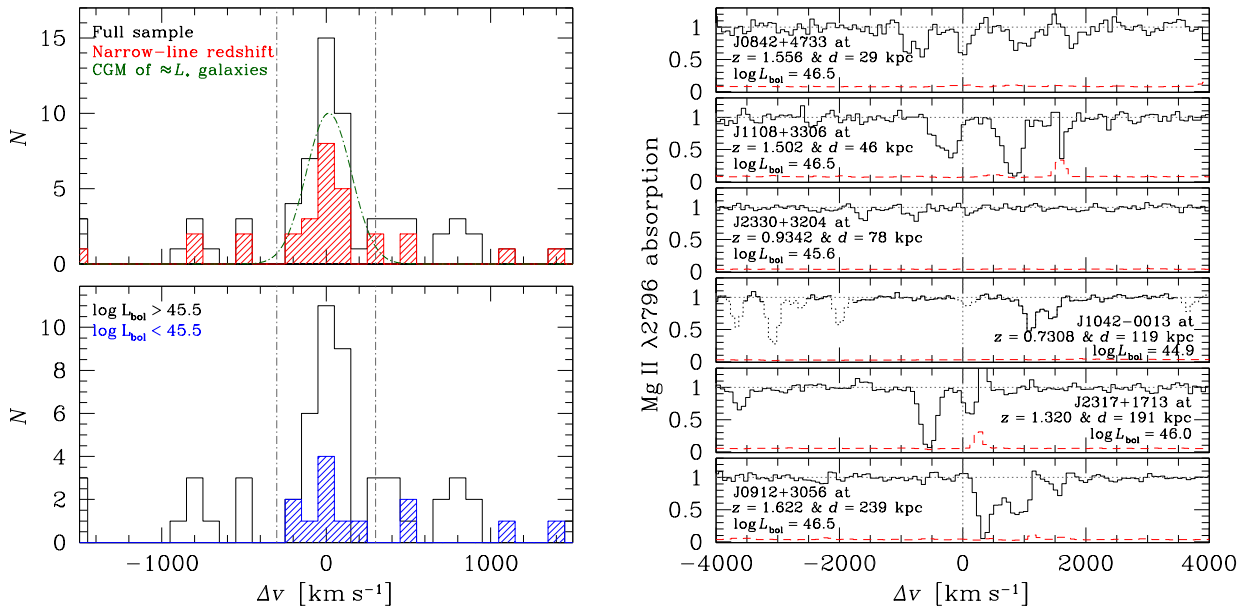

left: Histograms of the radial velocity differences between the quasar systemic redshifts and Mg II component redshifts at $\Delta v < 1500$ km s^{-1}. The *top* panel shows the full Mg II sample in black, quasars with narrow-line redshifts in shaded red, and the fit to galaxies from Chen et al. (2010a) in green dash-dot line. Vertical lines mark ± 300 km s^{-1}, the expected virial velocity of a typical quasar host halo at $z = 1.0$. The *bottom* panel shows the radial velocity histogram for the high- and low-luminosity quasars in black and blue filled histogram respectively. *right*: Kinematic structure seen in absorption toward six foreground quasars observed with resolved velocity structure in SDSS spectra of the background quasar. The panels are labelled with the foreground quasar name, redshift, projected distance, and bolometric luminosity. Quasar redshifts from narrow lines are shown to four decimal places and those from broad lines are shown to three. To prevent confusion between kinematic structure and the weaker Mg II doublet member, we model the Mg II doublet observed in the SDSS spectra and plot the data divided by the model for the λ2803 doublet member.

of redshift and i-band magnitude matched quasars without associated absorption found that quasars with associated Mg II absorption exhibit slightly enhanced dust extinction ($E(B-V) \approx 0.03$) and a $50-70\%$ enhancement in [O II] emission (Shen & Ménard, 2012; Khare et al., 2014).

A search within our foreground quasar sample identifies four luminous and six low-luminosity quasars with associated ($|\Delta v| < 1500$ km s^{-1}) narrow Mg II absorption systems along the foreground quasar sightline. Two of these four luminous quasars are found to have Mg II absorption systems detected in the background quasar spectra at $d = 150-300$ kpc, consistent with expectations from the general high-luminosity quasar sample. None of the six low-luminosity quasars with associated absorption systems are found to have Mg II systems in the background quasar spectra at $d = 180-275$ kpc, also consistent with expectations from the general, low-luminosity quasar sample. Though the sample of quasars with associated Mg II absorption and constraints on transverse Mg II absorption from background quasars is small, these results suggest that the large-scale halo gas contents of quasars with associated absorption are not radically different from those found in the general quasar population.

5.4 Discussion

Using a sample of 195 quasars at $z \approx 1$ with constraints on Mg II absorption from background quasars at projected distances of $d < 300$ kpc from the SDSS, we characterized the cool gas contents of quasar host halos as a function of projected distance, quasar luminosity, and redshift. Our main findings are the following:

1. Luminous quasars of $\log L_{\rm bol}/{\rm erg\,s^{-1}} > 45.5$ exhibit enhanced Mg II absorption relative to low-luminosity quasars and inactive galaxies of similar mass at projected distances of $d < 300$ kpc.

2. The absorbing gas near quasars exhibits complex kinematics with $30-40\%$ of components

found at $|\Delta v| = 300 - 1500$ km s^{-1} from the quasar systemic redshift. and

3. The incidence of cool gas absorption around luminous quasars does not evolve strongly with redshift between $z \approx 1$ and $z \approx 2.2$.

In this section, we discuss the possible origins of the extended Mg II absorbing gas near quasars, correlation with luminosity, and complex kinematics. Finally, we briefly consider possible avenues of future research.

Galaxies of $L \approx L_*$ at $z \lesssim 0.2$ exhibit high Mg II covering fractions out to a gaseous radius that is observed to scale with stellar mass according to $R_{\rm Mg\,II} \propto M_*^{0.28}$ (Chen et al., 2010b) and comparisons with CGM absorption at higher redshift suggest that the low-redshift scaling relations remain valid at $z \lesssim 2$ (e.g. Lovegrove & Simcoe, 2011; Chen, 2012; Liang & Chen, 2014). Since quasars are thought to reside in massive galaxies of $L \gtrsim L_*$, previous studies (e.g. Farina et al., 2014; Prochaska et al., 2014) suggested that the high incidence of C II and Mg II absorption observed at impact parameters of $d = 100 - 200$ kpc from quasars are the result of mass scaling of the CGM. In this scenario, the absorption traces the "normal" halo gas of inactive galaxies with masses similar to quasar hosts. However, the expected Mg II absorption incidence from inactive galaxies with masses similar to quasar hosts ($\log M_*/M_\odot \approx 11$ based on the clustering measurement from Shen et al. (2013b) and stellar-to-halo mass relation from Behroozi et al. (2013)) is significantly lower than the covering fraction observed around luminous quasars (see the right panel of Figure 5.3). Moreover, quasar luminosity and host halo mass are only weakly (if at all) correlated (e.g. Shen et al., 2013b) so the observed correlation between quasar luminosity and Mg II absorption cannot be explained by mass scaling.

Finally, the large velocity differences observed between the quasar and absorber redshifts ($30 - 40\%$ of absorption at $|\Delta v| = 300 - 1500$ km s^{-1}) and complex kinematics seen in some sightlines (see Figure 5.5) are inconsistent with gas gravitationally bound to a halo with the mean mass of quasar hosts ($\log M_h/M_\odot = 12.8$; Shen et al., 2013b) which have inferred halo

virial velocities of ≈ 300 km s^{-1}. However, clustering measurements constrain the mean mass of quasar hosts, not the overall host halo mass distribution (see discussion in White et al., 2012), and the large fraction of absorption at $|\Delta v| = 300 - 1500$ km s^{-1} could be explained if $\approx 30 - 40\%$ of quasars reside in halos with larger masses. To evaluate this possibility, we measure the radial velocity differences observed between quasars with narrow-line redshifts and Mg II absorption systems, correct for line-of-sight projection by multiplying by $\sqrt{3}$, and find a population averaged velocity dispersion of 1000 km s^{-1} between the quasars and absorbing gas. The halo mass corresponding to a virial velocity of 1000 km s^{-1} is $\log M_h/M_\odot = 14.4$. Such massive halos are three orders-of-magnitude less abundant than those of $\log M_h/M_\odot = 12.8$ (Tinker et al., 2008) making it unlikely that a substantial fraction of quasars reside in such massive systems. Direct confirmation of this conclusion will require redshift surveys to characterize the environments of quasars with constraints on halo gas properties from background sightlines.

The high Mg II gas covering fractions, correlation with quasar luminosity, and kinematics can be explained if the Mg II absorbing gas is the result of:

1. the CGM of neighboring galaxies at $\gtrsim 1$ Mpc scales but at projected distances of $d \lesssim 300$ kpc,

2. feedback from luminous quasars, or

3. debris from the galaxy interactions and mergers thought to trigger luminous quasars.

In the following subsections, we discuss each of these possibilities in turn.

5.4.1 Mg II absorption from galaxies neighboring the quasar host

Large scale quasar-quasar (e.g. White et al., 2012) and quasar-galaxy (e.g. Shen et al., 2013b) clustering measurements indicate that quasars reside in massive halos that trace over-dense regions of the Universe. Consequently, the CGM of galaxies in neighboring halos at

Figure 5.6: Possible contribution to the Mg II covering fraction from nearby galaxies.

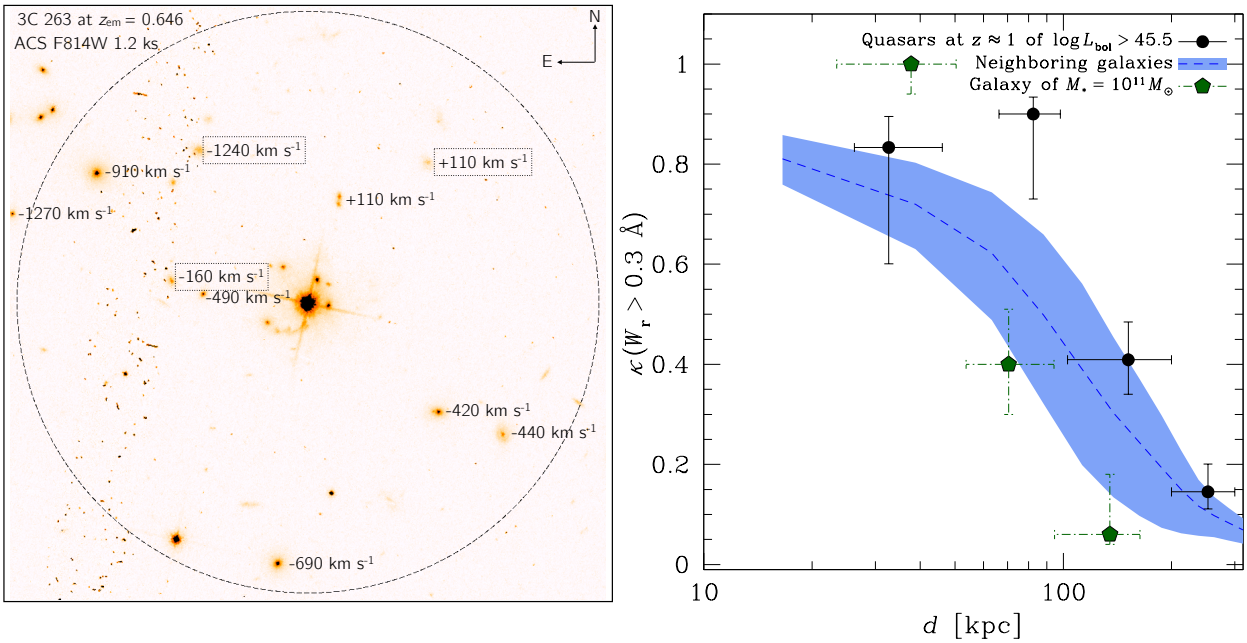

left: The galaxy environments near a luminous quasar (3C 263 at $z = 0.646$) with available deep redshift surveys targeting galaxies of $r_{\rm AB} < 23$. Galaxies with secure redshifts and within $|\Delta v| < 1500$ km s^{-1} of the quasar redshift are labelled with Δv and star-forming galaxies are highlighted with dotted black outline. A dashed black circle of 150 kpc in radius centered on the quasar is shown for scale. The image is a stack of two 600 second exposures from the Advanced Camera for Surveys on the *Hubble Space Telescope* (PI: Mulchaey; PID: 13024) taken with the F814W filter with offsets between exposures to fill the gap between the ACS detectors. Cosmic ray removal is not possible in regions with coverage in only one exposure and these regions are visible as 5″ wide stripes with high cosmic ray contamination. *right*: Covering fraction for absorption systems with $W_{\rm r}(2796) > 0.3$ Å as a function of projected distance for luminous quasars (black solid line) compared to expectations from a galaxy of $\log M_*/M_\odot = 11$ (green dash-dot line), and expected incidence due to neighbors of the quasar host (blue dashed line). The mean expected incidence due to neighbors is based on four UV-bright quasars with available deep galaxy redshift surveys and the light blue band represents the estimated uncertainty in the mean. We note, however, that with such a small sample size, uncertainty due to sampling are both large and poorly quantified.

distances of $\gtrsim 1$ Mpc from the quasar but projected distances of $\lesssim 300$ kpc could contribute to the Mg II absorption covering fractions and explain the large radial velocity differences often observed between the quasar and absorber redshifts.

To evaluate the expected covering fraction from neighboring galaxies, we use four UV-bright quasars at $z = 0.3 - 0.6$ with highly complete redshift surveys of galaxies of $r_{\rm AB} < 23$ from Chen & Mulchaey (2009); Johnson et al. (2013); and Johnson et al (in prep). These surveys reveal the presence of galaxies with redshifts within $|\Delta v| < 1500$ km s^{-1} of the quasar redshift at projected distances of $d \lesssim 300$ kpc that could potentially contribute to the Mg II absorption observed around quasars at similar projected distances (see left panel of Figure 5.6). We estimate the expected contribution to the covering fraction observed around quasars from these neighboring galaxies using the covering fraction and luminosity scaling measurements from Chen et al. (2010a). In this calculation, we do not include galaxies more luminous than $M_B = -22.2$ since such luminous galaxies exhibit reduced incidence of Mg II absorption compared to galaxies of $L \approx L_*$ (Gauthier et al., 2010).

The expected Mg II covering fractions from neighboring galaxies can explain a significant portion of the Mg II absorption observed around quasars at $d < 300$ kpc (see right panel of Figure 5.6). Moreover, neighboring galaxies are often at $|\Delta v| \approx 300 - 1500$ km s^{-1} from the quasar, potentially explaining the kinematics observed in Mg II absorption. We note, however, that the sample of quasars with available deep redshift surveys is small (4 quasars) and, consequently, the estimated covering fraction from neighboring galaxies suffers from significant and poorly quantified sampling uncertainties.

If a substantial portion of the Mg II absorption observed around quasars traces the CGM of neighboring galaxies in other host halos at Mpc scales, then the correlation between quasar luminosity and Mg II absorption would imply a correlation between quasar luminosity and quasar-galaxy clustering. However, studies of quasar-quasar and quasar-galaxy clustering found no correlation between quasar luminosity and clustering on Mpc scales (e.g. Croom

et al., 2005; Myers et al., 2007; White et al., 2012; Shen et al., 2013b). In addition, recent observations of projected quasar-photometric galaxy pair counts find no evidence for a correlation with quasar luminosity (Padmanabhan et al., 2009; Zhang et al., 2013; Scott et al., 2015). We note that some studies of quasar-photometric galaxy pair counts find excess counts at $d < 300$ kpc for luminous quasars (Serber et al., 2006), but this excess is attributed to galaxies in the quasar host halo and the excess is not observed on larger scales.

The lack of correlation between quasar luminosity and clustering are in tension with expectations from the observed correlation between Mg II covering fraction and quasar luminosity if a substantial portion of the absorption arises in neighboring halos on Mpc scales, in apparent contradiction with the covering fraction estimate shown in the right panel of Figure 5.6. This discrepancy can be explained by the proximity effect in which the UV light from the quasar photo-evaporates the cool halo gas of galaxies out to Mpc scales. Indeed, galaxies at $\Delta v < 3000$ km s^{-1} from quasars exhibit significantly reduced cool halo gas content compared to the general galaxy population (e.g. Pascarelle et al., 2001).

5.4.2 Mg II absorption due to quasar feedback

Radio-loud, lobe-dominated quasars (class FRII; Fanaroff & Riley, 1974) are known to drive powerful outflows at both high and low redshift (e.g. Nesvadba et al., 2008; Fu & Stockton, 2009). However, only a small fraction quasars are radio-loud and lobe-dominated (e.g. Urry & Padovani, 1995; Ivezić et al., 2002), so radio-mode feedback alone cannot be responsible for the observed correlation between Mg II absorption and luminosity.

Recent observations of spatially resolved [O III] emission around luminous, radio-quiet, obscured (Type 2) quasars revealed the presence of surprisingly spherical gaseous nebulae that are both spatially (≈ 30 kpc) and kinematically (≈ 1000 km s^{-1}) extended (Greene et al., 2012; Liu et al., 2013a,b). Similar structures are observed in [O III] emission around luminous, radio-quiet, unobscured (Type 1) quasars (Liu et al., 2014) like those studied

in this work. These observations are most naturally explained as fast outflows with wide opening angles driven by radio-quiet quasars (also see Zakamska & Greene, 2014).

The quasar driven outflows observed in emission on scales of ≈ 30 kpc may naturally explain the high incidence and complex kinematics of Mg II absorption around quasars if the outflows persist to larger distances but with gas densities that are too low to be observed in collisionally excited emission lines. An outflow with velocity $v_{\rm out} = 1000\ {\rm km\,s^{-1}}$ at 15 kpc from the host galaxy nucleus could reach distances of ≈ 100 (200) kpc in $\approx 10^8$ (2×10^8) years assuming that the outflow decelerates due to the gravitational potential of the host halo. The timescales required to reach $100 - 200$ kpc from the host halo are comparable to the high end of quasar lifetime estimates (10^8 years; Martini, 2004). Moreover, these fast, quasar driven outflows are observed to be effective at luminosities of $\log\, L_{\rm bol}/{\rm erg\,s^{-1}} \gtrsim 45.5$ (e.g. Veilleux et al., 2013; Zakamska & Greene, 2014) and could therefore explain the observed correlation between extended Mg II absorption and quasar luminosity.

In the outflow scenario, the Mg II absorbing gas represents cool clumps entrained in a hotter outflowing medium (e.g. Costa et al., 2015). Indeed, observations of outflows from both quasars and ultra-luminous infrared galaxies reveal copious quantities of highly ionized gas traced by C IV and O VI absorption (Arav et al., 2013; Martin et al., 2015). However, in the one foreground quasar with published high resolution background quasar spectroscopy, cool gas traced by C II absorption is found spread over 700 ${\rm km\,s^{-1}}$ but little absorption from more highly ionized species is found (Prochaska & Hennawi, 2009). The low ionization state of the gas in this system ($N({\rm C\,II})/N({\rm C\,IV}) > 10$) is inconsistent with expectations from cool gas entrained in a quasar driven outflow, suggesting that quasar driven outflows alone cannot universally explain the high absorption covering fractions and complex kinematics observed around quasars.

Alternatively, the gas kinematics and ionization state can be understood if feedback from luminous quasars drives the pre-existing halo gas to large velocities, far in excess of the sound

speed. Such fast bulk motions could lead to an enhanced fraction of gas with sufficiently high densities to cool and produce Mg II absorbing clumps. In this way, feedback from the quasar could convert halo gas generally observed in high ionization states at projected distances less than the virial radius (e.g. O VI; Chen & Mulchaey, 2009; Tumlinson et al., 2011; Johnson et al., 2015b) to lower-ionization states observable in Mg II absorption. Feedback from luminous quasars therefore represents a viable scenario for explaining the cool halo gas properties around quasar hosts including kinematics, correlation with luminosity, and enhanced covering fractions relative to inactive galaxies of similar masses.

5.4.3 Mg II absorption from tidal debris

Luminous quasars are thought to be fueled by gas supplied during galaxy mergers while the gas required to fuel less luminous AGN can be supplied by more secular processes (e.g. Hopkins & Hernquist, 2009). The high incidence of absorbing gas around quasars and correlation with luminosity can be explained if the gas traces debris from the galaxy mergers that can trigger luminous AGN. Tidal debris can obtain velocities that exceed the escape velocity of the host halo (e.g. Toomre & Toomre, 1972), possibly explaining the kinematics observed in absorption. The low ionization state ($N(\mathrm{C\,II})/N(\mathrm{C\,IV}) > 10$) observed in the one available quasar with high resolution background spectroscopy (Prochaska & Hennawi, 2009) is consistent with the ionization state found in Magellanic Stream sightlines with similar H I column densities (Fox et al., 2014). Finally, deep 21-cm observations of the M81/M82 group reveal that relic gas from galaxy interactions can extend to cover large areas, possibly explaining the high Mg II covering fractions observed out to scales of $\lesssim 200$ kpc around luminous quasars. Tidal debris therefore represents a viable possibility for explaining observed Mg II absorption properties around quasars. We note, however, that it is not clear that tidal debris alone can explain the large fraction ($30 - 40\%$) of Mg II absorption components found at radial velocities of $|\Delta v| > 300$ km s^{-1}.

5.4.4 Future prospects

The high covering fraction of Mg II absorption observed around quasars, correlation with luminosity, and complex kinematics observed in our SDSS sample are not consistent with the absorption expected from inactive galaxies with masses similar to typical quasar hosts. In addition, clustering measurements imply that high- and low-luminosity quasars are hosted by halos of similar mean masses (Shen et al., 2013b) implying that the correlation between cool gas covering fraction and quasar luminosity is not the result of simple mass scaling of the circum-galactic medium. Together, these observations imply that a substantial portion of the Mg II absorbing gas does not originate in the "normal" halo gas of the quasar hosts. The high covering fraction, correlation with luminosity, and complex kinematics can be explained if the absorbing gas is the result of: (1) the CGM of neighboring galaxies on Mpc scales, (2) feedback from luminous quasars, or (3) relics from the interactions thought to trigger luminous quasars. The first of these scenarios is in tension with the lack of correlation between quasar luminosity and clustering on Mpc scales (e.g. Serber et al., 2006; Shen et al., 2013b). The remaining two scenarios make distinct predictions that can be tested with additional observations.

If a substantial fraction of the Mg II absorbing gas is the result of quasar feedback, then we expect the cool gas absorption to be correlated with the presence of extended outflows observed in [O III] emission (e.g. Greene et al., 2012).

If, on the other hand, the Mg II absorbing gas arises in relics from the mergers that are thought to trigger luminous quasars, then the absorption would be correlated with the presence of disturbed host morphologies and nearby tidal remnants. At $z \approx 1$, searching for such interaction signatures requires the high resolution imaging capabilities of HST.

CHAPTER 6

CURRENT SURVEY STATUS AND FUTURE WORK

In the previous chapters of this thesis, I presented results from on-going surveys to constrain the relationship between diffuse baryons observed as quasar absorption-line systems and galaxies. The thesis began in Chapter 2 with a detailed analysis of the galactic environments of quasar absorption systems in the field of PKS 0405−123 finding that O VI absorption systems in the sightline primarily trace the extended gaseous halos of star-forming galaxies and low-mass galaxy groups. Next, in Chapter 3, I presented the discovery of a surprisingly transparent sightline at small projected distance from a close pair of interacting galaxies suggesting that galaxy interactions can significantly deplete cool gas reservoirs through heating or stripping. Next, in Chapter 4 I examined the extent of H I and O VI absorbing gas around galaxies as a function of environment and found that O VI absorption but not H I is more extended around galaxies with nearby neighbors. This contrast suggests that galaxy environment plays a role in distributing heavy-element enriched gas beyond the halos of individual galaxies. Finally, in Chapter 5 I presented a survey of the relationship between cool halo gas traced by Mg II absorption and quasar activity finding a strong correlation between quasar luminosity and cool gas content at large distances as well as extreme kinematics in the absorbing gas. The luminosity dependence and kinematics of the cool gas around quasar hosts can potentially be explained by quasar feedback and debris from the galaxy interactions thought to trigger luminous quasars. The results presented in Chapters 2−5 highlight the potentially important role of galaxy environment in the relationship between galaxies and extended halo gas reservoirs. In this chapter, I summarize the current survey status, preview on-going work, and motivate future studies with the existing dataset.

6.1 Current survey status

Since the installation of COS on HST in 2009, the COS GTO team as well as investigators awarded GO proposals have built a large archive of over 200 quasars with moderate resolution UV spectra covering $\approx 1150 - 1750$ Å from the COS G130M and G160M gratings. These spectra have enabled quasar absorption line surveys to characterize the baryon content of the low redshift Universe with unprecedented precision (e.g. Danforth et al., 2016). However, to quote Michael Rauch in his talk at a conference held at the NRAO in Oct. 2015, "quasar absorption line surveys provide exquisite statistical constraints that are forever in search of physical meaning".

To provide some additional insights into the nature of baryons probed by quasar absorption surveys and their relationship with galaxies in particular, we have been conducting deep and highly complete galaxy redshift surveys in fields with high quality COS spectra of intermediate redshift quasars using the IMACS and LDSS3 spectrographs on the Magellan telescopes. The quasar sightlines were selected to be at $z_{\rm QSO} \gtrsim 0.5$, observable from Magellan (dec $\lesssim +15$ deg), and with high S/N COS G130M and G160M spectra available in the HST archive. Quasars at higher redshifts were prioritized due to the larger redshift path length probed by their COS spectra and quasars with higher S/N COS spectra were prioritized to maximize the sensitivity of the available absorption-line constraints. In total, we obtained galaxy redshift survey data for nine quasar fields which represent the majority of intermediate redshift quasars with high S/N COS spectra that are observable from the southern hemisphere (see Figure 6.1). The COS quasar spectra and corresponding galaxy survey data are summarized in Table 6.1.

6.1.1 Galaxy survey data

In order to target galaxies for spectroscopic follow-up and provide information on the galaxy spectral energy distributions, we obtained deep multi–band images covering a field

Table 6.1: Summary of the galaxy and quasar absorption survey

	Quasar sightline					Galaxy survey			
Field name	R.A. (J2000)	Dec. (J2000)	z_{QSO}	COS $\langle S/N \rangle$	COS PI/PID	imaging (camera-bands)	# masks (IMACS)	# masks (LDSS3)	# redshifts ($\theta < 10'$)
HE 0226−4110[a]	02:28:15.1	−40:28:15.1	0.493	25	Green/11541	IMACS-BRI & ACS-F814W	5	2	429
PKS 0232−04	02:35:07.4	−04:02:05.7	1.437	13	Tripp/11741	IMACS-gri & ACS-F814W[c]	12	1	1014
PKS 0405−123[b]	04:07:48.4	−12:11:36.7	0.573	50	Noil/11508 & Green/11541	IMACS-gri & ACS-F814W	9	1	442
PKS 0637−752	06:35:46.5	−75:16:16.8	0.653	20	Howk/11692	IMACS-gri & WFPC2-F702W	9	0	489
HE 1003+0149	10:05:35.2	+01:34:45.7	1.076	11	Morris/12264	IMACS-gri & ACS-F184W[d]	6	0	462
PG 1216+069[a]	12:19:20.9	+06:38:39	0.331	17	Green/12025	IMACS-BRI & WFPC2-F702W	5	0	326
LBQS 1435-0134	14:37:48.3	−01:47:10.8	1.312	25	Tripp/11741	IMACS-gri & ACS-F814W	15	0	926
PG 1522+101	15:24:24.5	+09:58:29.1	1.326	17	Tripp/11741	IMACS-gri & ACS-F814W[d]	13	1	589
1ES 1553+113	15:55:43.0	+11:11:24.3	> 0.43	20	Green/12025	MOSAIC1.1-gri & ACS-F814W	8	0	491

Notes
[a] Galaxy catalog published in Chen & Mulchaey (2009)
[a] Galaxy catalog published in Johnson et al. (2013)
[c] HST image scheduled but not yet acquired (PI/PID: Lehner/14269)
[d] HST image acquired but not yet public (PI/PID: Lehner/14269)

Figure 6.1: Galaxy survey sightlines in the context of the COS archive

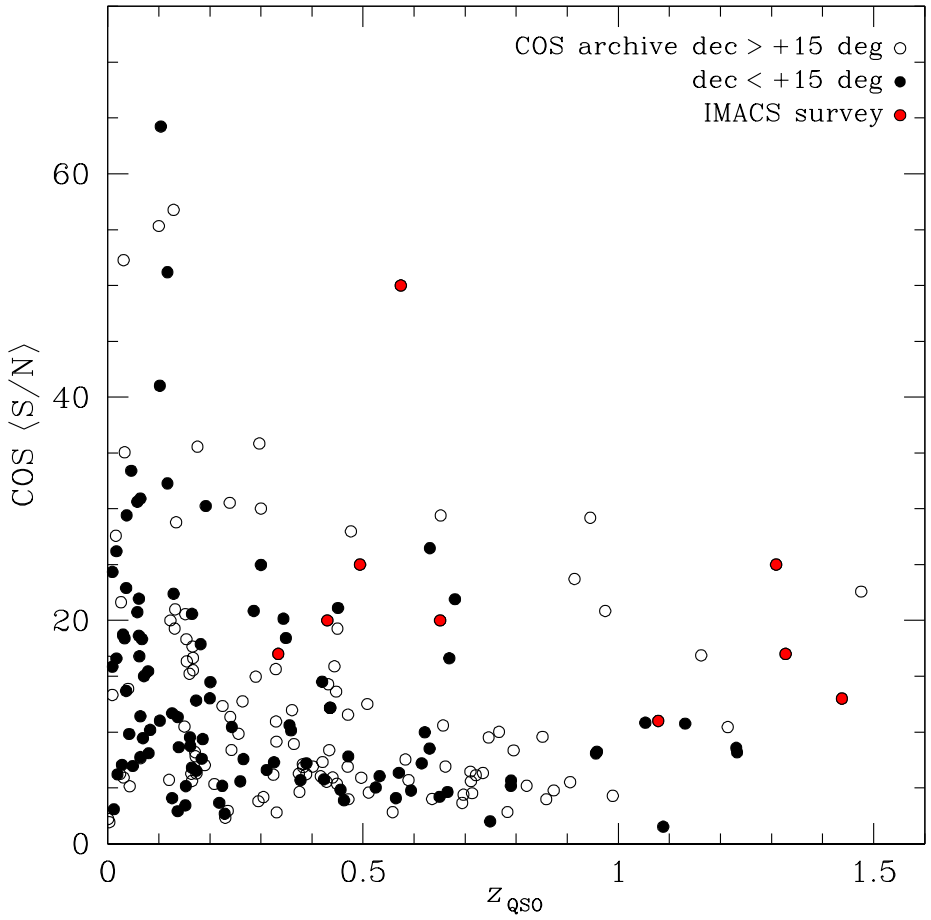

COS mean S/N versus quasar redshift for sightlines with archival G130M and G160M spectra. Quasars at dec $> +15$ deg are shown in open black circles while those observable from Magellan at dec $< +15$ are shown in filled black circles. Quasar fields in our Magellan galaxy survey are highlighted in red.

Figure 6.2: Completeness levels for faint galaxies in the three most complete survey fields.

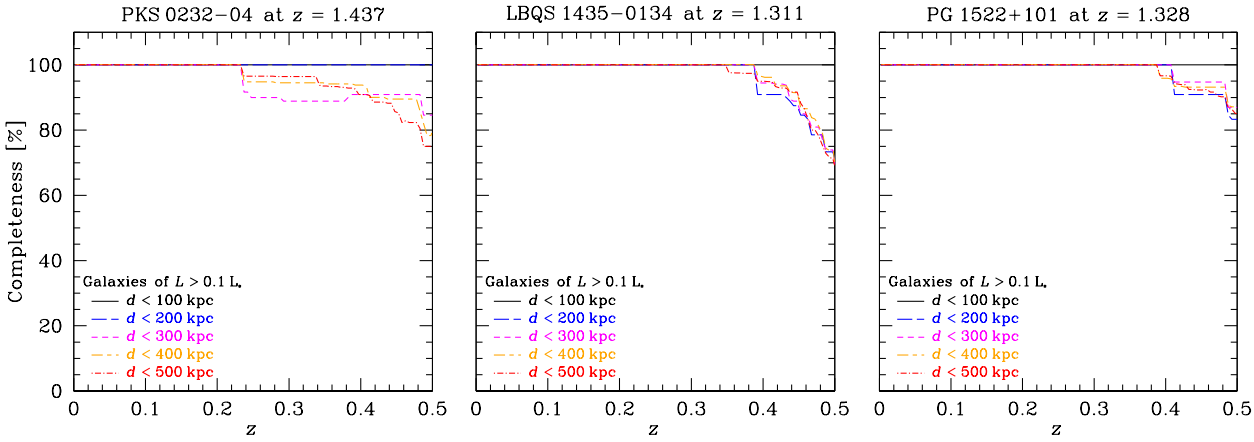

Estimated completeness as a function of redshift for galaxies of $L > 0.1\,L*$ in the fields of PKS 0232−04 (left), LBQS 1435-0134 (middle), PG 1522+101 (right). Completeness levels at projected distances of $d < 100, 200, 300, 400$, and 500 kpc are shown with line-style indicated in the figure legends.

of at least $20'$ in diameter with the IMACS f2 camera in imaging mode or the MOSAIC 1.1 camera (Sawyer et al., 2010) on the Mayall 4-m telescope at the Kitt Peak Observatory (summarized in Table 6.1). The images were all obtained under photometric conditions with atmospheric seeing ranging from $0.6''$ to $1.1''$. The images from each detector were reduced with standard techniques (bias subtraction and flat fielding), and astrometry solutions were calculated using the CCMAP routine in IRAF with SDSS stars as references when available and the 2MASS point sources (Cutri et al., 2003) as references for fields outside of the SDSS footprint. The images from each CCD were then combined into a single median mosaic stack using SWARP (Bertin et al., 2002). The stacked images were flux calibrated using unsaturated stars in SDSS fields and standard star fields from Landolt (1992). Finally, objects were detected and galaxy photometry measured using Source Extractor (Bertin & Arnouts, 1996) isophotal magnitudes with the r-band as the detection image. The resulting photometric galaxy catalogs are highly complete for galaxies of $AB(r) < 25$.

With the images described above in hand, we targeted galaxies of $AB(r) < 23.5$ mag (corresponding to $\approx 0.1\,L_*$ at $z = 0.5$) for multi-object spectroscopic follow-up and prioritized

the galaxies closest to the quasar sightline with the goal of obtaining $\gtrsim 80\%$ completeness levels for faint galaxies at $\theta \lesssim 1'$ (corresponding to ≈ 350 kpc at $z = 0.5$). The galaxy spectroscopy was obtained using the $200l$ (200 lines per mm) grating on IMACS and the VPH-all grating on LDSS3 which provide an observed wavelength coverage of $4000 - 9500$ Å with a FWHM resolution of ≈ 10 Å. The spectroscopic observations generally consisted of between $2\times$ and 6×1800 second exposures (depending on observing conditions) with flat and HeNeAr wavelength calibrations obtained every hour. The multi-object spectra were reduced with the COSMOS reduction pipeline and redshifts were measured both by cross-correlation with SDSS galaxy templates and a PCA fitting technique as discussed in Chapter 2. Based on a comparison between galaxy redshifts from our survey that were also measured by the SDSS, we estimate a 1-σ redshift uncertainty of ≈ 60 km s^{-1}.

The resulting redshift survey includes between 300 and 1000 galaxies per field and achieves completeness levels of $60 - 100\%$ for galaxies or $AB(r) < 23$ at $\theta < 1'$ except in the fields of PG 1216+069 and 1ES 1553+113 which were given lower priority due to the lower redshifts of the background quasars. Particularly high completeness levels were obtained in the fields of PKS 0232−04, LBQS 1435−0134, and PG 1522+101 (see Figure 6.2) which were given increased priority due to the high quasar redshift and high S/N of the quasar spectra. In addition the surveys cover a wide area of $\theta < 10'$ with completeness levels of $\gtrsim 50\%$ for galaxies of $r < 22$ to enable characterizations of galaxy environment and future clustering measurements on Mpc scales.

6.1.2 Quasar absorption-line analysis

While the galaxy data were being acquired, we analyzed the COS quasar spectra in order to characterize the IGM and CGM absorption lines observed in each sightline. The individual COS exposures were retrieved in reduced form from the Mikulski Archive for HST. Though the latest COS calibration pipeline from STScI (CALCOS version 3.1.7) includes significantly

improved wavelength calibrations compared to previous versions, residual calibration errors remain. In particular, zero-point errors likely due to faulty target acquisition can be as high as ≈ 50 km s^{-1} and higher order errors of ≈ 10 km s^{-1} in the wavelength calibration are common. In order to perform a near optimal coadd of exposures in the presence of such large wavelength calibration errors, we measured wavelength calibration corrections for each exposure relative to a reference exposure by cross-correlating every suitable absorption feature observed in the individual exposures. We then fit low-order polynomials to the wavelength corrections and registered the exposures to a common wavelength solution before creating a final stacked spectrum. Because COS uses a photon counting detector with no read noise, we calculated the flux error using the gross total counts and Poisson statistics enabling accurate error estimates in the low count regime.

While the calibration of the wavelength grid of each exposure to a common reference enables a near optimal coadd, the wavelength calibration of the reference exposure is still subject to the large zero-point and higher order calibration errors often seen in COS data. To improve upon this wavelength calibration, we fit a low-order polynomial to the offsets between measured centroids of unsaturated, low ionization state Milky Way ISM lines and expected laboratory wavelengths of these transitions. We then subtracted the low-order fit from the COS wavelength array so that the Milky Way ISM lines are aligned at $z = 0$ and then shifted the spectrum to match the redshift of Milky Way Ca II H & K absorption features measured in ground-based optical spectra of the quasars. By comparing the resulting COS spectra of HE 0226−4110 and PKS 0405−123 with archival STIS spectra of these sightlines we estimate that the corrected wavelength calibration results in reduced wavelength calibration uncertainties of $\lesssim 4$ km s^{-1}. While these residual wavelength calibration errors are not ideal, they are sufficiently small compared to the COS FWHM resolution (≈ 17 km s^{-1}) to enable confident line identification.

With the stacked COS spectra, we proceeded to identify absorption features visually in

the following steps. First, we identified Milky Way interstellar absorption features commonly found in quasar absorption spectra. Next, we identified strong H I absorption features and associated Lyman series and metal ion lines by starting at the highest wavelength end of the COS spectrum and proceeding to lower wavelengths. For PKS 0232−04, LBQS 1435−0134, and PG 1522+101 the line identification process was aided by COS G185M and G225M spectra as well as STIS E230M spectra from the COSBaH survey (PI/PID: Tripp/13846). These near-UV spectra covering $1800 - 3100$ Å enabled confident identification of strong H I absorption systems at $z = 0.75 - z_{\rm QSO}$. After identifying strong H I absorption systems and associated metal ion transitions, we attempted to identify the remaining unidentified lines by searching for doublet pairs of C IV, N V, O VI, and Ne VIII. Any remaining lines at > 1215 Å are assumed to be H I Lyα. Through this process, we identified between 100 and 300 absorption features per sightline for a total of 1800 identified features in all nine sightlines.

6.2 An updated view of the galactic environments of O VI absorption systems

Among quasar absorption systems, the O VI doublet has received particular attention as possible tracer of the WHIM, galactic outflows, highly ionized galaxy halo gas, and the intra-group medium. In Chapter 2 we examined the galactic environments of strong H I absorption systems (N(H I) $> 10^{13.6}$ cm^{-2}) with detected O VI absorption relative to a control sample of strong H I absorption systems with no detected O VI or other metal lines in the field of PKS 0405−123. This comparison provides insights into the conditions that distinguish O VI absorption systems from those without such highly ionized metal enriched gas. We found that the strong H I absorbers with O VI primarily trace the extended highly ionized halo gas around galaxies and groups of galaxies and that the galaxy surface density and flux around these H I + O VI absorbers is enhanced at $d < 500$ kpc from the quasar sightline relative to strong H I systems without detected metal lines. However, with the small sample of seven

Figure 6.3: The galactic environments of strong H I absorption systems with detected O VI absorption compared to strong H I absorption systems without detected metal lines.

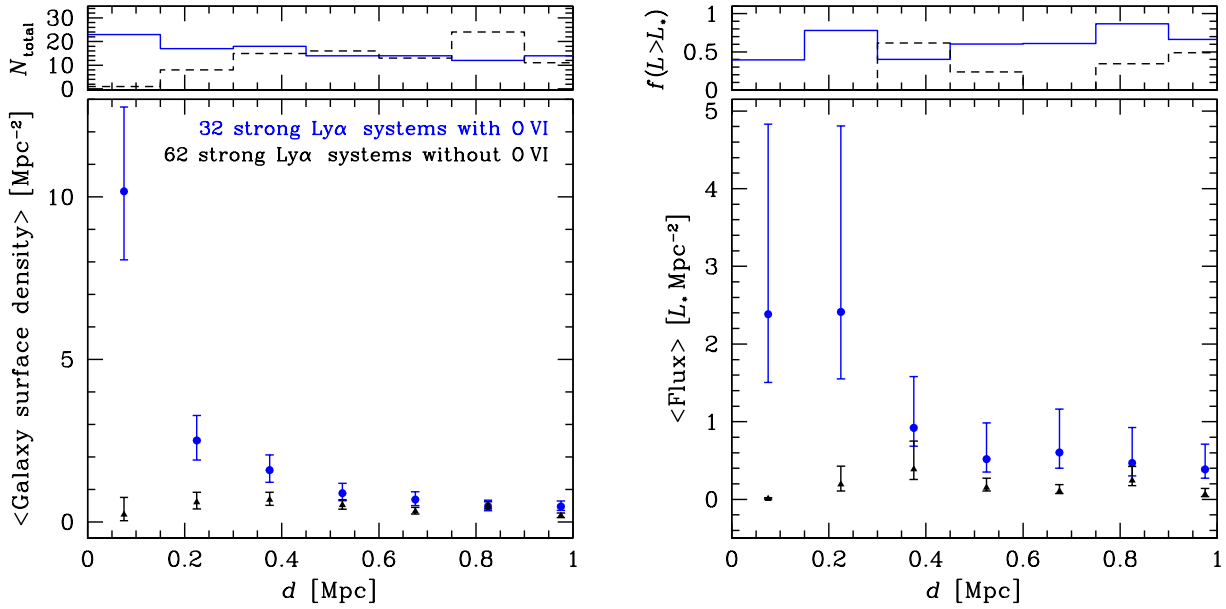

Mean total surface density (left bottom panel) and flux (right bottom panel) of galaxies around strong ($N(\mathrm{H\,I}) > 10^{13.6}\,\mathrm{cm}^{-2}$) H I absorption systems with detected O VI (blue circles) and those with no detected O VI or other metal transitions (black triangles) at $z < 0.5$. The surface density and flux are calculated in projected distance annuli with $d_{\mathrm{outer}} - d_{\mathrm{inner}} = 150$ kpc. The errors bars mark 1σ uncertainties calculated from Poisson statistics. The strong H I + O VI absorption systems exhibit enhanced galaxy surface density and flux at $d \lesssim 500$ kpc relative to strong H I absorption systems without metal lines which exhibit flat radial profiles. For reference, the total number of galaxies contributing to the mean of each annulus is shown in the small panel on the top left and the fraction of the total mean galaxy flux contributed from galaxies of $L > L_*$ is shown in the small panel on the top right.

O VI absorption systems in the sightline of PKS 0405−123, these conclusions were subject to large uncertainties. Here, we return to this question with a significantly increased sample of seven sightlines with COS quasar spectra complemented with deep Magellan galaxy survey data with completeness levels of $> 60\%$ for galaxies of $r < 23$ at angular distances less than $1'$ from the quasar sightline (the sightlines are PKS 0232−04, HE 0226−4110, PKS 0405−123, PKS 0637−752, HE 1003+0149, LBQS 1435−0134, and PG 1522+101). In total, these seven sightlines contain 32 strong H I absorption systems with O VI and 62 strong H I systems with no detected metal absorption lines.

First, we examine the mean radial galaxy surface density profile around strong H I absorption systems with and without O VI in the left panel of Figure 6.3. Motivated by clustering measurements form Chen et al. (2005), we associate galaxies with absorption systems if they fall within a radial velocity of ± 300 km s^{-1} of the absorber redshift. The strong H I systems with no O VI exhibit a relatively flat radial galaxy surface density profile from $d < 250$ kpc to 1 Mpc. In contrast, while the systems with O VI absorption exhibit similar galaxy surface density at $d > 500$ kpc, they exhibit a $\approx 2-3\times$ excess at $d = 250-500$ kpc that further increases to a $\approx 10\times$ excess at $d < 250$ kpc. Though the uncertainties are higher, the mean radial total galaxy flux profiles in annuli around strong H I systems with O VI absorption also exhibit a significant excess relative to those without O VI at $d < 500$ kpc as shown in the right panel of Figure 6.3. These results indicate that the key distinguishing feature in determining whether such strong H I absorption systems produce O VI is proximity to nearby galaxies.

To gain additional insights, we now consider the galactic environments of O VI in more detail. Of the 32 strong H I + O VI absorption systems in the seven sightlines at $z < 0.5$, 28 (88^{+4}_{-8}%) are found to have at least one galaxy within $d = 500$ kpc, 27 (84^{+4}_{-8}%) have at least one star-forming galaxy within 500 kpc, and 16 (47^{+9}_{-8}%) have more than one galaxy identified at $d < 500$ kpc. In contrast, among the strong H I absorption systems with no detected O VI or other metal-line absorption, only 18 of 62 (29^{+6}_{-5}%) have one or more galaxy at $d < 500$ kpc, 16 (26^{+6}_{-5}%) have one or more star-forming galaxy at $d < 500$ kpc, and 8 (13^{+5}_{-3}%) have two or more galaxies detected at $d < 500$ kpc. Moreover, the median distance to the nearest detected galaxy is 130 kpc for the O VI absorbing strong H I systems and 870 kpc for strong H I system with no O VI. These findings confirm the conclusion Chapter 2 that O VI absorption systems primarily trace the extended halos of gas-rich galaxies and groups.

6.3 Future work: the galaxy−gas two-point correlation function

The finding of at least one emission-line galaxy in the vicinity of 84% of the O VI absorption in the seven high completeness fields presented in the previous subsection suggests that O VI absorption systems largely occur in the halos of the intermediate luminosity ($L \approx 0.1 - 1\,L_*$) galaxies that dominate the star-forming galaxy population in magnitude limited surveys. In a CDM universe more massive systems are expected to exhibit stronger spatial clustering compared to less massive ones (e.g. Mo & White, 2002), and observational galaxy surveys have established that early-type galaxies are more strongly clustered than late-type galaxies (e.g. Madgwick et al., 2003). Consequently, the galaxy−absorber two-point projected spatial correlation function represents a key statistic that can provide additional insights into the origins of quasar absorption systems.

Chen et al. (2005) presented a pilot study of the galaxy−gas cross-correlation function for H I Lyα absorption systems at $z < 0.5$ in the field of PKS 0405−123 based on quasar absorption survey data from STIS and galaxy survey data from the WFCCD multi-object spectrograph on the 2.5-m DuPont telescope at the Las Campanas Observatory. They found strong H I Lyα absorption systems (with $N(\mathrm{H\,I}) > 10^{13.6}\,\mathrm{cm}^{-2}$ including those with observed O VI or other metal ion transitions) are not clustered spatially or in velocity space with early-type galaxies. In contrast, the strong H I absorption systems were found to cluster with late-type galaxies with amplitude comparable to the late-type galaxy auto-correlation function indicating that strong H I absorption systems and late-type galaxies trace similar dark matter halo populations. Chen & Mulchaey (2009) confirmed this result with significantly deeper galaxy survey data and two additional sightlines, and in addition, found that O VI absorbers (which represent a subset of the strong Lyα systems) exhibit the same clustering behavior as the strong H I absorbers. Subsequent galaxy−gas clustering measurements have confirmed the enhanced clustering of strong Lyα and O VI absorption around late-type galaxies in two-dimensional clustering measurements, however these findings do not always persist when the

two dimensional clustering measurements are collapsed in velocity to measure the projected spatial cross-correlation function (e.g. Tejos et al., 2014; Finn et al., 2016). This puzzling apparent discrepancy necessitates further study.

The combined quasar absorption and galaxy survey data of nine sightlines presented in this thesis and summarized in Table 6.1 offers a unique opportunity to study galaxy−gas clustering over a redshift pathlength of $z(\mathrm{O\,VI}) = 4.4$ with deep galaxy survey data. These sightlines combined represent a four-fold increase in redshift pathlength over the previous surveys with deep galaxy data enabling a more precise upcoming study of galaxy−gas clustering as a function of galaxy type as well as absorption properties.

REFERENCES

Adelberger, K. L., Steidel, C. C., Shapley, A. E., & Pettini, M. 2003, ApJ, 584, 45

Agertz, O., & Kravtsov, A. V. 2015, ApJ, 804, 18

Agertz, O., Teyssier, R., & Moore, B. 2011, MNRAS, 410, 1391

Ahn, C. P., Alexandroff, R., Allende Prieto, C., et al. 2014, ApJS, 211, 17

—. 2012, ApJS, 203, 21

Alam, S., Albareti, F. D., Allende Prieto, C., et al. 2015, ArXiv e-prints

Allende Prieto, C., Lambert, D. L., & Asplund, M. 2001, ApJL, 556, L63

Antonucci, R. 1993, ARAA, 31, 473

Arav, N., Borguet, B., Chamberlain, C., Edmonds, D., & Danforth, C. 2013, MNRAS, 436, 3286

Bahcall, J. N., & Salpeter, E. E. 1966, ApJ, 144, 847

Bahcall, J. N., & Spitzer, Jr., L. 1969, ApJL, 156, L63

Bahcall, J. N., Bergeron, J., Boksenberg, A., et al. 1993, ApJS, 87, 1

Balogh, M. L., Navarro, J. F., & Morris, S. L. 2000, ApJ, 540, 113

Barnes, J. E. 1989, Nature, 338, 123

Behroozi, P. S., Wechsler, R. H., & Conroy, C. 2013, ApJ, 770, 57

Bell, E. F., Wolf, C., Meisenheimer, K., et al. 2004, ApJ, 608, 752

Benson, A. J., Bower, R. G., Frenk, C. S., et al. 2003, ApJ, 599, 38

Bergeron, J., & Boissé, P. 1991, AAP, 243, 344

Bergeron, J., & Stasińska, G. 1986, AAP, 169, 1

Bernardi, M., Meert, A., Sheth, R. K., et al. 2013, MNRAS, 436, 697

Bertin, E., & Arnouts, S. 1996, AAPS, 117, 393

Bertin, E., Mellier, Y., Radovich, M., et al. 2002, in Astronomical Society of the Pacific Conference Series, Vol. 281, Astronomical Data Analysis Software and Systems XI, ed. D. A. Bohlender, D. Durand, & T. H. Handley, 228

Blanton, M. R., & Roweis, S. 2007, AJ, 133, 734

Blanton, M. R., Hogg, D. W., Bahcall, N. A., et al. 2003, ApJ, 592, 819

Boksenberg, A., Danziger, I. J., Fosbury, R. A. E., & Goss, W. M. 1980, ApJL, 242, L145

Bolton, A. S., Schlegel, D. J., Aubourg, É., et al. 2012, AJ, 144, 144

Bordoloi, R., Lilly, S. J., Knobel, C., et al. 2011, ApJ, 743, 10

Bordoloi, R., Tumlinson, J., Werk, J. K., et al. 2014, ApJ, 796, 136

Boroson, T. 2005, AJ, 130, 381

Borthakur, S., Heckman, T., Strickland, D., Wild, V., & Schiminovich, D. 2013, ApJ, 768, 18

Bowen, D. V., Blades, J. C., & Pettini, M. 1995, ApJ, 448, 634

Bowen, D. V., Pettini, M., & Blades, J. C. 2002, ApJ, 580, 169

Bowen, D. V., Hennawi, J. F., Ménard, B., et al. 2006, ApJL, 645, L105

Bruzual, G., & Charlot, S. 2003, MNRAS, 344, 1000

Bruzual, G. R., & Charlot, S., eds. 2010, IAU Symposium, Vol. 262, Stellar Populations - Planning for the Next Decade

Bryan, G. L., & Norman, M. L. 1998, ApJ, 495, 80

Burbidge, E. M., Lynds, C. R., & Burbidge, G. R. 1966, ApJ, 144, 447

Burles, S., Nollett, K. M., & Turner, M. S. 2001, Physical Reviews D, 63, 063512

Burles, S., & Tytler, D. 1996, ApJ, 460, 584

Carswell, R. F., & Webb, J. K. 2014, VPFIT: Voigt profile fitting program, Astrophysics Source Code Library

Carswell, R. F., Webb, J. K., Baldwin, J. A., & Atwood, B. 1987, ApJ, 319, 709

Casali, M., Adamson, A., Alves de Oliveira, C., & et al.. 2007, AAP, 467, 777

Catinella, B., Schiminovich, D., Cortese, L., et al. 2013, MNRAS

Cen, R. 2012, ApJ, 753, 17

—. 2013, ApJ, 770, 139

Cen, R., & Ostriker, J. P. 1999, ApJ, 514, 1

Chabrier, G. 2003, PASP, 115, 763

Charlot, S., & Fall, S. M. 2000, ApJ, 539, 718

Chen, H.-W. 2012, MNRAS, 427, 1238

Chen, H.-W., Helsby, J. E., Gauthier, J.-R., et al. 2010a, ApJ, 714, 1521

Chen, H.-W., Lanzetta, K. M., & Webb, J. K. 2001, ApJ, 556, 158

Chen, H.-W., Lanzetta, K. M., Webb, J. K., & Barcons, X. 1998, ApJ, 498, 77

—. 2001, ApJ, 559, 654

Chen, H.-W., & Mulchaey, J. S. 2009, ApJ, 701, 1219

Chen, H.-W., & Prochaska, J. X. 2000, ApJL, 543, L9

Chen, H.-W., Prochaska, J. X., Weiner, B. J., Mulchaey, J. S., & Williger, G. M. 2005, ApJL, 629, L25

Chen, H.-W., Wild, V., Tinker, J. L., et al. 2010b, ApJL, 724, L176

Churchill, C. W., Steidel, C. C., & Vogt, S. S. 1996, ApJ, 471, 164

Cid Fernandes, R., Stasińska, G., Mateus, A., & Vale Asari, N. 2011, MNRAS, 413, 1687

Coil, A. L., Blanton, M. R., Burles, S. M., et al. 2011, ApJ, 741, 8

Cole, S. 1991, ApJ, 367, 45

Coleman, G. D., Wu, C.-C., & Weedman, D. W. 1980, ApJS, 43, 393

Conroy, C., van Dokkum, P. G., & Kravtsov, A. 2015, ApJ, 803, 77

Conroy, C., & Wechsler, R. H. 2009, ApJ, 696, 620

Costa, T., Sijacki, D., & Haehnelt, M. G. 2015, MNRAS, 448, L30

Cox, T. J., Dutta, S. N., Di Matteo, T., et al. 2006, ApJ, 650, 791

Croom, S. M., Boyle, B. J., Shanks, T., et al. 2005, MNRAS, 356, 415

Cutri, R. M., Skrutskie, M. F., van Dyk, S., et al. 2003, 2MASS All Sky Catalog of point sources.

Danforth, C. W., & Shull, J. M. 2008, ApJ, 679, 194

Danforth, C. W., Tilton, E. M., Shull, J. M., et al. 2014, ArXiv e-prints, 1402.2655

Danforth, C. W., Keeney, B. A., Tilton, E. M., et al. 2016, ApJ, 817, 111

Davé, R., Oppenheimer, B. D., & Finlator, K. 2011, MNRAS, 415, 11

Davé, R., Oppenheimer, B. D., Katz, N., Kollmeier, J. A., & Weinberg, D. H. 2010, MNRAS, 408, 2051

Davé, R., Cen, R., Ostriker, J. P., et al. 2001, ApJ, 552, 473

de Vaucouleurs, G. 1961, ApJS, 5, 233

Dekel, A., & Birnboim, Y. 2006, MNRAS, 368, 2

Dekel, A., & Silk, J. 1986, ApJ, 303, 39

Dekel, A., Birnboim, Y., Engel, G., et al. 2009, Nature, 457, 451

Di Matteo, T., Springel, V., & Hernquist, L. 2005, Nature, 433, 604

Dicke, R. H., Peebles, P. J. E., Roll, P. G., & Wilkinson, D. T. 1965, ApJ, 142, 414

Dressler, A. 1980, ApJ, 236, 351

Dressler, A., Bigelow, B., Hare, T., et al. 2011, PASP, 123, 288

Ebeling, H., Stephenson, L. N., & Edge, A. C. 2014, ApJL, 781, L40

Eisenstein, D. J., Weinberg, D. H., Agol, E., et al. 2011, AJ, 142, 72

Ellingson, E., & Yee, H. K. C. 1994, ApJS, 92, 33

Faber, S. M., Willmer, C. N. A., Wolf, C., & et al.. 2007, ApJ, 665, 265

Fabian, A. C. 2012, ARAA, 50, 455

Fanaroff, B. L., & Riley, J. M. 1974, MNRAS, 167, 31P

Farina, E. P., Falomo, R., Decarli, R., Treves, A., & Kotilainen, J. K. 2013, MNRAS, 429, 1267

Farina, E. P., Falomo, R., Scarpa, R., et al. 2014, MNRAS, 441, 886

Faucher-Giguère, C.-A., Hopkins, P. F., Kereš, D., et al. 2015, MNRAS, 449, 987

Feigelson, E. D., & Nelson, P. I. 1985, ApJ, 293, 192

Ferland, G. J., Korista, K. T., Verner, D. A., et al. 1998, PASP, 110, 761

Ferland, G. J., Porter, R. L., van Hoof, P. A. M., et al. 2013, RMXAA, 49, 137

Finn, C. W., Morris, S. L., Tejos, N., et al. 2016, MNRAS, 460, 590

Ford, A. B., Oppenheimer, B. D., Davé, R., et al. 2013, MNRAS, 432, 89

Ford, A. B., Werk, J. K., Davé, R., et al. 2016, MNRAS, 459, 1745

Fox, A. J., Wakker, B. P., Barger, K. A., et al. 2014, ApJ, 787, 147

Fu, H., & Stockton, A. 2009, ApJ, 690, 953

Fukugita, M. 2004, in IAU Symposium, Vol. 220, Dark Matter in Galaxies, ed. S. Ryder, D. Pisano, M. Walker, & K. Freeman, 227

Fukugita, M., Hogan, C. J., & Peebles, P. J. E. 1998, ApJ, 503, 518

Fukugita, M., & Peebles, P. J. E. 2004, ApJ, 616, 643

Fumagalli, M., Hennawi, J. F., Prochaska, J. X., et al. 2014, ApJ, 780, 74

Gabor, J. M., & Davé, R. 2012, MNRAS, 427, 1816

Gaskell, C. M. 1982, ApJ, 263, 79

Gauthier, J.-R. 2013, MNRAS, 432, 1444

Gauthier, J.-R., Chen, H.-W., & Tinker, J. L. 2010, ApJ, 716, 1263

Gehrels, N. 1986, ApJ, 303, 336

Geller, M. J., & Huchra, J. P. 1989, Science, 246, 897

Genel, S., Genzel, R., Bouché, N., et al. 2008, ApJ, 688, 789

Ghavamian, P., Aloisi, A., Lennon, D., et al. 2009, Preliminary Characterization of the Post-Launch Line Spread Function of COS, Tech. rep.

Gnat, O., Sternberg, A., & McKee, C. F. 2010, ApJ, 718, 1315

Green, J. C., Froning, C. S., Osterman, S., et al. 2012, ApJ, 744, 60

Greene, J. E., Zakamska, N. L., & Smith, P. S. 2012, ApJ, 746, 86

Greenstein, J. L., & Schmidt, M. 1967, ApJL, 148, L13

Grossi, M., di Serego Alighieri, S., Giovanardi, C., et al. 2009, AAP, 498, 407

Gunn, J. E., & Gott, III, J. R. 1972, ApJ, 176, 1

Haardt, F., & Madau, P. 2012, ApJ, 746, 125

Hambly, N. C., Collins, R. S., Cross, N. J. G., & et al.. 2008, MNRAS, 384, 637

Heckman, T. M., Lehnert, M. D., Strickland, D. K., & Armus, L. 2000, ApJS, 129, 493

Hennawi, J. F., & Prochaska, J. X. 2007, ApJ, 655, 735

—. 2013, ApJ, 766, 58

Hennawi, J. F., Prochaska, J. X., Burles, S., et al. 2006, ApJ, 651, 61

Hewett, P. C., Warren, S. J., Leggett, S. K., & Hodgkin, S. T. 2006, MNRAS, 367, 454

Hewett, P. C., & Wild, V. 2010, MNRAS, 405, 2302

Hodgkin, S. T., Irwin, M. J., Hewett, P. C., & Warren, S. J. 2009, MNRAS, 394, 675

Hopkins, P. F., & Hernquist, L. 2009, ApJ, 694, 599

Hopkins, P. F., Kereš, D., Oñorbe, J., et al. 2014, MNRAS, 445, 581

Howk, J. C., Ribaudo, J. S., Lehner, N., Prochaska, J. X., & Chen, H.-W. 2009, MNRAS, 396, 1875

Hubble, E. P. 1936, Realm of the Nebulae

Hummels, C. B., Bryan, G. L., Smith, B. D., & Turk, M. J. 2013, MNRAS, 430, 1548

Isobe, T., Feigelson, E. D., & Nelson, P. I. 1986, ApJ, 306, 490

Ivezić, Ž., Menou, K., Knapp, G. R., et al. 2002, AJ, 124, 2364

Jenkins, E. B., & Meloy, D. A. 1974, ApJL, 193, L121

Johnson, S. D., Chen, H.-W., & Mulchaey, J. S. 2013, MNRAS, 434, 1765

—. 2015a, MNRAS, 452, 2553

—. 2015b, MNRAS, 449, 3263

Johnson, S. D., Chen, H.-W., Mulchaey, J. S., et al. 2014, MNRAS, 438, 3039

Kang, H., Ryu, D., Cen, R., & Song, D. 2005, ApJ, 620, 21

Katz, N., & Gunn, J. E. 1991, ApJ, 377, 365

Kenney, J. D. P., van Gorkom, J. H., & Vollmer, B. 2004, AJ, 127, 3361

Kennicutt, R. C., & Evans, N. J. 2012, ARAA, 50, 531

Kereš, D., Katz, N., Davé, R., Fardal, M., & Weinberg, D. H. 2009, MNRAS, 396, 2332

Kewley, L. J., Dopita, M. A., Sutherland, R. S., Heisler, C. A., & Trevena, J. 2001, ApJ, 556, 121

Kewley, L. J., Groves, B., Kauffmann, G., & Heckman, T. 2006, MNRAS, 372, 961

Keyes, C. D., Koratkar, A. P., Dahlem, M., et al. 1995, Faint Object Spectrograph Instrument Handbook v. 6.0

Khare, P., Berk Daniel, V., Rahmani, H., & York, D. G. 2014, ApJ, 794, 66

Koester, B. P., McKay, T. A., Annis, J., et al. 2007, ApJ, 660, 239

Kravtsov, A., Vikhlinin, A., & Meshscheryakov, A. 2014, ArXiv e-prints

Kravtsov, A. V., & Borgani, S. 2012, ARAA, 50, 353

Landolt, A. U. 1992, AJ, 104, 372

Lanzetta, K. M., Bowen, D. V., Tytler, D., & Webb, J. K. 1995, ApJ, 442, 538

Larson, R. B., Tinsley, B. M., & Caldwell, C. N. 1980, ApJ, 237, 692

Lawrence, A., Warren, S. J., Almaini, O., & et al.. 2007, MNRAS, 379, 1599

Le Fèvre, O., Saisse, M., Mancini, D., et al. 2003, in Society of Photo-Optical Instrumentation Engineers (SPIE) Conference Series, Vol. 4841, Society of Photo-Optical Instrumentation Engineers (SPIE) Conference Series, ed. M. Iye & A. F. M. Moorwood, 1670–1681

Lehner, N., Savage, B. D., Richter, P., et al. 2007, ApJ, 658, 680

Lehner, N., Howk, J. C., Tripp, T. M., et al. 2013, ApJ, 770, 138

Li, Y., & Bryan, G. L. 2014, ApJ, 789, 54

Liang, C. J., & Chen, H.-W. 2014, MNRAS, 445, 2061

Liang, C. J., Kravtsov, A. V., & Agertz, O. 2016, MNRAS, 458, 1164

Liu, G., Zakamska, N. L., & Greene, J. E. 2014, MNRAS, 442, 1303

Liu, G., Zakamska, N. L., Greene, J. E., Nesvadba, N. P. H., & Liu, X. 2013a, MNRAS, 430, 2327

—. 2013b, MNRAS, 436, 2576

Lopez, S., Barrientos, L. F., Lira, P., et al. 2008, ApJ, 679, 1144

Loveday, J., Norberg, P., Baldry, I. K., et al. 2012, MNRAS, 420, 1239

Lovegrove, E., & Simcoe, R. A. 2011, ApJ, 740, 30

Madgwick, D. S., Hawkins, E., Lahav, O., et al. 2003, MNRAS, 344, 847

Maller, A. H., Berlind, A. A., Blanton, M. R., & Hogg, D. W. 2009, ApJ, 691, 394

Maller, A. H., & Bullock, J. S. 2004, MNRAS, 355, 694

Martin, C. L., Dijkstra, M., Henry, A., et al. 2015, ApJ, 803, 6

Martini, P. 2004, Coevolution of Black Holes and Galaxies, 169

Mathes, N. L., Churchill, C. W., Kacprzak, G. G., et al. 2014, ApJ, 792, 128

Mathews, W. G., & Baker, J. C. 1971, ApJ, 170, 241

McConnachie, A. W., Patton, D. R., Ellison, S. L., & Simard, L. 2009, MNRAS, 395, 255

Meiksin, A., Bolton, J. S., & Tittley, E. R. 2015, ArXiv e-prints

Meiring, J. D., Tripp, T. M., Prochaska, J. X., et al. 2011, ApJ, 732, 35

Mo, H. J., & White, S. D. M. 2002, MNRAS, 336, 112

Montero-Dorta, A. D., & Prada, F. 2009, MNRAS, 399, 1106

Moore, B., Katz, N., Lake, G., Dressler, A., & Oemler, A. 1996, Nature, 379, 613

Moore, B., Lake, G., & Katz, N. 1998, ApJ, 495, 139

Moos, H. W., Cash, W. C., Cowie, L. L., et al. 2000, ApJL, 538, L1

Morris, S. L., Weymann, R. J., Dressler, A., et al. 1993, ApJ, 419, 524

Moster, B. P., Somerville, R. S., Maulbetsch, C., et al. 2010, ApJ, 710, 903

Mulchaey, J. S., & Chen, H.-W. 2009, ApJL, 698, L46

Mulchaey, J. S., Mushotzky, R. F., Burstein, D., & Davis, D. S. 1996, ApJL, 456, L5

Muller, C. A., Oort, J. H., & Raimond, E. 1963, Academie des Sciences Paris Comptes Rendus, 257, 1661

Murray, N., Ménard, B., & Thompson, T. A. 2011, ApJ, 735, 66

Myers, A. D., Brunner, R. J., Nichol, R. C., et al. 2007, ApJ, 658, 85

Narayanan, A., Savage, B. D., Wakker, B. P., et al. 2011, ApJ, 730, 15

Navarro, J. F., & White, S. D. M. 1994, MNRAS, 267, 401

Nestor, D. B., Johnson, B. D., Wild, V., et al. 2011, MNRAS, 412, 1559

Nesvadba, N. P. H., Lehnert, M. D., De Breuck, C., Gilbert, A. M., & van Breugel, W. 2008, AAP, 491, 407

Netzer, H. 2015, ArXiv e-prints

Oke, J. B., & Gunn, J. E. 1983, ApJ, 266, 713

Oosterloo, T. A., Morganti, R., Sadler, E. M., van der Hulst, T., & Serra, P. 2007, AAP, 465, 787

Oppenheimer, B. D., & Davé, R. 2006, MNRAS, 373, 1265

—. 2008, MNRAS, 387, 577

—. 2009, MNRAS, 395, 1875

Oppenheimer, B. D., Davé, R., Katz, N., Kollmeier, J. A., & Weinberg, D. H. 2012, MNRAS, 420, 829

Oppenheimer, B. D., Crain, R. A., Schaye, J., et al. 2016, MNRAS

Ostriker, J. P., Peebles, P. J. E., & Yahil, A. 1974, ApJL, 193, L1

Padmanabhan, N., White, M., Norberg, P., & Porciani, C. 2009, MNRAS, 397, 1862

Pascarelle, S. M., Lanzetta, K. M., Chen, H.-W., & Webb, J. K. 2001, ApJ, 560, 101

Penton, S. V., Shull, J. M., & Stocke, J. T. 2000, ApJ, 544, 150

Penton, S. V., Stocke, J. T., & Shull, J. M. 2004, ApJS, 152, 29

Penzias, A. A., & Wilson, R. W. 1965, ApJ, 142, 419

Pettini, M., & Pagel, B. E. J. 2004, MNRAS, 348, L59

Pisano, D. J., Barnes, D. G., Staveley-Smith, L., et al. 2011, ApJS, 197, 28

Planck Collaboration, Ade, P. A. R., Aghanim, N., et al. 2015, ArXiv e-prints

Poggianti, B. M., von der Linden, A., De Lucia, G., et al. 2006, ApJ, 642, 188

Prochaska, J. X., Chen, H.-W., Howk, J. C., Weiner, B. J., & Mulchaey, J. 2004, ApJ, 617, 718

Prochaska, J. X., & Hennawi, J. F. 2009, ApJ, 690, 1558

Prochaska, J. X., Hennawi, J. F., & Simcoe, R. A. 2013, ApJL, 762, L19

Prochaska, J. X., Lau, M. W., & Hennawi, J. F. 2014, Ap, 796, 140

Prochaska, J. X., Weiner, B., Chen, H.-W., Cooksey, K. L., & Mulchaey, J. S. 2011a, ApJS, 193, 28

Prochaska, J. X., Weiner, B., Chen, H.-W., Mulchaey, J., & Cooksey, K. 2011b, ApJ, 740, 91

Prochaska, J. X., Weiner, B. J., Chen, H.-W., & Mulchaey, J. S. 2006, ApJ, 643, 680

Rahmati, A., Schaye, J., Bower, R. G., et al. 2015, ArXiv e-prints

Rahmati, A., Schaye, J., Crain, R. A., et al. 2016, MNRAS, 459, 310

Rao, S. M., Turnshek, D. A., & Nestor, D. B. 2006, ApJ, 636, 610

Rauch, M., Miralda-Escudé, J., Sargent, W. L. W., et al. 1997, ApJ, 489, 7

Rees, M. J., & Ostriker, J. P. 1977, MNRAS, 179, 541

Reyes, R., Mandelbaum, R., Gunn, J. E., et al. 2012, MNRAS, 425, 2610

Richards, G. T., Vanden Berk, D. E., Reichard, T. A., et al. 2002, AJ, 124, 1

Richards, G. T., Lacy, M., Storrie-Lombardi, L. J., et al. 2006, ApJS, 166, 470

Richter, P., Savage, B. D., Tripp, T. M., & Sembach, K. R. 2004, ApJS, 153, 165

Rogerson, J. B., York, D. G., Drake, J. F., et al. 1973, ApJL, 181, L110

Rosenberg, J. L., & Schneider, S. E. 2003, ApJ, 585, 256

Rubin, V. C., & Ford, Jr., W. K. 1970, ApJ, 159, 379

Rubin, V. C., Thonnard, N., & Ford, Jr., W. K. 1978, ApJL, 225, L107

Rudie, G. C., Steidel, C. C., Shapley, A. E., & Pettini, M. 2013, ApJ, 769, 146

Rudie, G. C., Steidel, C. C., Trainor, R. F., et al. 2012, ApJ, 750, 67

Savage, B. D., Kim, T.-S., Wakker, B. P., et al. 2014, ApJS, 212, 8

Savage, B. D., Narayanan, A., Wakker, B. P., et al. 2010, ApJ, 719, 1526

Sawyer, D. G., Daly, P. N., Howell, S. B., Hunten, M. R., & Schweiker, H. 2010, in Proceedings of the SPIE, Vol. 7735, Ground-based and Airborne Instrumentation for Astronomy III, 77353A

Schaye, J., Dalla Vecchia, C., Booth, C. M., et al. 2010, MNRAS, 402, 1536

Schaye, J., Crain, R. A., Bower, R. G., et al. 2015, MNRAS, 446, 521

Schlafly, E. F., & Finkbeiner, D. P. 2011, ApJ, 737, 103

Schlegel, D. J., Finkbeiner, D. P., & Davis, M. 1998, ApJ, 500, 525

Schmidt, M. 1963, Nature, 197, 1040

Schmidt, M., & Green, R. F. 1983, ApJ, 269, 352

Schweizer, F., & Seitzer, P. 1992, AJ, 104, 1039

Scott, J. E., Rafiee, A., Bechtold, J., et al. 2015, ApJ, 800, 93

Serber, W., Bahcall, N., Ménard, B., & Richards, G. 2006, ApJ, 643, 68

Shapley, A. E., Steidel, C. C., Pettini, M., & Adelberger, K. L. 2003, ApJ, 588, 65

Shectman, S. A., & Johns, M. 2003, in The International Society for Optical Engineering Proceedings, ed. J. M. Oschmann & L. M. Stepp, Vol. 4837, 910–918

Shen, S., Madau, P., Guedes, J., et al. 2013a, ApJ, 765, 89

Shen, Y., & Ménard, B. 2012, ApJ, 748, 131

Shen, Y., Richards, G. T., Strauss, M. A., et al. 2011, ApJS, 194, 45

Shen, Y., McBride, C. K., White, M., et al. 2013b, ApJ, 778, 98

Sijacki, D., Springel, V., Di Matteo, T., & Hernquist, L. 2007, MNRAS, 380, 877

Silk, J. 1968, ApJ, 151, 459

Silk, J., & Rees, M. J. 1998, AAP, 331, L1

Simcoe, R. A., Sargent, W. L. W., Rauch, M., & Becker, G. 2006, ApJ, 637, 648

Smith, B. D., Hallman, E. J., Shull, J. M., & O'Shea, B. W. 2011, ApJ, 731, 6

Smoot, G. F., Bennett, C. L., Kogut, A., et al. 1992, ApJL, 396, L1

Soderblom, D. R., Hulbert, S. J., Leitherer, C., & Sherbert, L. 1995, Goddard High Resolution Spectrograph Instrument Handbook v. 6.0

Spergel, D. N., Verde, L., Peiris, H. V., et al. 2003, ApJS, 148, 175

Spinrad, H., Filippenko, A. V., Yee, H. K., et al. 1993, AJ, 106, 1

Spitzer, Jr., L. 1956, ApJ, 124, 20

—. 1968, Science, 161, 225

Spitzer, Jr., L., & Baade, W. 1951, ApJ, 113, 413

Springel, V., Di Matteo, T., & Hernquist, L. 2005, MNRAS, 361, 776

Steidel, C. C., Dickinson, M., Meyer, D. M., Adelberger, K. L., & Sembach, K. R. 1997, ApJ, 480, 568

Steidel, C. C., Erb, D. K., Shapley, A. E., et al. 2010, ApJ, 717, 289

Stinson, G. S., Brook, C., Prochaska, J. X., et al. 2012, MNRAS, 425, 1270

Stocke, J. T., Keeney, B. A., Danforth, C. W., et al. 2013, ApJ, 763, 148

Stocke, J. T., Penton, S. V., Danforth, C. W., et al. 2006, ApJ, 641, 217

Stocke, J. T., Shull, J. M., Penton, S., Donahue, M., & Carilli, C. 1995, ApJ, 451, 24

Stocke, J. T., Keeney, B. A., Danforth, C. W., et al. 2014, ApJ, 791, 128

Strateva, I., Ivezić, Ž., Knapp, G. R., & et al.. 2001, AJ, 122, 1861

Suresh, J., Bird, S., Vogelsberger, M., et al. 2015, MNRAS, 448, 895

Tejos, N., Morris, S. L., Finn, C. W., et al. 2014, MNRAS, 437, 2017

Tepper-García, T., Richter, P., Schaye, J., et al. 2011, MNRAS, 413, 190

Thom, C., & Chen, H.-W. 2008a, ApJS, 179, 37

—. 2008b, ApJ, 683, 22

Thom, C., Tumlinson, J., Werk, J. K., et al. 2012, ApJL, 758, L41

Tilton, E. M., Danforth, C. W., Shull, J. M., Ross, T. L., & Ross, T. L. 2012, ApJ, 759, 112

Tinker, J., Kravtsov, A. V., Klypin, A., et al. 2008, ApJ, 688, 709

Tonnesen, S., & Bryan, G. L. 2009, ApJ, 694, 789

Toomre, A., & Toomre, J. 1972, ApJ, 178, 623

Tripp, T. M., Aracil, B., Bowen, D. V., & Jenkins, E. B. 2006, ApJL, 643, L77

Tripp, T. M., Lu, L., & Savage, B. D. 1998, ApJ, 508, 200

Tripp, T. M., & Savage, B. D. 2000, ApJ, 542, 42

Tripp, T. M., Savage, B. D., & Jenkins, E. B. 2000, ApJL, 534, L1

Tripp, T. M., Sembach, K. R., Bowen, D. V., et al. 2008, ApJS, 177, 39

Tumlinson, J., Thom, C., Werk, J. K., et al. 2013, ApJ, 777, 59

—. 2011, Science, 334, 948

Turner, M. L., Schaye, J., Steidel, C. C., Rudie, G. C., & Strom, A. L. 2014, MNRAS, 445, 794

Tytler, D., & Fan, X.-M. 1992, ApJS, 79, 1

Urry, C. M., & Padovani, P. 1995, PASP, 107, 803

Vanden Berk, D., Khare, P., York, D. G., et al. 2008, ApJ, 679, 239

Veilleux, S., Meléndez, M., Sturm, E., et al. 2013, ApJ, 776, 27

Verdes-Montenegro, L., Yun, M. S., Williams, B. A., et al. 2001, AAP, 377, 812

Vestergaard, M., & Wilkes, B. J. 2001, ApJS, 134, 1

Vogelsberger, M., Genel, S., Sijacki, D., et al. 2013, MNRAS, 436, 3031

Vogelsberger, M., Genel, S., Springel, V., et al. 2014, Nature, 509, 177

Vogt, S. S., Allen, S. L., Bigelow, B. C., et al. 1994, in Proceedings of the SPIE, Vol. 2198, Instrumentation in Astronomy VIII, ed. D. L. Crawford & E. R. Craine, 362

Wakker, B. P., & Savage, B. D. 2009, ApJS, 182, 378

Wang, B. 1993, ApJ, 415, 174

Werk, J. K., Prochaska, J. X., Thom, C., et al. 2012, ApJS, 198, 3

—. 2013, ApJS, 204, 17

Weymann, R. J., Williams, R. E., Peterson, B. M., & Turnshek, D. A. 1979, ApJ, 234, 33

White, M., Myers, A. D., Ross, N. P., & et al. 2012, MNRAS, 424, 933

White, S. D. M., & Rees, M. J. 1978, MNRAS, 183, 341

Whiting, M. T., Webster, R. L., & Francis, P. J. 2006, MNRAS, 368, 341

Wild, V., Kauffmann, G., White, S., et al. 2008, MNRAS, 388, 227

Williger, G. M., Heap, S. R., Weymann, R. J., et al. 2006, ApJ, 636, 631

Woodgate, B. E., Kimble, R. A., Bowers, C. W., et al. 1998, PASP, 110, 1183

Yip, C. W., Connolly, A. J., Szalay, A. S., et al. 2004, AJ, 128, 585

Yoon, J. H., Putman, M. E., Thom, C., Chen, H.-W., & Bryan, G. L. 2012, ApJ, 754, 84

York, D. G. 1974, ApJL, 193, L127

York, D. G., Adelman, J., Anderson, Jr., J. E., & et al.. 2000, AJ, 120, 1579

Zakamska, N. L., & Greene, J. E. 2014, MNRAS, 442, 784

Zhang, S., Wang, T., Wang, H., & Zhou, H. 2013, ApJ, 773, 175

Zhu, G., & Ménard, B. 2013, ApJ, 770, 130